One-Dimensional Physics of Interacting Electrons and Phonons in Carbon Nanotubes

Thesis by
Vikram Vijay Deshpande

In Partial Fulfillment of the Requirements
for the Degree of
Doctor of Philosophy

California Institute of Technology
Pasadena, California

2009

(Defended September 15, 2008)

To

my mother

and

my late father

Acknowledgements

It is hard to compress six years of a journey into a couple of pages, but let me give it a shot anyway. I should begin by thanking the person who influenced this thesis the most, my advisor Prof. Marc Bockrath—for taking me on as a curious-but-mostly-clueless engineer, showing faith in my ability to learn on the job, introducing me to the joys of exploratory research, giving me the freedom to follow my interests—Marc, I cannot thank you enough. Everything about you, from your insight into physics and your scientific integrity to your sense of humor, has left an impression on me. Gestures like letting me participate in your theorist discussions and giving me the opportunity to talk at important conferences—indeed, I have been told by senior faculty that I am lucky to have received such mentorship. You have shown me how to be a good scientist.

I'd like to thank Professors Harry Atwater, Jim Eisenstein and Gil Refael for serving on my committee and for their input at various stages of my Ph.D.; Adam Bushmaker and Prof. Steve Cronin for our very fruitful collaboration; Scott Hsieh for your enthusiasm and diligence. Other collaborators I have worked with during the course of this thesis: Dmitry Novikov, Greg Fiete, Gil, Ryan Barnett—the theorist-experimentalist meetings were very useful; Hsin-Ying Chiu, Henk Postma for your efforts during the MWNT work; Csilla Miko and Laszlo Forro for providing excellent MWNT material; more recently, Prof. Jim Hone, Bhupesh Chandra and Rob Caldwell—I guess I'll be seeing you soon. I'd like to thank all my lab members: Hsin-Ying for being the senior and responsible member, Hareem Maune, Jinseong Heo, Brian Standley, Isabella Kierk, Henk, Bertrand Bourlon, Joyce Wong, Anthony Mendez, Peter Hung, Emma Schmidgall, Kai Zhu for the nice company. I must thank Eleonora Vorobieff, Rosalie Rowe, Irene Loera and Connie Rodriguez for taking care of administrative matters and Ali Ghaffari for cleanroom maintenance. Other people who influenced this thesis include Teresa Emery who evaporated my first platinum samples; Jien Cao and Dunwei Wang for assuring me, after multiple unsuccessful attempts, that the fabrication technique actually worked; and Brian Thibeault and Ning Cao for all the help at Santa Barbara. I'd like to also acknowledge Professors Kaushik Bhattacharya, Rob Phillips, G. Ravichandran and Sandra Troian for valuable guidance; and helpful scientific interactions with members of the condensed matter community—Professors David Cobden, Hongjie Dai, Mandar Deshmukh, Arindam Ghosh, Leonid Glazman, Ronald Hanson, Tony

Heinz, Shahal Ilani, Atac Imamoglu, Pablo Jarillo-Herrero, Jeannie Lau, Konrad Lehnert, Karyn LeHur, Leonid Levitov, Philip Kim, Marcus Kindermann, Leo Kouwenhoven, Charlie Marcus, Ethan Minot, Jesper Nygard, Hongkun Park, Jason Petta, Daniel Prober, Leo Radzhihovsky, Rob Schoelkopf, Mansour Shayegan, Lieven Vandersypen, Amir Yacoby, Val Zwiller and many others.

Away from your family, your friends are your best support group; indeed, these years would have been unimaginable without my friends—Jen Dionne, for entertaining stories, company during the weird schedules we were the only ones who seemed to keep, for your enthusiasm for science (which is infectious), but most of all for letting me count on your friendship through good times and bad; Waheb Bishara, Deepak Kumar, Raviv Perahia, Jenn Stockdill, Tristan Ursell, Nhat Vu—we had a great time through the all-nighters at Watson, random discussions, horrific hiking experiences (poison oak, anyone?). Of course I have to mention the nicest roommates I've had—Vijay Natraj, Tejaswi Navilarekallu, and Chaitanya Rao, for taking me under their wing my first year, and the chaos that ensued—movie making, festival organizing, cricket playing/screening... that night of the World Cup of 2003 when we hosted possibly the entire Indian community of Pasadena in our apartment, with multiple screenings in every room, shall remain engrained in my memory—no wonder I got nothing done that year! My subsequent roommates—Carey Hsu, Francisco Ortega, Meher Ayalasomayajula and David Yeaton-Massey for being good sports. Naresh Satyan and Phanish Suryanarayana for being good friends and neighbors these last couple of years (and letting me subject you to my primitive culinary skills). Shwetank Kumar, Abhishek Tiwari, Krish Subramaniam, Sowmya Chandrasekhar, Shankar Kalyanaraman, Arun Natarajan, Karen Remedios, Meher—those were good times. Shaunak Sen, Uday Khankhoje, Mayank Bakshi, Prabha Mandayam, Pinkesh Patel, Sujit Nair, Zeeshan Ahmed, Vikram Gavini, Nachiket Kapre, Sukhada Phadnavis, Radhika Marathe, Iram Bilal and many others—it was nice to spend time with you all; and all the people I have known in Watson or otherwise: Brendan Kayes, Robb Walters, Mike Filler, Mike Kelzenberg, April Neidholdt, Matt Eichenfield, Tom Johnson, Andrea Armani, Deniz Armani, Tobias Kippenberg, John Choi, Will Green, Eve Stenson, Saurabh Vyawahare, Jeff Fingler, Sotiris Masmanidis, Akshay Naik, Matt LaHaye, Tomo Honda, Aditya Khair, Rizal Hariadi, Orion Crisafulli, Tristan Smith, Jenny Roizen, Erin Koos, Anna Folinsky and many others. My buddies at UCLA—Vishal Shrotriya (and later Shweta Sharma), Ram Rengaswamy, Saurabh Ganeriwal, Amit

Jain, Aman Kansal—the assorted spontaneous road trips were fun. All the old-timers who stuck through grad school—Vijay Desai, Anurag Ganguli, Rohit Karnik, Bhaskaran Muralidharan, Ankur Pareek, Sameera Poduri, Shodhan Rao, Pramod Reddy—thanks for all the discussions on academia, science and life in general.

An event which changed my life (and also coincided with the time things turned around for this thesis) was the death of my father mid-way through my PhD. I am extremely grateful to my extended family for helping me cope with his loss and for their support of all my endeavors. My father did not live to see any of this work, but I am sure he would have been proud of me. To my mother, who is the bravest woman I know, surely you know that none of this would have been possible without your continued support and love—I dedicate this thesis to you and to the memory of my father.

Vikram Deshpande

September 2008

Pasadena, CA

Abstract

The one-dimensional (1D) world is quite different from its higher dimensional counterparts. For example, the electronic ground state in 1D is not a Fermi liquid as in most solids, due to the role of electron-electron interactions. Most commonly, electrons in 1D are described as a *Luttinger liquid*, where the low-energy excitations are decoupled bosonic charge and spin waves. Carbon nanotubes are clean 1D systems which have been shown to behave like a Luttinger liquid at high electron density. However, at low electron density and in the absence of disorder, the ground state is predicted to be a *1D Wigner crystal*—an electron solid dominated by long-range Coulomb interaction. Moreover, short-range interaction mediated by the atomic lattice (umklapp scattering) is predicted to transform a nominal 1D metal into a *Mott insulator*.

In this thesis, we develop techniques to make extremely clean nanotube single-electron transistors. We study them in the few-electron/hole regime using Coulomb blockade spectroscopy in a magnetic field. In semiconducting nanotubes, we map out the antiferromagnetic exchange coupling as a function of carrier number and find excellent agreement to a Wigner crystal model. In nominally metallic nanotubes, we observe a universal energy gap in addition to the single-particle bandgap, implying that nanotubes are never metallic. The magnitude, radius dependence and low-energy neutral excitations of this additional gap indicate a Mott insulating origin.

Further, we use simultaneous electrical and Raman spectroscopy measurements to study the phonons scattered by an electric current. At high bias, suspended nanotubes show striking negative differential conductance, attributed to non-equilibrium phonons. We directly observe such "hot" phonon populations in the Raman response and also report preferential electron coupling to one of two optical phonon modes. In addition, using spatially-resolved Raman spectroscopy, we obtain a wealth of local information including the 1D temperature profile, a spatial map of the thermal conductivity and thermal contact resistances, which reveal the mechanism of thermal transport in nanotubes.

Finally, with multi-wall nanotubes (MWNTs), we use electrical breakdown as thermometry to provide evidence for ballistic phonon propagation and obtain an estimate for the quantum of thermal conductance. We also develop linear-bearing nanoswitches using the low-friction properties of MWNTs.

Contents

List of Figures

List of Publications

Portions of this thesis have been drawn from the following publications:

Chapter 4 appears as:
"The One-Dimensional Wigner Crystal in Carbon Nanotubes", V. V. Deshpande and M. Bockrath, *Nature Physics*, **4**, 314, 2008

Chapter 5 is similar to:
"Observation of a Mott Insulating State in Ultra-Clean Carbon Nanotubes", V. V. Deshpande, B. Chandra, R. Caldwell, D. Novikov, J. Hone and M. Bockrath, submitted to *Science*

Chapter 6 consists of:
"Direct Observation of Mode Selective Electron-Phonon Coupling in Suspended Carbon Nanotubes", A. W. Bushmaker, V. V. Deshpande, M. Bockrath, S. B. Cronin, *Nano Letters*, **7**, 3618, 2007
"Spatially-Resolved Temperature Measurements of Electrically-Heated Carbon Nanotubes", V. V. Deshpande, S. Hsieh, A. W. Bushmaker, M. Bockrath, S. B. Cronin, submitted to *Physical Review Letters*

Chapter 7 appears as:
"Ballistic Phonon Thermal Transport in Multi-Walled Carbon Nanotubes", H.-Y. Chiu*, V. V. Deshpande*, H. W. Ch. Postma, C. N. Lau, C. Miko, L. Forro, M. Bockrath, *Physical Review Letters*, **95**, 226101, 2005

Chapter 8 appears as:

"Carbon Nanotube Linear Bearing Nanoswitches", V. V. Deshpande*, H.-Y. Chiu*, H. W. Ch. Postma, C. Miko, L. Forro, M. Bockrath, *Nano Letters*, **6**, 1092, 2006

The following work has not been included in this thesis:

"Direct Observation of Born-Oppenheimer Approximation Breakdown in Carbon Nanotubes", A. W. Bushmaker, V. V. Deshpande, S. Hsieh, M. Bockrath, S. B. Cronin, submitted to *Nano Letters*

"Giant Raman Intensity Modulation in Suspended Carbon Nanotubes", A. W. Bushmaker, V. V. Deshpande, S. Hsieh, M. Bockrath, S. B. Cronin, to be submitted

(* indicates equal contribution)

Chapter 1

Introduction

It is only appropriate to begin a thesis on electrons and phonons with a reference to John Ziman who wrote the most exhaustive treatise to date on electrons and phonons titled, well, *Electrons and Phonons* [1]. Ziman likes to quote Lewis Carroll; there was one very imaginative quote in particular, which I'd like to borrow:

> ... they began running when they liked and stopped when they liked, so it was not easy to know when the race was over.

Ziman makes a striking analogy between the chaotic nature of the caucus race and the random behavior of electrons and phonons in solids. However, this analogy can also be used to highlight the progress made in the ensuing decades towards understanding and controlling their behavior. Several groups around the world have now isolated a single electron and have used its spin as a quantum bit towards the holy grail of building a quantum computer. Efforts are on at engineering phonons, which are often responsible for relaxing the quantum bits, so as to obtain longer electron lifetimes. This progress has been due to the availability of clean materials (two-dimensional electron gases (2DEGs), in the above case) and constantly improving lithographic techniques. This thesis shall focus on the behavior of electrons and phonons in clean carbon nanotube devices, made using special lithographic techniques. In particular, the one-dimensional (1D) nature of carbon nanotubes gives rise to rich physics, some of which has no counterpart in higher dimensions.

Electronic properties of most materials are understood from the most successful theory in solid state physics, Landau's Fermi liquid theory. However, it has been known that this theory breaks down in 1D due to electron-electron interactions, and an alternative paradigm, most commonly *Luttinger liquid theory* has been used to describe 1D systems [2]. Until recently however, the absence of 1D systems in experiment had prevented one from expressing much confidence in this theory. In the last decade, the availability of clean

1D systems such as carbon nanotubes [3], molecular beam epitaxy (MBE)-grown cleaved-edge quantum wires [4] and edge states of the fractional quantum Hall effect (FQHE) in 2DEGs [5] have been used to verify that the 1D electron gas is indeed a Luttinger liquid.

Things can only become more interesting with the advent of cleaner materials and use of alternative measurement techniques. In particular, the group of Hongjie Dai at Stanford has recently pioneered a technique for growing nanotubes on metal electrodes and in a suspended geometry [6]. These as-grown, suspended single-wall nanotubes avoid disorder from the substrate or chemical processing and show unprecedented cleanness in transport measurements [7]. In my graduate work, I developed this technique further and investigated the behavior of interacting electrons in carbon nanotubes, in the process finding evidence for two more electronic states in 1D: the Wigner crystal and the Mott insulator.

Nanotubes have a quantized 1D phonon spectrum. The interaction of phonons with electrons and their propagation along the nanotube has important implications towards use of nanotubes in miniaturizing electronic circuits. Nanotubes have been touted as the replacement of CMOS transistors and copper interconnects. An understanding of electron-phonon interactions and phonon transport in nanotubes can provide the necessary knowledge towards effective thermal management in these high-heating applications. Our tool in studying phonons in electrically-heated nanotubes is Raman spectroscopy. It turns out, this study also yields some surprises, again in part due to the 1D nature of nanotubes.

Another material, a sibling of the single-wall nanotube (SWNT), is the multi-wall nanotube (MWNT). Its complex structure of nestled walls (or shells), much like a Russian doll, provides a system with moving parts, moving with almost zero friction! I investigated mechanical motion and thermal transport in this system in the early part of my Ph.D., and it still remains a rich system for study.

Organization of this thesis

The rest of this chapter discusses the electronic and phonon dispersion of nanotubes, describes important concepts used in this work and reviews the relevant previous work. Chapter 2 details the fabrication procedure used to obtain extremely clean nanotube data. Chapter 3 treats theoretically the subject of electron-electron interactions in carbon nanotubes. Chapter 4 shows evidence for a 1D Wigner crystal in semiconducting nanotubes. Chap-

ter 5 deals with experiments in "metallic" nanotubes showing a Mott insulating state at half-filling of energy bands. Chapter 6 shows the use of simultaneous electrical and Raman spectroscopy towards understanding electron-phonon interactions and phonon transport in nanotubes. Chapter 7 shows evidence for ballistic phonon propagation in MWNTs. Chapter 8 uses MWNTs to realize low-friction bearing devices. Chapter 9 concludes with a section on possible future directions.

1.1 Carbon nanotubes; electronic and thermal properties

Carbon nanotubes, the thinnest and cleanest of all 1D systems, were first made by Ijima in 1991 [8]. The first nanotubes were multi-walled, made from a carbon-arc soot. In 1996, single-wall nanotubes were produced in bulk for the first time using a laser ablation technique by Smalley and co-workers [9]. Nanotubes were grown on chip for the first time by the Dai group in 1998 [10], using a technique called chemical vapor deposition (CVD). All single-wall tubes used in this study were CVD-grown, and this technique will be discussed in more detail in Chapter 2. The multi-wall tubes in this study were produced by the arc-discharge technique [8] in the group of Laszlo Forro at EPFL.

A single-wall nanotube is essentially a single sheet of graphite (called graphene) rolled up into a cylinder (Fig. 1.1(a)). Graphene is an sp^2 bonded network of carbon atoms arranged in a hexagonal lattice with two atoms per unit cell. Figure 1.1(c) shows the low-energy band structure of graphene in the first Brillouin zone (Fig. 1.1(b)). The Fermi surface of graphene consists of six (Dirac) points at the corners of the hexagonal Brillouin zone where the conduction and valence bands touch, obtained by translating the two inequivalent points (corresponding to the two atoms in the unit cell) by reciprocal lattice vectors.

The band structure of nanotubes can be derived directly from that of graphene [12]. By imposing periodic boundary conditions for translations by the roll-up vector that defines the nanotube, the wave-vector $k_\perp$ along the circumference πD is quantized as $\pi D k_\perp = 2\pi j$, where j is an integer. An example of this is shown in Figure 1.1(b) with horizontal lines corresponding to the quantized $k_\perp$. The resulting intersection of $k_\perp$ with graphene's bandstructure is shown in Figure 1.1(c) in red lines. Thus, the band structure of a nanotube consists of 1D subbands. For a 1 nm diameter tube the subband splitting is on the order of one eV, and therefore nanotubes are truly 1D materials. The nanotube will have a band

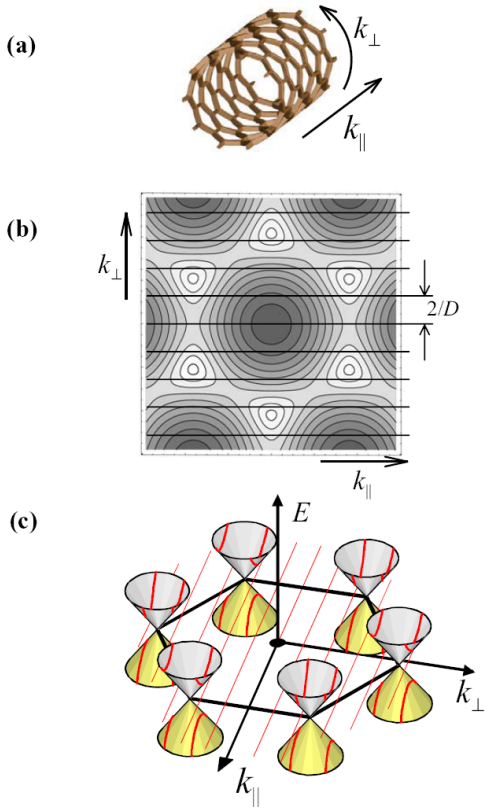

Figure 1.1. **(a)** Axes of a nanotube. **(b)** Quantized Brillouin zone of graphene. **(c)** Quantization of graphene's bandstructure to yield 1D sub-bands. [11]

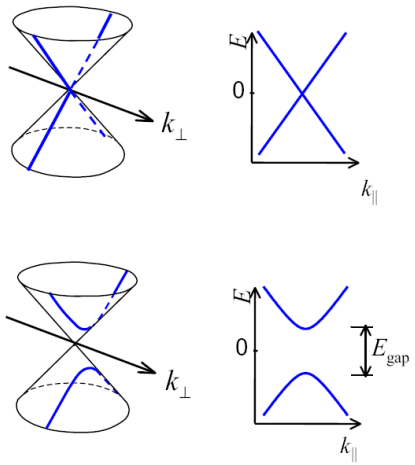

Figure 1.2. Bandstructure of metallic (top) and semiconducting (bottom) nanotubes depending on whether $k_\perp$ passes through a Dirac point or not. [11]

gap unless the red lines in Fig. 1.1(c) pass though the two gapless points. Figure 1.2 shows the band-structure of the resulting metallic and semi-conducting nanotubes. Effects due to curvature or in-built strain or twist (during device fabrication) result in corrections to this picture [13]. For example, this results in translation of the Dirac points of graphene and opens a small band-gap for most metallic nanotubes. However, the class of nanotubes with highest symmetry, called armchair nanotubes, are insensitive to most perturbations in a single-particle picture. For the purposes of this thesis, nanotubes with energy gaps $\lesssim k_B T$ at room temperature will be referred to as "metallic", "quasi-metallic" or "small-band-gap" while those with larger gaps will be called "semiconducting" (since the distinction, as per zone folding theory, cannot be made in a transport experiment).

Similar to the band-structure, the quantized phonon dispersion of nanotubes can be obtained by zone-folding the phonon dispersion of graphite [14]. The dispersion for graphite and that for a representative armchair nanotube are shown in Figure 1.3. The sub-band spacing for phonon modes is much smaller than the electrons, and many modes may be occupied at room temperature. Among them the following optical phonon modes will be studied in more detail in Chapter 6 using Raman spectroscopy:

- A longitudinal optical (LO) mode with atomic motion along the nanotube,
- A transverse optical (TO) mode with atoms vibrating perpendicular to the nanotube axis.

Figure 1.4 shows the atomic motion for these modes.

1.2 Overview of concepts and techniques

The following techniques have been used in the course of this work:

Coulomb blockade spectroscopy

Coulomb blockade is a phenomenon that arises in small metallic islands connected to large metal contacts through tunnel barriers (see Figure 1.5). If the size of the island is small enough that the energy required to add a single electron (charging energy $E_c = e^2/C$ where C is the capacitance of the island to the external world) is larger than the thermal energy $k_B T$ and the barriers are sufficiently opaque so as to confine electrons on the island

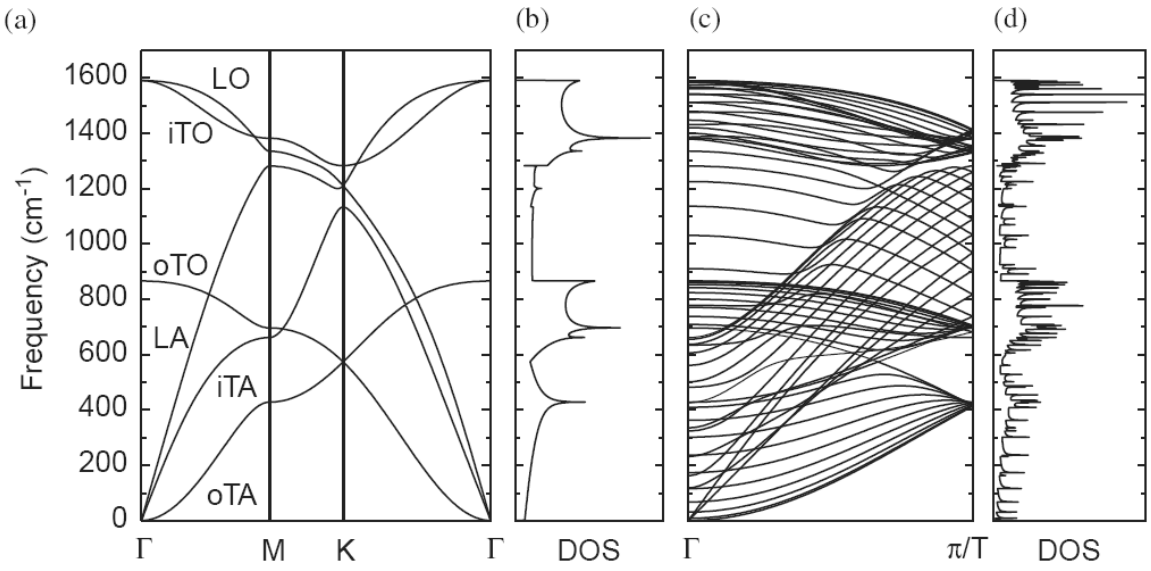

Figure 1.3. Phonon dispersions and density of states for graphite (**(a)** and **(b)**) and a representative nanotube (**(c)** and **(d)**). [15]

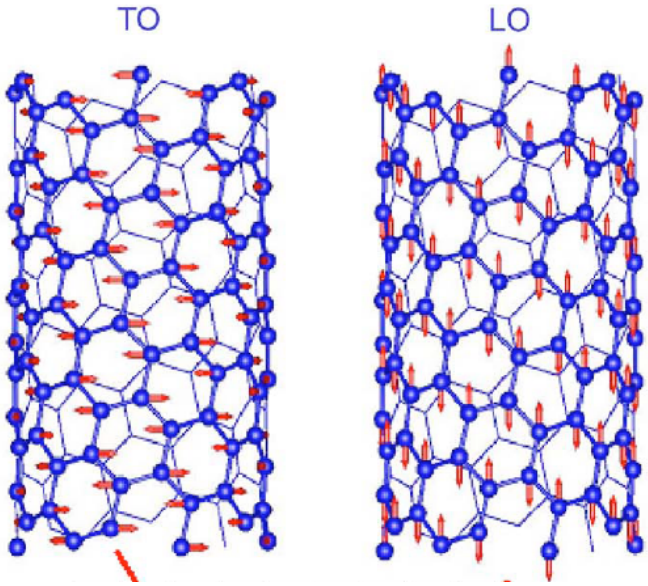

Figure 1.4. Atomic motion for TO and LO phonon modes. [16]

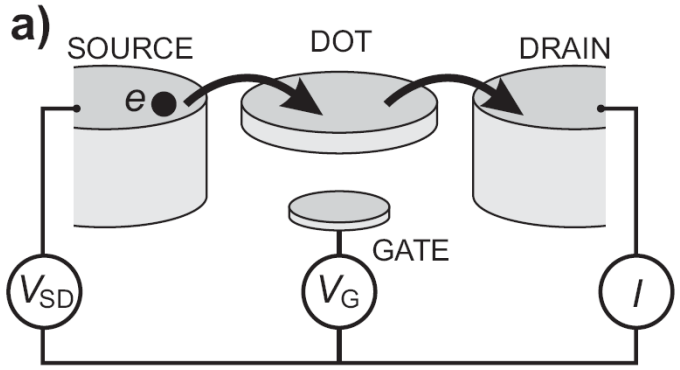

Figure 1.5. An island (or dot) connected to metallic leads. [17]

(in general, the contact resistance R_c should be much larger than the quantum resistance $h/e^2 \simeq 25k\Omega$), no current can flow through the island. This blockade can be removed by either changing the chemical potential of the island by varying an external gate voltage or injecting electrons with high enough energy by applying a bias voltage, leading to flow of current. This device is called a single-electron transistor (SET).

Another effect that is important in small systems is discretization of the energy spectrum due to the formation of zero-dimensional (0D) electron states. Such a "quantum dot" or "artificial atom" also shows similar behavior as above, with an additional energy scale (level spacing ΔE between successive quantum dot energy levels). The energy required to add an electron is now $E = E_c + \Delta E$. Figure 1.6 shows this behavior schematically. See [18] for a detailed treatment of Coulomb blockade in SETs and quantum dots. Coulomb blockade has been extensively studied in metallic grains, nano-crystals, single molecules, vertical and lateral quantum dots in semi-conductor heterostructures and finite-size segments of nanotubes and nanowires. In this thesis, I show the use of this technique to study the energy spectrum of clean small-bandgap nanotubes near the band-edge (see Chapter 5 for more details).

A simple model used to understand Coulomb blockade is the Constant Interaction (CI) model [18]. This model treats the interactions between electrons on the island as a constant, irrespective of their number and captures this physics in the capacitance C. The CI model has been remarkably successful in explaining experiments, however it has been found wanting in explaining the behavior over a large change in carrier density [19]. In particular, it is known that at extremely low carrier density, interactions dominate over

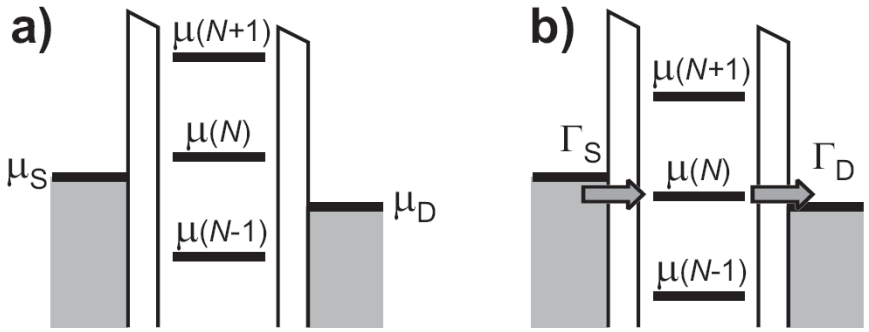

Figure 1.6. **(a)** Current is blockaded and **(b)** the blockade is removed, in this case, by changing the chemical potential via the gate voltage. [17]

kinetic energy [20]. This regime cannot be explained with a single constant independent of density. We have explored this regime in detail for the first time in nanotubes, studying semiconducting nanotubes at low carrier density (see chapter 4 for more details).

Raman spectroscopy

Raman spectroscopy involves the inelastic scattering of monochromatic light, usually from a laser in the visible, near-infrared, or near-ultraviolet range, by phonons and other low-frequency excitations of the system. The elastically scattered light is filtered out, and the rest of the light is collected on a detector. By measuring the intensity of the scattered light as a function of frequency (which is called the Raman spectrum), one can obtain an accurate measure of the phonon frequencies of the material. Raman scattering of light can occur by emitting phonons (Stokes process) or absorbing phonons (anti-Stokes process).

Raman spectroscopy has been studied in carbon nanotubes since the late 90s (see [15] for a review) and has been used to correlate optical spectra to atomic structure. In spite of the extremely small diameter of nanotubes ($\sim$ 1 nm) compared to the wavelength of light, nanotubes can have a large scattering cross-section if the energy of the incident or scattered light corresponds to a van-Hove singularity in the electronic density of states of the carbon nanotube. Such a process is called resonant Raman scattering. Previously, Raman spectroscopy measurements have been performed by shining a laser on a large number of nanotubes dispersed on a Si substrate, and gathering information on the tubes resonant with the laser.

In studying electrically contacted individual nanotubes with Raman spectroscopy, one

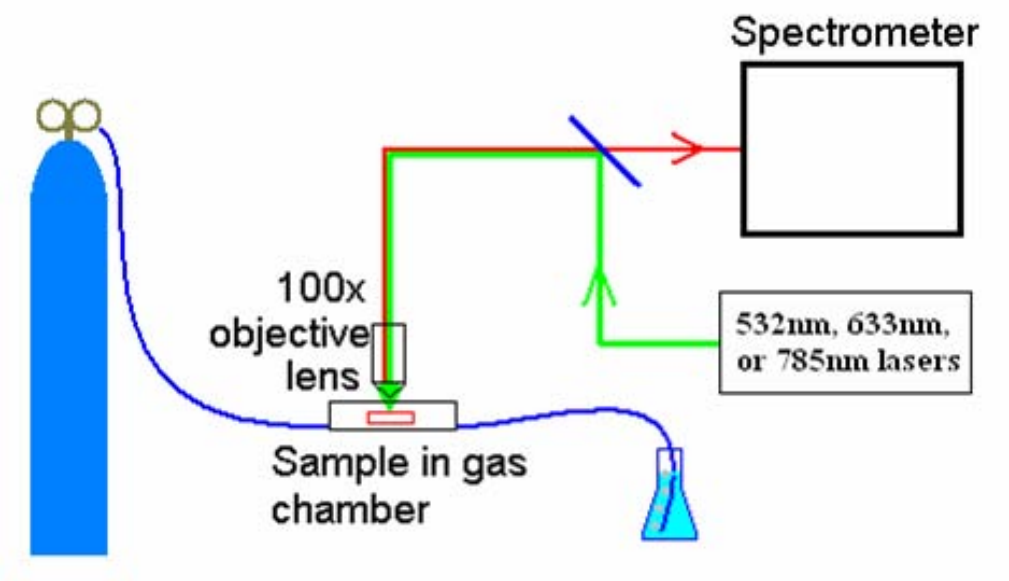

Figure 1.7. Schematic diagram of experimental setup for simultaneous transport and Raman measurements

will almost surely *not* find it resonant with the laser. Nevertheless, we have studied over a hundred nanotube devices using Raman spectroscopy and report on the resonant devices or those with a measurably large Raman signal. Figure 1.7 shows a schematic diagram of our experimental setup (the optical measurements were carried out in the lab of our collaborator, Steve Cronin, at the University of Southern California). The nanotube device was housed in a home-made chamber flushed with argon gas to prevent burn-out from the high bias voltages involved in the experiment. In particular, we were interested in observing the LO and TO phonon modes that have been proposed to be responsible for the current saturation and negative differential conductance in nanotubes at high bias voltages (see next section).

1.3 Previous work

Low-temperature electron transport

In this section, I shall review previous work in clean (i.e., ballistic) SWNTs with normal metal contacts. A lot of low-temperature work has also been done with superconducting and magnetic contacts, local gates and diffusive/disordered systems, which are beyond the scope of this thesis. Single-electron transport in nanotubes was first observed by Bockrath

et al. [21] and Tans et al. [22] in 1997 using resistive (weakly coupled) contacts. McEuen et al. [23] showed that while metallic SWNTs form clean single quantum dots, similarly long segments of semiconducting nanotubes break up into multiple quantum dots, due to disorder. Four-fold filling of 0D electron states was observed [24, 25] and the relevant energy scales (level spacing, sub-band splitting, ferromagnetic exchange, etc.) were determined. Slightly better contacts led to the observation of the Kondo effect in nanotubes [26], where electron wave-functions leak into the leads and interaction with spins in the leads becomes possible. For almost transparent contacts, multiply-reflected electron waves formed an interference pattern [27] analogous to Fabry-Perot interference in optical cavities. In 2004, Jarillo-Herrero et al. [28] observed the few-electron-hole regime for the first time using a suspended nanotube. Minot et al. [29] found that electron states near the band-edge had a magnetic moment much larger than the Bohr magneton. This was understood semi-classically as electrons orbiting around the circumference of the nanotube, the direction of orbiting corresponding to the k-point degeneracy. The Kondo effect was also observed for this orbital degree of freedom [30].

The observations above could be explained with a single-particle picture, as is expected in quantum dots with energy scales dominated by charging energy and level spacing. The role of interactions was observed when these energy scales were lowered by studying extremely long metallic nanotubes, ~ 2 μm, with tunnel contacts. Bockrath et al. [3] found power laws in non-linear transport and temperature dependence of conductance, in agreement with Luttinger liquid theory, applicable for a 1D metallic system. Note that power laws in clean systems are not to be confused with power laws in diffusive conductors, attributed to disorder (see, *e.g.* [31]) and understood from the Coulomb blockade in a resistive LC transmission line environment [32].

Room temperature high-bias transport

Relatively less work has been done on carbon nanotubes at high bias, in part because one runs the risk of destroying the sample. (It will blow up anyway, if you live in a place as dry as here. In our lab, we run humidifiers constantly, sprinkle water on the floor every few hours, work bare-foot *and* ground ourselves before we touch anything, to keep our samples alive.) Yao et al. [33] first studied high-bias transport in nanotubes and found that the current in SWNTs saturated at ~ 25 μA beyond a couple of volts of applied

bias. They proposed that this saturation was related to electron scattering off LO and TO phonons. Further work by Park et al. [34] and Javey et al. [35] estimated the mean-free path of electron-phonon scattering at high bias to be $\sim$ 100 nm. Pop et al. [36] discovered that *suspended* nanotubes showed negative differential conductance (NDC) in their *I-V* characteristics instead of saturation (shown in Fig. 1.8). They attributed it to a bottleneck of phonons, with a population higher than that arising from the equilibrium lattice temperature (non-equilibrium or "hot" phonons). We have found direct evidence of such hot phonons using simultaneous electrical and Raman measurements on nanotubes (see Section 6.1 for more details).

Collins and co-workers [37] found that applying a high enough bias to MWNTs led to burning of shells and demonstrated controllable shell burning one-by-one to engineer nanotubes of various thicknesses. The current drop on burning each each shell was found to be constant, $\sim$ 20 μA. We have used these observations to separate out MWNTs and ropes of nanotubes from the SWNTs. Moreover, our experiments on breakdown in MWNTs have led to the development of non-volatile switches based on telescoping motion of the concentric shells (see Chapter 8 for more details).

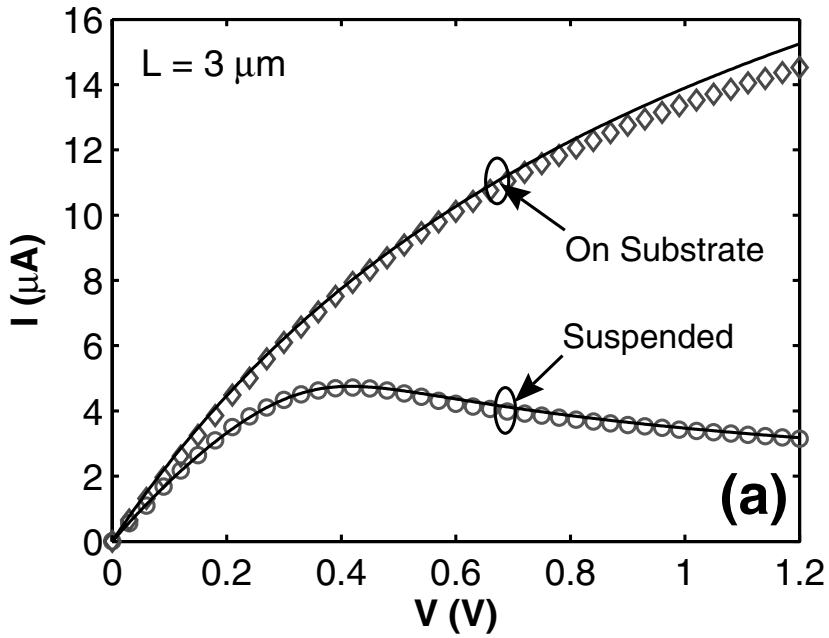

Figure 1.8. Negative differential conductance in suspended nanotubes, as observed by [36]

Thermal transport

Nanotubes have been predicted and reported to have a thermal conductivity ten times that of copper [38]. This raises hopes that phonon-phonon scattering mean-free-paths are large and that quantum thermal phenomena can be observed. Additionally, phonon transport influences the electrical characteristics, as mentioned in the previous section, and a systematic study of electrically-driven thermal transport can reveal information about the underlying electron-phonon coupling.

Previously, Philip Kim and co-workers heated MWNTs using micro-fabricated heaters and reported a temperature dependence of the thermal conductivity [38]. They also used a scanning probe technique to report the spatial variation of temperature in an electrically-heated MWNT [39]. Similar information has also been obtained, somewhat indirectly, by studying the melting of nano-particles placed around MWNTs [40]. These spatially-resolved temperature measurements involve temperature drops at the measurement contact interface. A *non-contact* measurement in electrically-heated *single-wall* nanotubes is desirable to understand thermal transport better. In Section 6.2, we report such a measurement using spatially-resolved Raman spectroscopy.

Chapter 2

Fabrication of Ultra-Clean Nanotube Devices

There exist a number of procedures for making electrical contact to carbon nanotubes. The most popular procedure is the one developed by my advisor during his graduate work [41] with variations over the years:

- Disperse bulk-grown nanotubes into solution; deposit solution on Si/SiO_2 substrate (alternatively, deposit/pattern catalyst on substrate and CVD-grow nanotubes in furnace).
- Image substrate using atomic force microscope (AFM) to locate nanotubes.
- Design pattern based on AFM image; write leads using electron beam (e-beam) lithography.
- Evaporate metal, lift-off, measure.

This procedure has been used to obtain the bulk of nanotube data in literature. Electrical contact has been made to clean-enough segments, forming quantum dots and interesting physics has been observed in metallic nanotubes (as summarized in Chapter 1). However, quantum dot behavior in semiconducting nanotubes had not been observed for a long time. Figures 2.1 and 2.2 show typical data obtained from two metallic and semiconducting nanotubes, respectively, of similar lengths.

The difficulty in obtaining ballistic data from semiconducting nanotubes can be attributed to the so-called pseudo-spin, as was elucidated by McEuen and co-workers [23]. Recall from Chapter 1 that the electronic structure of nanotubes consists of two bands, crossing at the two Dirac points in the case of metallic nanotubes. Each band can be attributed to arising from either the bonding or anti-bonding molecular orbital of graphite. This degree of freedom is called the pseudo-spin. Inter-band scattering at each Dirac point is prevented in metallic nanotubes since the molecular states corresponding to the two bands

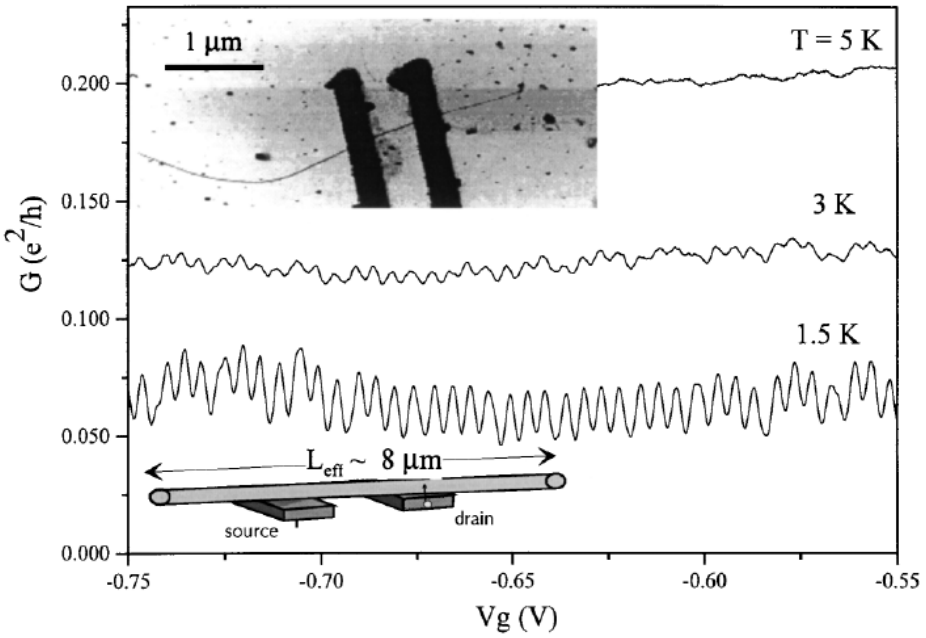

Figure 2.1. Transport data from a metallic nanotube on substrate. [23]

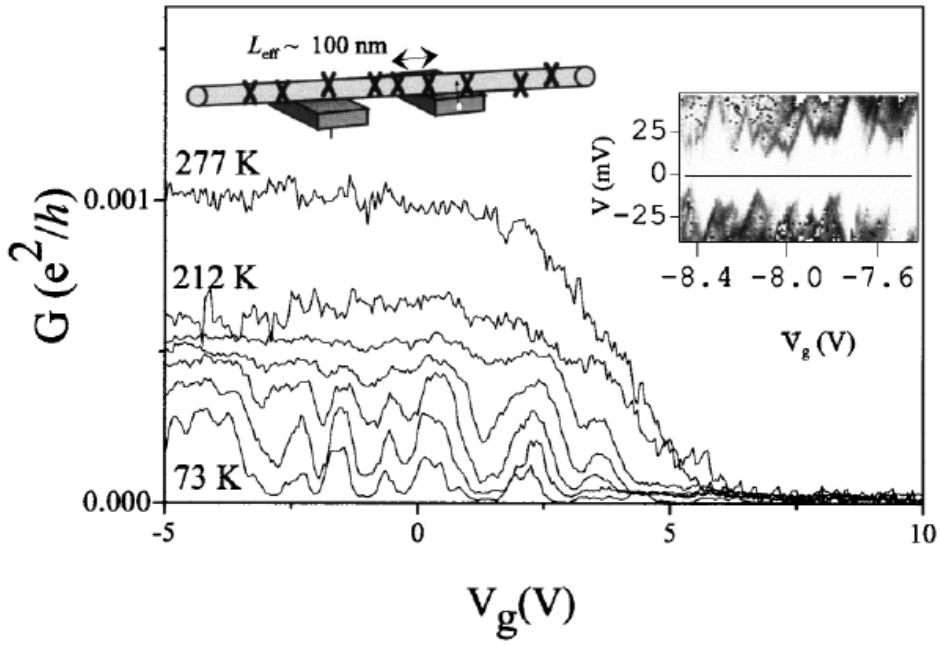

Figure 2.2. Transport data from a semi-conducting nanotube on substrate. [23]

are orthogonal. In semiconducting nanotubes however, the electronic states are a mixture of both bands and scattering is only partially suppressed. This is shown schematically in Figure 2.3. The scattering matrix element should scale with the bandgap. Note that this is the response of the system to long-range disorder (such as that arising from inhomogeneities on the substrate); short-range (atomically-sharp) disorder will cause inter-band scattering in both metallic and semi-conducting nanotubes.

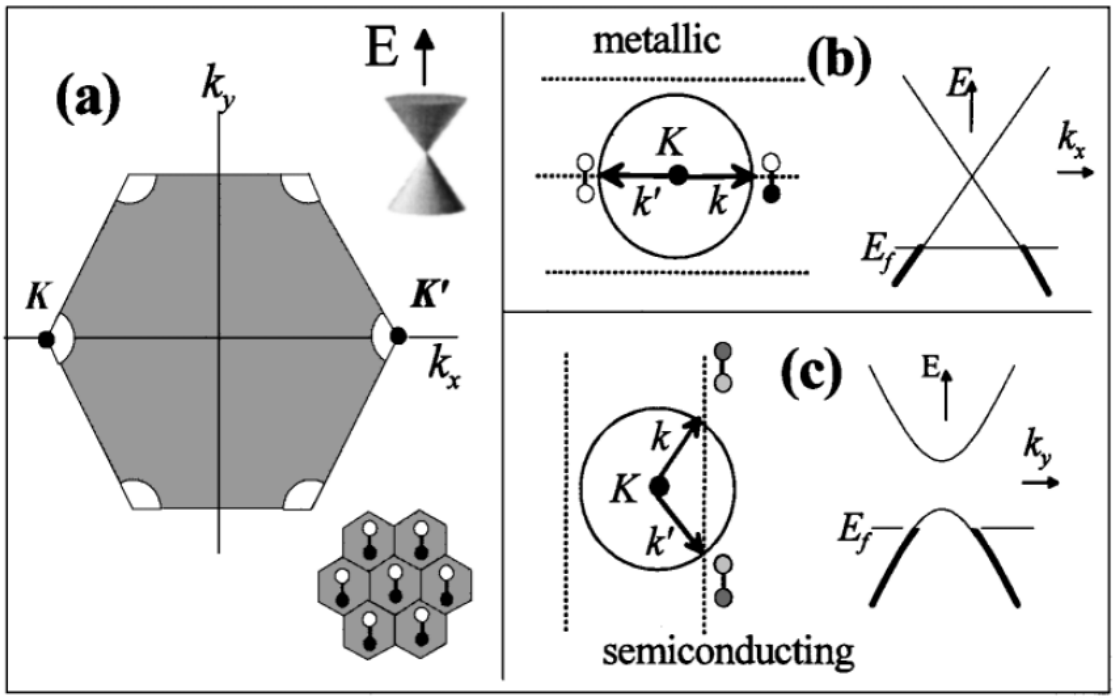

Figure 2.3. The Brillouin zone of graphene is shown in **(a)**. **(b)** shows the difference in molecular states in metallic and semiconducting nanotubes. [23]

In 2004, a few-electron quantum dot was reported from Delft in one semiconducting nanotube, suspended after fabrication to avoid disorder from the substrate [28]. In 2005, clean data was reported from Stanford in small-bandgap nanotubes grown in-place on top of leads and in a suspended geometry [7]. From my trials, results in devices suspended after fabrication have not been encouraging. We decided to use the latter technique with the aim of obtaining clean data in semi-conducting nanotubes, since these were the devices most likely to host the Wigner crystal.

I have also used other techniques of device fabrication during the course of this thesis, such as depositing nanotubes from solution on top of thick leads to achieve a suspended geometry or (AC and DC) dielectrophoresis of nanotubes in solution to trap one (or few) nanotubes across leads. However, none of these yielded the clean data obtained from the procedure detailed below:

Fabrication procedure

1. The substrate is a p-doped Si/SiO_2 (500 nm)/Si_3N_4 (50nm) wafer (see Figure 2.4 for geometry). The first lithography step is for the trench over which the nanotube will be suspended. Depending on the size of the trench, e-beam or optical lithography is used to pattern the trench. The nitride is then reactive-ion etched all through. If a metal layer needs to be evaporated for a local gate, the etching should be isotropic, so as to create an undercut in the nitride below the resist. Even though this removes more material than the size of the window, metal does not stick to the nitride walls of the trench. The oxide is then wet-etched, about 300 nm deep. If etched all the way, there can be problems with random nanotubes growing from the lead into the trench and shorting the back gate (i.e., doped Si).

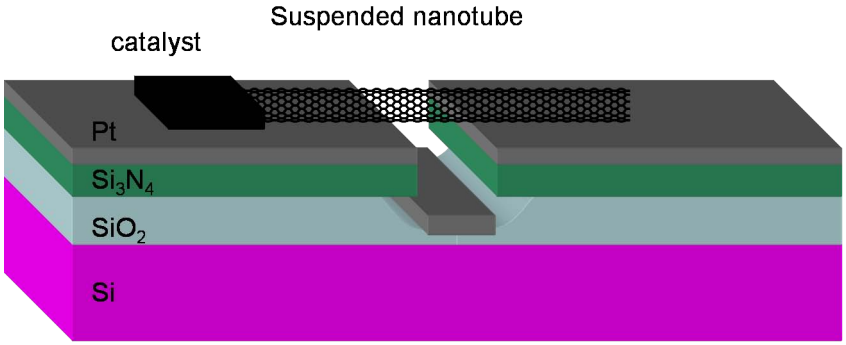

Figure 2.4. Fabrication geometry

2. The second lithography step involves patterning the leads across the trench using photo-lithography (using a bilayer resist for undercut), depositing metal (most commonly, Pt with W sticking layer) and subsequent lift-off.

3. The next step involves patterning islands on the Pt leads, some distance away from

the trench. This process is done using photo-lithography. A solution of catalyst nano-particles (see section **Catalyst** for more details) is then spun on the sample. The yield of nanotubes successfully crossing the trench is a sensitive function of the density of catalyst material and the distance of the island from the edge of the trench. Unfortunately, the best solvent for the catalyst is methanol, which was incompatible with photoresist. I had to live with making catalyst in water, which does not dissolve it well and hence there is less control on catalyst density. The catalyst is dried on a hot plate, lifted off using agitation and ultra-sounded for variable amounts of time to achieve some control on density.

4. CVD growth of SWNTs [10] involves the high-temperature decomposition of the feedstock material (see section **Feedstock gas**) on the surface of the catalyst to carbon, which is released by the catalyst in the form of a nanotube (the lowest energy configuration). The nanotubes drift (mostly in the direction of the flow) for a short distance, typically a few μms, before they stop growing. CVD growth is carried out in a 1 inch furnace with either methane, ethanol or ethylene as feedstock gas, along with H_2 and Ar co-flows in varying concentrations and various temperatures between 800 and 900 C. Temperature does not seem to be critical, as long as it is high. Samples are baked in air before and after growth. However, the outcome/data obtained was similar even when this step was not carried out.

5. Devices are first probed in air at low bias ($\sim k_B T$) on our home-built probe station to detect electrically connected pairs of leads. Metallic and semiconducting nanotubes have typical low-bias resistances $\propto$ length L (plus contact resistance, which depends on the specifics of the procedure and nanotube bandgap, but typically $\sim$ 25 kΩ for metallic and $\sim$ 100 kΩ for semiconducting) and differing by a factor of a few. The length-dependence arises from acoustic phonon scattering. The difference in resistance between metallic and semiconducting nanotubes can only be partly attributed to the difference in contact resistance. Temperature dependence of resistivity ρ shows linear behavior (unpublished data) characteristic of phonon scattering, with co-efficient $\frac{d\rho}{dT}$ larger for semi-conducting than metallic nanotubes, again indicating enhanced scattering in semi-conducting nanotubes. Single nanotube devices are then selected for wire-bonding, and a more stringent screening at high bias.

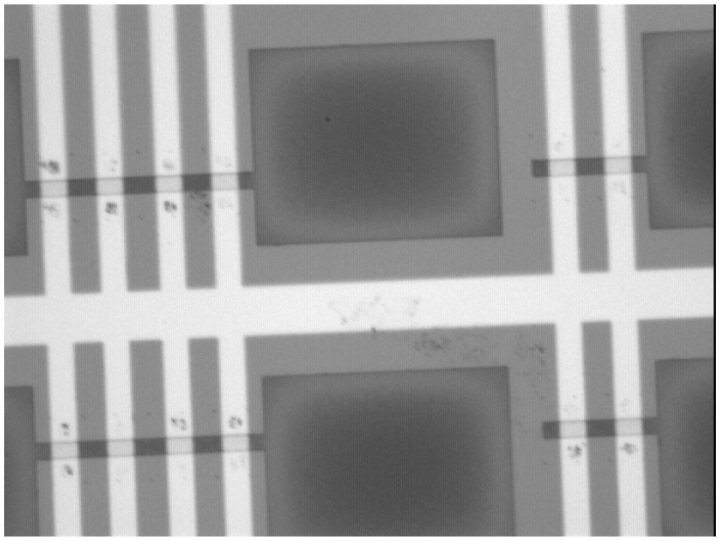

Figure 2.5. Optical micrograph of the layout of devices: the dark spots are catalyst islands on Pt leads.

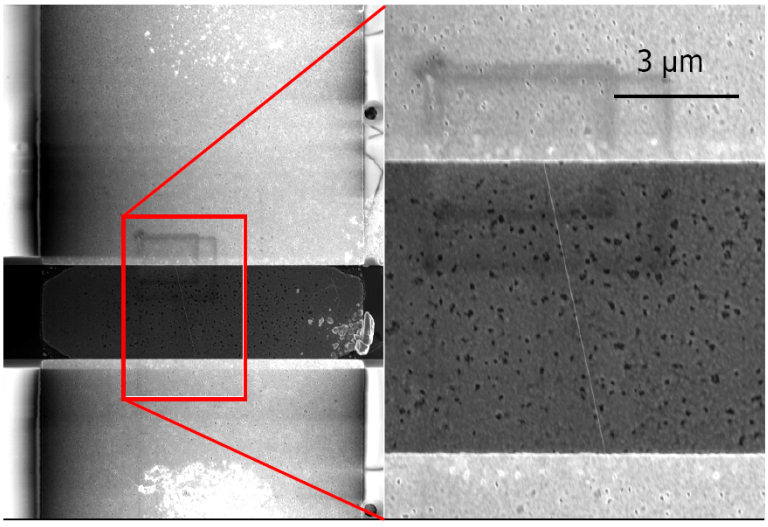

Figure 2.6. SEM image of a typical device: the right image is a zoomed-in version of the red square in the left image.

6. Devices selected from probing, which have resistances in the range expected for single tubes, are wire-bonded and measured in argon gas at high bias. At high bias (typically up to 1.5–2 V), all shells of the nanotube carry current, roughly in equal amounts. In particular, suspended SWNTs have a characteristic maximum current of $\sim 10/L$ μA, where L is the length of the device in μm, as was observed in [36]. This can be attributed to a heating-induced current-limiting process since the power I^2R scales as $1/L$, consistent with 1D conduction of heat which yields a $P \propto 1/L$ dependence. Electrical heating is investigated in more detail in Chapters 6 and 7 using Raman and transport spectroscopy, respectively. High bias enables one to pick out the single-tube single-wall devices with certainty. Each (5 mm $\times$ 5 mm) chip typically has $\sim$ 50 pairs of leads of which, on average, about 5 are single devices. However, this number drops for longer devices. For our 10 μm long suspended samples, we either saw bundles or nothing. Figures 2.5 and 2.6 are optical and SEM images of the layout and a representative device, respectively.

I wire-bonded and characterized about 1000 devices at high bias and studied about a hundred of the cleanest ones in the cryostat over various cool-downs. Figure 2.7 shows conductance G versus gate voltage V_g for a representative "clean" device, with a measured gap $\sim$ 220 meV at 1.4 K and different axial magnetic fields, obtained using a low-frequency lock-in technique, to be compared with typical data on substrate from a similarly long semiconducting nanotube (Figure 2.2).

In addition, the following factors are crucial for the growth process:

Contact metal

The choice of contact metal is important since the metal should have a favorable work-function, wetting characteristics, support nanotube growth, survive the high temperatures involved in the growth process and not alloy with carbon or any of the other materials involved in growth. In this work, the metals used included Au, Mo, Pd, Pt and W. While Pt was the material reported by the Dai group, the user facility at Caltech did not have an e-beam evaporator. Even though Au melts at the high growth temperatures, I was able to successfully grow devices using a thick enough ($\sim$ 200 nm) Au layer. However, Au

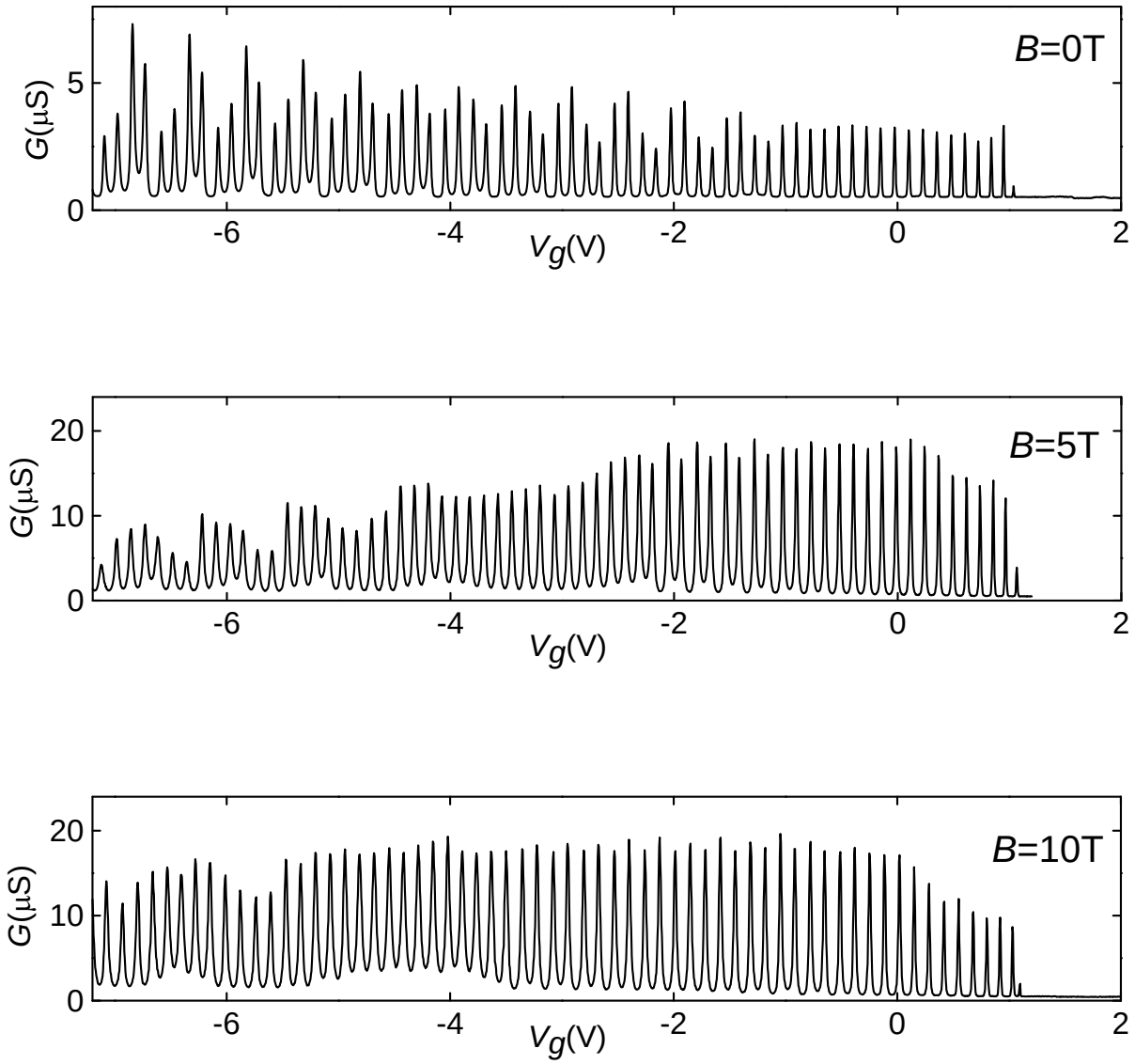

Figure 2.7. Conductance G versus gate voltage V_g for a clean device with a measured energy gap $\sim$ 220 meV at 1.4 K

tended to accumulate a lot of soot and the resulting devices were mostly disordered at low temperatures. Pd is reported to make ohmic contacts when evaporated on top of nanotubes, but I found it to be unsuitable as a growth substrate. In fact, the Pd leads were found to grow their own tubes! After testing Pt leads evaporated by the Scherer group, subsequent evaporations and related wafer-scale processing (steps 1 and 2 of the fabrication procedure) were carried out at the nanofab in UC Santa Barbara. In addition, I also used Mo and W in the hopes of making n-type and electron-hole symmetic contacts to nanotubes. However, these metals had bad wetting characteristics and these attempts were largely unsuccessful.

Catalyst

The commonly used catalyst is the Fe/Mo salt mixture with alumina nanoparticles dispersed in methanol, as developed by the Dai group [10]. However, this catalyst is not compatible with photoresist. The catalyst used in this work was made in water with varying amounts of Fe and Mo salts. It was reported in [42] that different ratios of Fe and Mo salts produced nanotubes with different average radii. While AFM radius measurements are not possible with the suspended geometry, the radial breathing phonon mode (RBM, which directly yields nanotube radius) in our Raman measurements from resonant nanotubes correlates with this observation. For most of the growth, I used two Fe/Mo salt ratios by weight:

- (Fe:Mo) 20:1.5 mg for small ($\lesssim$ 1 nm) radius nanotubes for Raman measurements (otherwise the RBM frequency, which goes as 1/radius, is cut off by the notch filter)
- (Fe:Mo) 20:4.5 mg for large ($\gtrsim$ 1 nm and up to 5 nm) radius nanotubes for magnetic flux threading measurements

Feedstock gas

Methane, ethylene and ethanol were used as feedstock gases in the CVD process. The growth process involves ramping up the temperature of the furnace to the growth temperature (800–900 °C) with 0.2 and 0.4 standard liters per minute (SLM) flows of H_2 and Ar, flowing the carbon feedstock for 2–10 minutes depending on the length of nanotube samples required, flusing the furnace with 2 SLM of H_2 and cooling down with Ar flow. With methane as the feedstock, I used variations of recipes developed by other groups to get clean nanotubes. In

particular, the combination developed at Delft of (H_2:CH_4) 0.7:0.52 SLM worked well. Too little H_2 led to noticeable amorphous carbon and disordered devices. My attempts with C_2H_4, even with trace amounts, yielded disordered devices. Ethanol was reported by the Columbia group to grow mm-long nanotubes [43]. My SURF trainee, Scott Hsieh, and I built an ethanol bubbler setup, and tried various mixtures of Ar gas bubbled into ethanol with co-flow of H_2. The combination H_2:Ar of 0.075:0.175 SLM worked best; all of the long nanotubes reported in Chapter 6 and some of the clean quasi-metallic quantum dots in Chapter 5 were made using ethanol.

If anything can go wrong, it will

Anybody who has worked on experiments will know what I am talking about here, but the sheer amount of time I spent on these issues makes me list them, with the hope that future experimenters working on this system will learn from my mistakes.

- Commercially available ethanol is denatured by adding small amounts of contaminants. We found this was bad for growth only after measuring the resulting devices with transport and Raman, where we found multiple quantum dot behavior and the defect (D) band, respectively. We obtained better results after switching to non-denatured alcohol (for which we paid food tax).

- Another problem was that, typically, for an individual nanotube crossing the trench, many others fell into the trench on the metal at the bottom (see Fig. 2.4), shorting the lead with the metal. This charged metal screened the nanotube from the back gate, making these devices useless for most measurements. This happened in almost 50% of the devices. One will need a different fabrication design to overcome this issue.

- Clean devices require extremely clean growth conditions and the slightest presence of impurities can lead to disordered devices. While I was quite diligent about regularly making new catalyst, replacing the alcohol, cleaning the furnace, etc., there was one very frustrating period when I could not obtain clean data in spite of changing every variable of the growth process (and there are a lot of them!). This was finally traced to a minute leak in the gas setup.

Chapter 3

Interacting Electron States in Carbon Nanotubes: Theory

Electron-electron interactions have a profound effect on the properties of solids. Under certain conditions, they are known to be responsible for such exotic behavior as the fractional quantum Hall effect (FQHE) and high-temperature superconductivity in two- and three-dimensional (2D and 3D) materials, respectively. In general however, in 2D and 3D interactions are well accounted for by Landau's Fermi liquid theory. In this theory, low-energy excitations of an interacting electron gas can be described in the same way as the Drude or Sommerfeld theory of non-interacting electrons; there is a one-to-one correspondence between non-interacting electrons and "dressed" quasiparticles of the Fermi liquid theory.

In 1D, Fermi liquid theory breaks down even for *arbitrarily* weak interactions [2]. This can be understood from the linear dispersion that arises in such conditions, where energy and momentum conservation are essentially the same. This leads to large available phase-space for electron scattering, in turn causing a vanishing lifetime for the quasiparticle. The low-energy excitations of such a *Luttinger* liquid are bosonic in nature and comprise of charge and spin excitations (plasmons and spinons) propagating independently of each other (a phenomenon known as spin-charge separation). Indeed, Luttinger liquid behavior has been observed in clean 1D systems such as carbon nanotubes [3] and edge states of the FQHE liquid [5]. Spin-charge separation has been observed in parallel tunnel-coupled semiconductor quantum wires [44].

The Luttinger liquid has certain conditions for validity, such as linear energy dispersion and the inclusion of only forward-scattering electron-electron interactions. Relaxing these conditions can lead to qualitatively different behavior. In this chapter, the Luttinger liquid formulation in carbon nanotubes is described in Section 3.1. In Section 3.2, it is shown

that introducing a curvature in the dispersion leads to the 1D Wigner crystal ground state. In Section 3.3, it is shown that including electron-electron back-scattering interactions at half-filling (umklapp scattering) for metallic nanotubes results in a Mott insulating ground state.

1D systems are special, in that Coulomb interactions cannot be described using perturbation theory [2]. Instead, one uses the equivalence of bosons and fermions in 1D, in a field theoretical technique called bosonization. This chapter will use bosonization terminology to describe mathematically the various processes involved in clean systems. Knowledge of this technique is not necessary to understand the contents of this chapter; however, the interested reader is guided to excellent references on bosonization [2, 45, 46].

3.1 Luttinger liquid formalism

Electron bands in metallic single-wall nanotubes form two pairs (i=1,2) of spin-degenerate ($\alpha = \uparrow, \downarrow$) right- (R) and left- (L) moving branches intersecting at the band center, as shown in Chapter 1. The Hamiltonian, without considering interactions, has the form [2]:

$$H_0 = -i\hbar v_F \int dx \sum_{i\alpha} \Psi^\dagger_{i\alpha} \sigma_3 \partial_x \Psi_{i\alpha} \tag{3.1}$$

where Ψ is a two-component wave-function $\Psi = [\psi^R \psi^L]^\dagger$, σ_3 is the Pauli matrix, v_F is the Fermi velocity and x is the co-ordinate along the nanotube. In the procedure of bosonization, where an electron is described in terms of an infinite number of bosons, one introduces a bosonic displacement field θ and phase field ϕ, such that $\rho(x) = \partial_x \theta(x)/\pi$ is the charge density and $p = \partial_x \phi(x)/\pi$ is the momentum conjugate to θ. One writes $\psi^{R,L}_{i\alpha} \sim e^{i(\phi_{i\alpha} \pm \theta_{i\alpha})}$ where the dual fields satisfy $[\phi_{i\alpha}(x), \theta_{j\beta}(y)] = -i\pi\delta_{i\alpha}\delta_{j\beta}\Theta(x-y)$. Expressed in these variables, Equation 3.1 takes the form $H_0 = \sum_{i\alpha} \mathcal{H}_0(\theta_{i\alpha}, \phi_{i\alpha})$ where

$$\mathcal{H}_0(\theta, \phi) = \frac{\hbar v_F}{2\pi} \int dx [(\partial_x \theta)^2 + (\partial_x \phi)^2]. \tag{3.2}$$

This Hamiltonian describes a bosonic wave propagating at velocity v_F, as can be verified by using the commutation relations to obtain the equations of motion, $\partial_t^2 \theta = v_F^2 \partial_x^2 \theta$ and similarly for ϕ.

Interactions are included in the $forward-scattering$ approximation, in which only pro-

cesses involving small momentum transfer are considered. Interbranch scattering processes (such as backscattering and umklapp) involve a momentum transfer of order $2k_F \sim 1/a$, where a is the carbon-carbon bond length. These processes are dominated by the short-range part of the interaction, at distances $r \sim a$, where the interaction changes significantly from site to site. Such processes are ignored by using a short-range cutoff, $2r$, the diameter of the nanotube. Furthermore, long-range interactions are assumed to be screened on a scale R_s, which is long compared to the radius r but short compared to the length of the nanotube. Modeling the nanotube as enclosed by a cylinder of radius R_s, the energy to charge the nanotube with an electron density $e\rho_{tot}$ is

$$H_{int} = e^2 ln(R_s/r) \int dx \rho_{tot}^2. \tag{3.3}$$

Since H_{int} involves only charge, one introduces a spin and band decomposition via $\theta_{i,\rho/\sigma} = (\theta_{i\uparrow} \pm \theta_{i\downarrow})/\sqrt{2}$ and $\theta_{\mu\pm} = (\theta_{1\mu} \pm \theta_{2\mu})/\sqrt{2}$, with $\mu = \rho, \sigma$ and similar definitions for ϕ. Now, the branch $\rho+$ is charged while the other three branches ($\rho-$, $\sigma+$, $\sigma-$) are neutral. One can write the Hamiltonian only for the charge sector as $\mathcal{H}_\rho = \mathcal{H}_0(\theta_{\rho+}, \phi_{\rho+}) + H_{int}(\theta_{\rho+})$, and may be written as

$$\mathcal{H}_\rho(\theta_{\rho+}, \phi_{\rho+}) = \frac{\hbar v_\rho}{2\pi} \int dx [g^{-1}(\partial_x \theta_{\rho+})^2 + g(\partial_x \phi_{\rho+})^2]. \tag{3.4}$$

This describes the 1D acoustic plasmon which propagates with velocity $v_\rho = \sqrt{v_F[v_F + (8e^2/\pi\hbar) ln(R_s/r)]}$ and is characterized by the Luttinger parameter $g = v_F/v_\rho \sim 0.2$ for nanotubes. The neutral modes are unchanged by interactions and propagate at v_F. Thus the charge mode travels ~ 5 times faster than the neutral modes. This describes the well-known spin-charge separation.

The above treatment makes two important assumptions which we shall now relax:

- Linear energy dispersion, and long-range cutoff at a distance R_s much smaller than nanotube length.

- Neglect of back-scattering processes, i.e., short-range cutoff at the diameter $2r$, larger than inter-atom spacing.

3.2 Inclusion of band-curvature: The 1D Wigner crystal

The Hamiltonian from the previous section is modified to account for the absence of screening, so that the Fourier component of the (truly) long-range interaction reads $V(q) = \int V(x)e^{iqx}dx = e^2 ln[(qr)^{-2} + 1]$. Now,

$$H_0 = -i\hbar v_F \int dx \sum_{j=0}^{3} \Psi_j^\dagger \sigma_3 \partial_x \Psi_j + \frac{1}{2}\sum_q \rho_q V(q) \rho_{-q} \tag{3.5}$$

with the summation over j being the four modes as in the previous section. As shown by Levitov and Tsvelik [47], band curvature (relevant for small-bandgap and semiconducting nanotubes) is included by adding to the above Hamiltonian a back-scattering term

$$\mathcal{V}_{ext} = \Delta_0 \int dx \sum_{j=0}^{3} \Psi_j^\dagger \sigma_1 \Psi_j \tag{3.6}$$

where Δ_0 is the band-gap of the nanotube.

In computing quantities relevant for transport, *e.g.*, tunneling density of states, one considers the classical action, S, which can be written in terms of the Lagrangian $\mathcal{L}$ as $S = \int dx d\tau \mathcal{L}$, in imaginary time τ where

$$\mathcal{L} = \frac{i}{\pi}\partial_\tau \phi \partial_x \theta + H(\phi, \theta). \tag{3.7}$$

The Lagrangians corresponding to H_0 and $\mathcal{V}_{ext}$ become

$$\mathcal{L}_0 = \frac{\hbar v_F}{2\pi}\left((\partial_t \phi^0)^2 - K\,(\partial_x \phi^0)^2 + \sum_{a=1}^{3} (\partial_\mu \phi^a)^2 \right), \tag{3.8}$$

$$\mathcal{L}_{ext} = -\lambda \left(\prod_{a=0}^{3} \cos \phi^a + \prod_{a=0}^{3} \sin \phi^a \right) \tag{3.9}$$

where λ is a renormalized coupling constant related to the band-gap Δ_0 by $\lambda = K\Delta_0^2/(4\pi\hbar v_F)$ and $K = g^{-2}$ (g is the Luttinger parameter) is the "stiffness" of the charge mode, related to the inter-carrier interaction potential and usefully approximated by a constant $\sim$ 20–40.

This is the well-studied sine-Gordon Lagrangian (the first correspondence between massive 1D fermions and the sine-Gordon model was made by Coleman [48] and Mandelstam [49] in 1975). Adding an electron to the system corresponds to creating a sine-Gordon soliton.

The excitation gap of such a system is given by the energy of the soliton. The difference in velocities between the charge and neutral (flavor) sectors leads to a separation of energy scales with the charge gap (measured energy gap) Δ being stiffer than the flavor gap by a factor $K^{1/2}$; the flavor gap, $\approx \Delta_0$, is relatively unaffected by interactions. The charge soliton is confined in space to a region (width w_ρ) related to Δ by $w_\rho \sim \hbar v_\rho/\Delta$, where $v_\rho = K^{1/2} v_F$ is the charge mode velocity. The flavor soliton width is $w \sim K^{-1/2} w_\rho$.

One can think of solitons as a competition between the kinetic energy of localization, arising from $\mathcal{L}_0$, which favors extended electrons, and the potential energy due to the presence of a bandgap, $\mathcal{L}_{ext}$ which favors point-like electrons. As a result of the competition, the electron is localized within a finite region of space, *i.e.*, the soliton width. For a multiple electron system, the minimum energy configuration is a 1D lattice of solitons as shown in [47]. This is a realization of the 1D Wigner crystal.

3.3 Inclusion of umklapp scattering: The Mott insulating state

In general, backscattering interactions require the presence of atomically sharp impurities, which are seen to be absent in clean samples. However, at commensurate filling of energy bands, umklapp scattering is a viable backscattering mechanism. Such a process, where the initial and final electron momenta differ by a reciprocal lattice vector, is governed by the short-range part of the Coulomb interaction.

In this section, we consider the effect of umklapp scattering in *metallic* nanotubes, at half-filling of energy bands. As discussed first by Balents and Fisher [50] and further by Lin [51], one can establish equivalence between a nanotube and a two-chain version of the 1D Hubbard model (also known as a two-leg ladder) as shown in Fig. 3.1 for an armchair nanotube. The on-site interaction strength is averaged over the atoms along the circumference (because the electrons are delocalized around the circumference of the nanotube, and hence occupy the same site with reduced probability). One then accounts for long-range interactions in the same way as the previous section.

The Lagrangian for a metallic nanotube at half-filling has the form $\mathcal{L} = \mathcal{L}_0 + \mathcal{L}_{umk}$,

where $\mathcal{L}_0$ is the same as in the previous section

$$\mathcal{L}_0 = \frac{\hbar v_F}{2\pi}\left((\partial_t\phi^0)^2 - K\,(\partial_x\phi^0)^2 + \sum_{a=1}^{3}(\partial_\mu\phi^a)^2\right), \tag{3.10}$$

and the backscattering part [52]

$$\mathcal{L}_{umk} = D\sum_{a=1}^{3} V_a \cos 2\phi^0 \cos 2\phi^a. \tag{3.11}$$

The long-range part of the interaction stiffens the charge mode by a factor $K^{1/2}$ as in the previous section, V_a is the short-range part scaled down by $1/N$ (N is the typical number of atoms along the circumference)

$$V_a = (e^2/\hbar v_F)/N \propto 1/r \tag{3.12}$$

and $D \simeq \hbar v_F/r$ is the 1D bandwidth.

This is also a sine-Gordon problem with soliton solutions. The magnitude of the resulting *Mott* gap is given by the energy of the charge soliton. Calculations [53] show that long-range interactions give a non-trivial scaling to the Mott gap with nanotube radius r,

$$\Delta_{Mott} \propto \frac{1}{r^{1/1-g}} \tag{3.13}$$

where g is the usual Luttinger parameter $\sim$ 0.2–0.3 in nanotubes.

The two-leg ladder is known to be a special type of Mott insulator, known as a spin-liquid Mott insulator, with gapped neutral excitations [54]. Theories [50, 51, 53, 55, 56] predict a similar ground state for nanotubes. The nanotube Mott state is predicted to have neutral excitations (corresponding to the three neutral modes) smaller than the Mott gap by a factor of the order g due to the effect of long-range interactions [53, 56].

Phase diagram of carbon nanotubes

Upon considering interactions as detailed in this chapter, the phase diagram of appropriately long carbon nanotubes looks as shown in Figure 3.2. In nanotubes with a bandgap, there is a crossover from a 1D Wigner crystal to a Luttinger liquid as a function of doping. In

metallic nanotubes, there is a quantum phase transition from a Mott insulator to a Luttinger liquid on adding an electron.

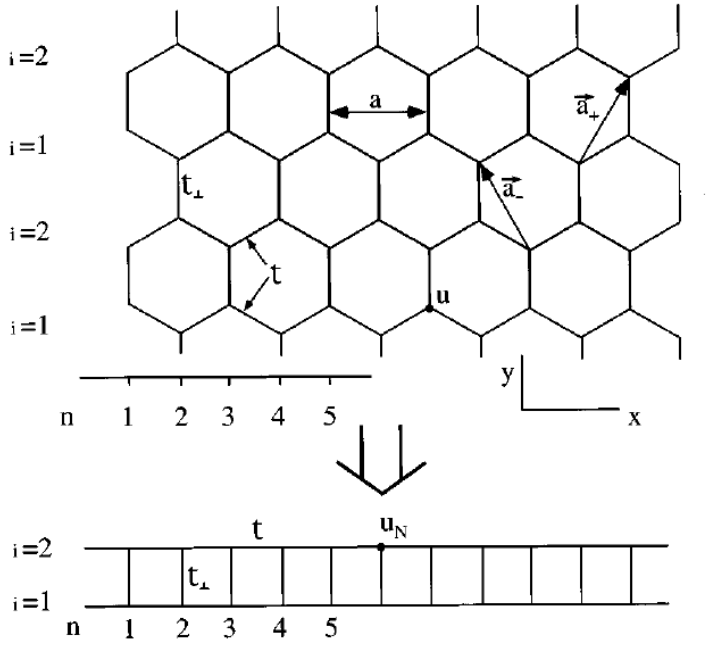

Figure 3.1. Short-range interactions on an armchair nanotube shown to be the equivalent of a two-chain Hubbard model. [50]

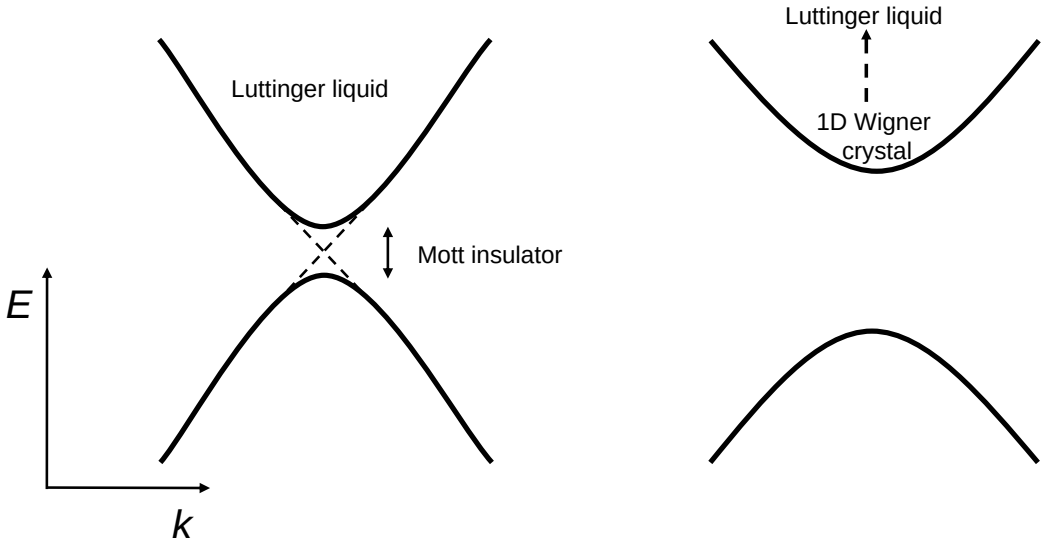

Figure 3.2. Phase diagram of electrons in metallic (left) and semiconducting (right) carbon nanotubes

Chapter 4

The One-Dimensional Wigner Crystal in Carbon Nanotubes

Abstract

A dilute system of electrons interacting through long-range Coulomb forces has been predicted to form a periodic solid known as a Wigner crystal. We demonstrate using low-temperature single-electron transport spectroscopy that a hole gas in low-disorder carbon nanotubes with a band gap is a realization of the one-dimensional Wigner crystal. In an axial magnetic field, we observe three distinct regimes of spin and isospin polarization as carrier density is varied. We explain these regimes using a Wigner crystal picture based on a gapped Luttinger liquid model, with the carriers represented by spatially localized solitons. Our observation can lead to unprecedented control over the behavior of the spatially separated system of carriers, and could be used to realize solid state quantum computing with long coherence times.

Electron-electron interactions strongly affect the behavior of low-dimensional systems. In one dimension (1D), arbitrarily weak interactions qualitatively alter the ground state producing a Luttinger liquid (LL) [2] which has now been observed in a number of experimental systems [3–5, 57, 58]. Interactions are even more important at low carrier density, and in the limit when the long-ranged Coulomb potential is the dominant energy scale, the electron liquid is expected to become a periodically ordered solid known as the Wigner crystal [59]. In 1D, the Wigner crystal has been predicted to exhibit novel spin and magnetic properties not present in an ordinary LL [20, 60–63]. However, despite recent progress in coupled quantum wires [64, 65], presence of disorder has precluded unambiguous experimental demonstration of this state.

Carbon nanotubes are high mobility quantum wires that may enable the study of the intrinsic properties of the 1D electron gas without significant disorder. Individual-nanotube transport experiments have demonstrated Coulomb blockade [24, 25] and Kondo physics [26], down to the few-electron-hole regime [7, 28, 29]. These experiments have generally been interpreted using the orthodox model and four-fold shell-filling. However, deviations have been noted at low density [7, 28], suggesting the importance of electron-electron interactions. In 1D, the ratio of inter-electron Coulomb energy to kinetic energy scales as $1/(na_B)$, where n is the carrier density, $a_B = \epsilon\hbar^2/me^2$ is the Bohr radius, ϵ is the dielectric constant, e is the electric charge, $\hbar$ is Planck's constant, and m is the electron effective mass. On the basis of this order-of-magnitude estimate (see *e.g.* ref. 9), the Coulomb energy becomes dominant and the system should begin to cross over to a strongly interacting regime at $n \sim {a_B}^{-1} = me^2/\epsilon\hbar^2$. Thus, nanotubes with larger bandgap and hence effective mass are more favorable for the observation of the Wigner crystal state; yet to date most studies in the few-electron regime have been done on nanotubes with relatively small gaps (<100 meV).

We report axial magnetic field measurements on low-disorder carbon nanotubes with larger bandgaps than previous studies. We observe for the first time three distinct regimes as a function of carrier density and magnetic field: (I) a completely spin and isospin polarized state, (II) an isospin polarized, spin antiferromagnetic state, and (III) an unpolarized state with a four-fold addition energy period. The transitions among these regimes can be quantitatively and intuitively explained using a Wigner crystal picture based on a gapped LL model [47]; the carriers are represented by spatially localized soliton solutions of the theory. The value of the soliton width we obtain from our analysis, corresponding to the spatial extent of the carrier wavefunctions, agrees with theoretical estimates [47, 66]. Surprisingly, we observe a sudden quenching of the Kondo effect for odd hole states as the magnetic field is tuned through the transition from the antiferromagnetically ordered regime to the four-fold filling regime. This can be understood based on the formation of large spin states with spin $S \geq 3/2$ resulting from the interplay between the spin and isospin degrees of freedom in the Wigner lattice.

Nanotubes with a bandgap are known to be more susceptible to disorder than metallic nanotubes [23]. Our fabrication procedure, based on Cao et al. [7], is designed to reduce disorder by growing nanotubes in a suspended geometry to eliminate perturbations from

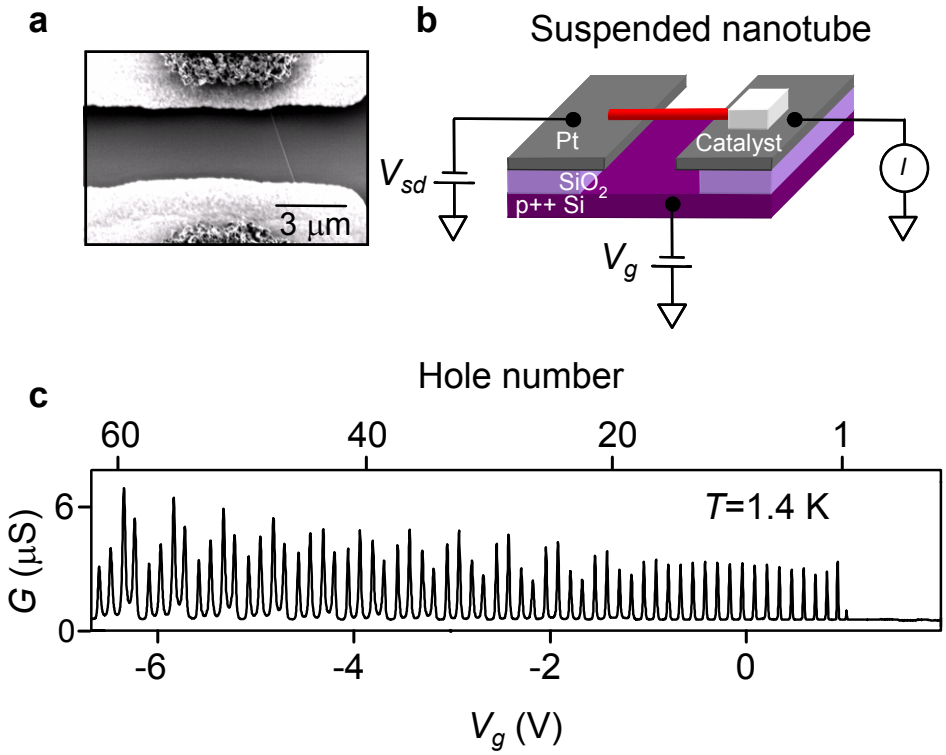

Figure 4.1. Experimental geometry and characteristic transport data. **(a)** Scanning electron microscope image of a representative suspended nanotube device. Samples are fabricated by chemical vapor deposition growth of single-walled carbon nanotubes, from lithographically defined Fe-Mo catalyst islands [10] across predefined Pt electrodes [7], by flowing a gas mixture of methane (0.5 SLM) and hydrogen (0.7 SLM) at 800 °C for 5 min. Devices are first studied at room temperature in an inert environment and the gate voltage and high bias (up to 1.5 V) electrical transport characteristics are recorded. Devices determined to have a bandgap and that show negative differential conductance at high bias with a maximum current of $\sim 10/L$ μA (where L is the known device length in μm), corresponding to individual, suspended, single-wall nanotubes [36], are then selected for low-temperature measurement. **(b)** Schematic of device geometry showing nanotube with attached source, drain, and doped Si gate electrode ~600 nm below the nanotube. **(c)** Conductance versus gate voltage for a 500 nm long device at temperature T=1.4 K.

the substrate and directly over metal contacts in order to avoid disorder due to chemical processing. Fig. 4.1(a) shows a scanning electron microscope image of a representative device, while Fig. 4.1(b) shows a schematic diagram of our devices, consisting of a nanotube with attached source, drain and gate electrodes.

At low temperatures, we typically observe Coulomb peaks in the conductance G versus the gate voltage V_g, when each additional hole is added to the nanotube dot. Fig. 4.1(c) shows such G versus V_g data taken at temperature $T = 1.4$ K from a device D1 with length 500 nm. V_g >1 V depletes the nanotube, placing the Fermi level in the bandgap. The regularity of the Coulomb peaks indicates that we are studying a single quantum dot that is essentially free from disorder and pinning. Non-linear transport spectroscopy results for D1 are shown in Figure 4.2(a) as a color-scale plot of dI/dV versus source-drain bias V and V_g. The data exhibits Coulomb blockade diamonds, shown by the dashed lines, and analysis of the data yields a charging energy $U \sim$10 meV, consistent with that expected for a 500 nm-long nanotube dot. We also measure the scale factor α between energy and V_g and find for D1 $\alpha \approx 14$. Using the value for α and a measurement of G versus V_g over the bandgap, we infer the bandgap 2Δ, which for D1 was found to be $\sim$220 meV.

Each Coulomb peak corresponds to the addition of a hole, with both a physical spin and an isospin that corresponds to its sense of the orbital motion around the tube waist [29]. In a magnetic field B, the increase in ground state energy from each hole shifts by the sum of contributions E_{orb} from its orbital magnetic moment [7, 29] and the Zeeman energy E_Z from the hole spin [67]. These energies are given by $E_{orb} = \pm\mu_{orb}B = \pm rev_F B/2 \approx \pm 0.41\text{meV}B[\text{T}]r[\text{nm}]$ [7, 29], and $E_Z = \pm g\mu_B B/2 \approx \pm 0.058B[\text{T}]$ meV, where μ_B is the Bohr magneton, r is the tube radius, e the electric charge, v_F the Fermi velocity, $g \approx 2$ is the electron g-factor. As the position of Nth Coulomb peak in V_g is α times the energy difference between the N and $N+1$ hole ground states, we determine the spin and isospin of each added hole by applying B parallel to the tube axis (Fig. 4.2(b)) and studying the Coulomb peaks' shifts versus B. Our results are plotted in Fig. 4.2(c), which shows a color-scale plot of G vs. B and V_g from D1. (Line traces of G versus V_g for various $B > 0$ were shown in Fig. 2.7).

Three distinct regimes are evident. For peak numbers N up to $\sim$12, their evolution is nearly parallel from near $B = 0$ T up to $B = 8$ T, shifting to larger V_g for larger B (positive slope). This region is referred to as region I. At more negative V_g, the slopes alternate

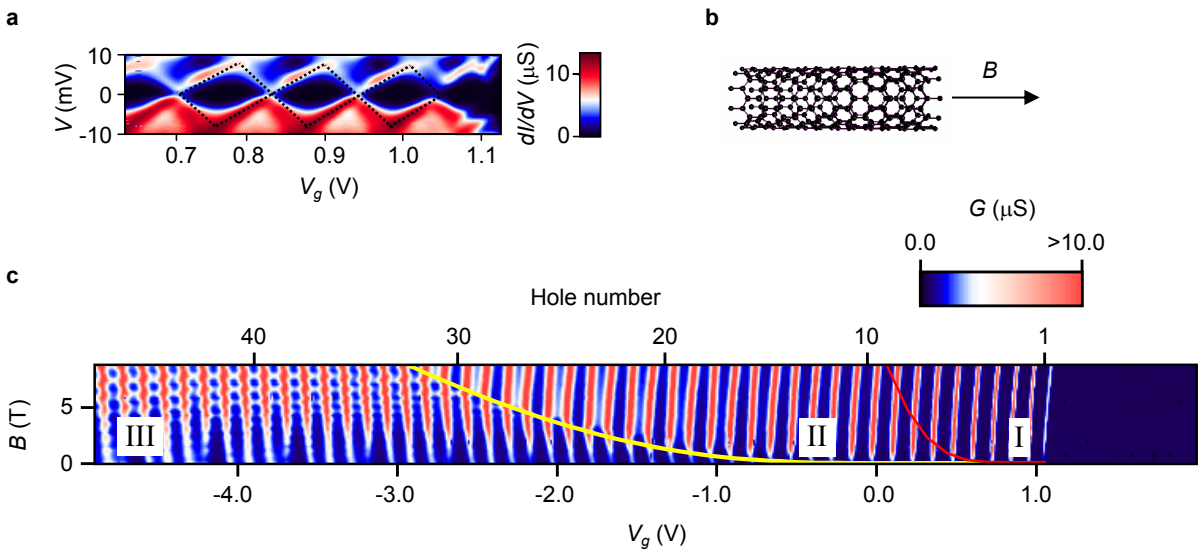

Figure 4.2. Transport spectroscopy and magnetic field evolution of Coulomb peaks. **(a)** Color plot of dI/dV versus gate voltage V_g and source-drain bias V. **(b)** Magnetic field B orientation relative to nanotube. **(c)** Color plot of G versus V_g and magnetic field B. The three different regions and curves, obtained from a model fit, delineating them are described in the text.

between two different positive values (region II). Finally, a region where both positive and negative slopes are observed in the vertical features, producing a zig-zag pattern, with similar magnitudes to the slope in region I. In addition, approximately horizontal features occur quasi-periodically in B (region III). The zig-zag pattern persists down to relatively weak fields, but is difficult to resolve below $B = 3$ T over the V_g range shown. Additionally, in region III, a four-fold period to the addition energies is observed, particularly at large carrier density (for example, Fig. 4.1(c) for V_g ∼-6 V, where the largest interval is typically ∼5% larger than the next smaller interval). The boundaries delineating these three regions are superimposed on the data as solid curves, which are calculated using a theoretical model as discussed below.

The spin and isospin states of each added hole can be inferred from the corresponding Coulomb peak slopes $dE/dB = (e/\alpha)dV_g/dB$. Figure 4.3(a) shows the measured slopes at $B = 8$ T in region I and II versus N. The peaks in region I are nearly parallel, with $d(E_Z + E_{orb})/dB \sim 0.4$ meV/T; in contrast, peaks in region II show a pronounced slope alternation, with an amplitude $\Delta E_s \sim 0.14$ meV/T. This indicates that in region I, all

the holes enter the dot with the same spin and isospin; in region II, the holes enter with alternating spins, but with the same isospin (see Fig. 4.3(a) insets). We thus find $\mu_{orb} \sim 0.33$ meV/T, yielding $r \sim 0.8$ nm. The electron g-factor is estimated from $\Delta E_s$to be ≈ 2.4, in good agreement with the theoretical value $\simeq 2$. Similar behavior has been found in all devices with a significant gap that showed regular Coulomb oscillations, attesting to the generality of this behavior in low-disorder samples. (Data from another device D2 is shown in the supplementary section in Fig. 4.5.)

The spin polarization observed in region I is surprising. In a shell-filling picture, the subbands corresponding to different isospin are split by the field [7, 29], and holes first begin to fill the lowest energy subband. This could account for the consistent isospin of the added holes. Yet, we expect because of the spin degenerate hole wavefunctions, they will tend to enter with alternating spins. Indeed, simple shell-filling models based on non-interacting electrons (such as a parabolic potential [28] or hardwall potential [7]) fail to reproduce the observed behavior (a detailed analysis is given in the Supplementary Discussion and Fig. 4.6), suggesting that strong interactions at low densities fundamentally alter the carriers' ground state.

This observed behavior, however, can be accounted for by assuming that the holes form a 1D Wigner crystal, in which the carriers become periodically ordered and interact via an exchange interaction J [20, 62, 68]. When $B > 0$ the state of the Wigner crystal is a competition between magnetic and exchange energy. At low n [62, 69], J is predicted to become exponentially small and the total energy will be minimized by having the holes with both spin and isospin polarized. At intermediate n, since $E_{orb} >> E_Z$, we expect a transition to an antiferromagnetically spin ordered, isospin polarized chain when $g\mu_B B = 2J$. For larger n, the carrier wavefunctions overlap strongly and we expect that exchange energy becomes large. We note that in nanotubes, carrier pairs have an exchange energy cost if and only if they have the same exact quantum numbers, including both spin and isospin; otherwise, a given carrier pair can both occupy their lowest energy molecular orbital state. This produces a four-fold addition energy pattern [47]. This picture thus qualitatively accounts for the existence and behavior of the three distinct regions as well as the transitions among them as n increases.

To analyze our data quantitatively, we utilize the theory of Levitov and Tsvelik [47]. The carriers in the 1D Wigner crystal within the nanotube are treated in terms of a linear

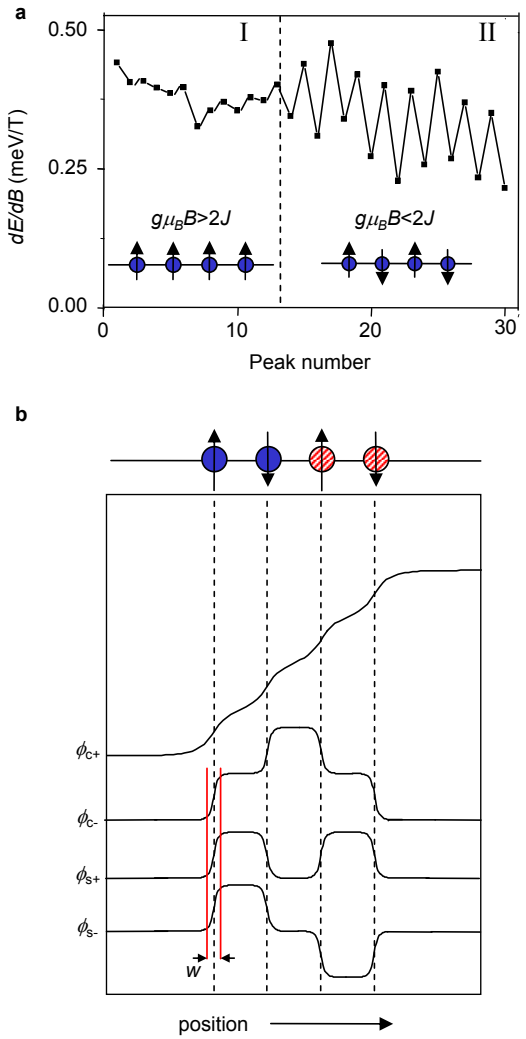

Figure 4.3. Energy shift of Coulomb peaks with B and schematic diagram of solitons corresponding to the four combination of spin and isospin. **(a)** Energy shift per tesla dE/dB of Coulomb peaks measured at B=8 T in region I and II. dE/dB is roughly constant in region I and shows alternation in region II. The value of the tube radius we find from analysis of this data is consistent with the range of radii typically reported for methane-based nanotube growth over the catalyst we employ [10], although knowledge of the tube radius is not essential to our analysis and interpretation. Inset: schematic diagrams of spin configurations in region I and region II. The holes all have isospin up. **(b)** Spatial variation of the four fields corresponding to charge sum in the two isospins (ϕ_{c+}), and three flavor modes corresponding to the charge difference (ϕ_{c-}), and spin sum (ϕ_{s+}) and difference (ϕ_{s-}). The corresponding hole configuration is shown at the top with the arrows indicating the spin and the color indicating the isospin, with blue indicating isospin up and red, hatched isospin down. The flavor soliton width w is indicated by the red lines.

combination of a charged bosonic field and three neutral flavor bosonic fields, chosen to yield their given spin and isospin. The fields' behavior is governed by a kinetic energy cost for localization that competes with a gap-dependent potential energy gain. This yields spatially-localized soliton solutions for the fields, with an optimal width w for the flavor solitons. Theoretical estimates yield a range of $w \sim 5 - 20$ nm for sample D1, and a charge soliton width approximately five times larger [47, 66]. Figure 4.3(b) shows the classical spatial variation of the four fields necessary to produce a chain with the four different spin and isospin combinations.

We use the theory of Levitov and Tsvelik in a classical approximation (details are provided in the Supplementary Discussion) to compute the ground state energy for a spin polarized (I), antiferromagnetically ordered (II), and four-fold period (III) ground state using the spin and isospin configurations shown in the insets to Figs. 3(a) and 3(b). As n increases, the flavor solitons overlap more strongly and J increases, leading to ground state transitions among the three states for $B > 0$. Note that our model assumes a uniform J; nevertheless, if the potential along the nanotube is non-uniform, as expected in our geometry [28, 70], the transition should occur with a similar energy per carrier as calculated by our method.

Using w as a fitting parameter, we fit the observed transition between regions II and III to the calculated B where the two states are degenerate. Fitting the data in Fig. 4.2(c) yields $w \sim 9$ nm. This fit is plotted in Fig. 4.2(c) as the yellow curve and follows the observed boundary closely. The fitted value falls well within the range of theoretically expected values. In the next step, using the fitted value for $w = 9$ nm, we directly compute the boundary between regimes I and II. The result is plotted in Fig. 4.2(c) as the grey curve, indicating the expected number of spin-polarized holes added at $B = 8$ T is ∼9, in agreement with the observed number ∼12. Although this boundary is not as distinct as that between II and III (attributed to the thermal smearing $\sim k_B T/g\mu_B \simeq 1$ T), the agreement is satisfactory given that the curve is plotted without free parameters.

Finally, we focus on the transition between regions II and III, which reveals a unique aspect of the strong electron correlations. Fig. 4.4(a) displays a color-scale plot of the conductance, G versus B and V_g. Regions II and III are divided by a black dotted line. In region II, G between adjacent Coulomb valleys alternates, with larger G in the odd-hole valleys, as shown in Fig. 4.4(b). This is a well-known signature of the Kondo effect [71], which

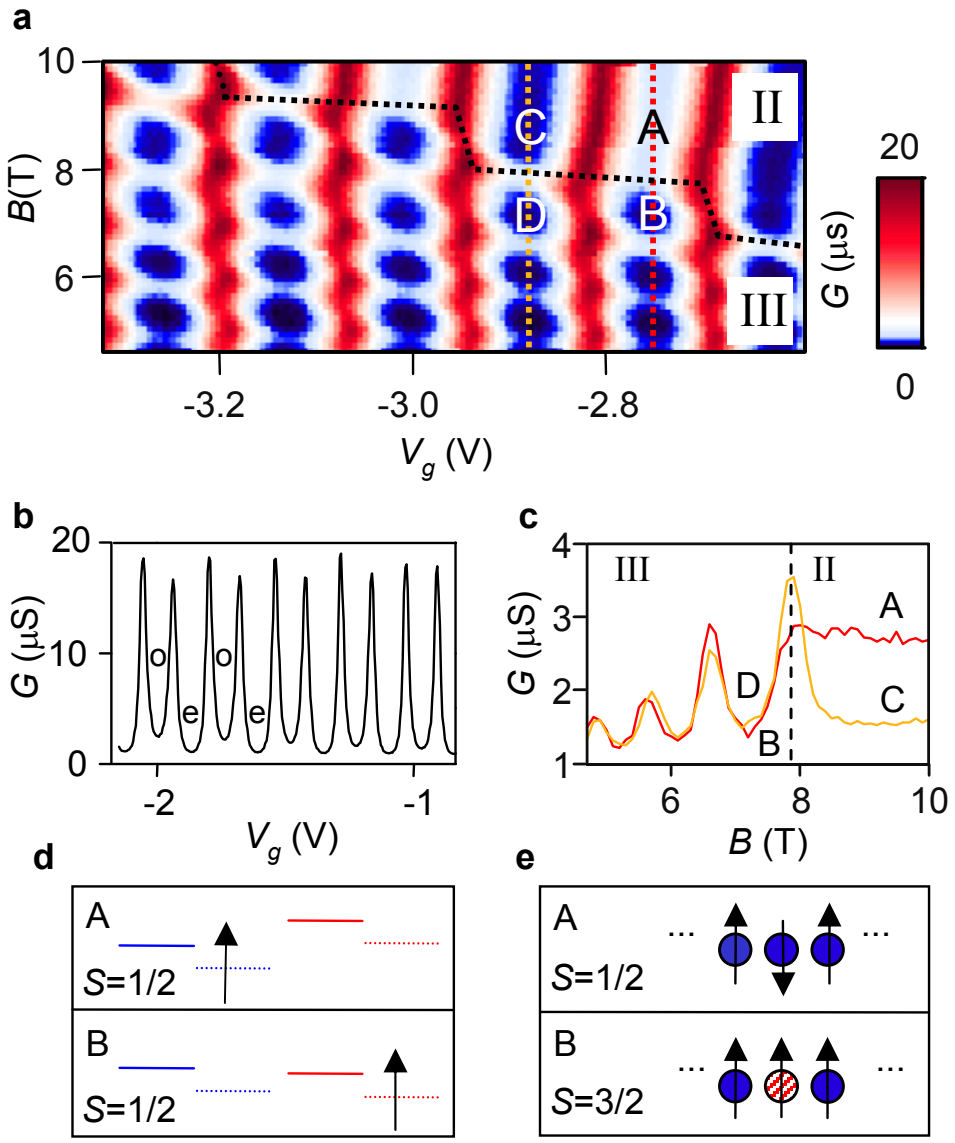

Figure 4.4. Kondo effect and flavor configurations. **(a)** Color scale plot of G versus V_g and B. The boundary between regions II and III is shown by the black dashed line. Points A and B are in an odd-hole valley, while points C and D are in an even-hole valley. **(b)** G versus V_g showing Coulomb peaks in region II taken at $B = 5$ T. **(c)** Line traces from part **a** taken along the odd-hole valley (shown in red) and in the even-hole valley (shown in dark yellow). **(d)** Shell filling picture of the transition between region II and III. Isospin up is shown by blue levels, while isospin down is shown by red levels. **(e)** Wigner crystal picture of the transition between region II and III.

results from the screening of a local spin on the nanotube with the conduction electrons in the electrodes to form a spin singlet state. This state has characteristic binding energy $\sim k_B T_K$, where T_K is the Kondo temperature [71], and k_B is Boltzmann's constant. The conductance alternation between valleys, and slopes of the Coulomb peak motion discussed previously indicates that the spin on the nanotube changes between $S = S_0$ in the even valleys and $S = S_0 + 1/2$ in the odd valleys, where S_0 is a constant [67].

To understand the appearance of the Kondo effect in our system, we note that in this regime of n, the spacing between flavor solitons ∼15–20 nm is comparable to their width ∼10 nm. As a result, J is large and the spin wave velocity approaches $\sim v_F$. For $k_B T_K$ lower than the quantum level spacing for spin wave excitations, $\approx hv_F/2L \sim 3$ meV, the Kondo effect will be sensitive to the total spin and isospin on the dot. This order of magnitude estimate is supported by theoretical calculations of the Kondo effect in quantum dot chains, which are conceptually similar to our system (see *e.g.* ref. [72]). We estimate from the measured parameters of our dot that $k_B T_K$ is ∼0.1 meV at the center of the Coulomb valleys [26] and thus we expect the total spin and isospin to be relevant.

An unexpected feature of the Kondo effect is the decrease in G by $\Delta G \sim 1.5$ μS in an odd-hole valley when B is tuned from region II to region III. In contrast, in the even-hole valley no such drop is observed (Fig. 4.4(a) points C and D). Fig. 4.4(c) shows G versus B taken along the red and yellow vertical dashed lines in adjacent Coulomb valleys. A shell-filling model could possibly account for the ridges by Kondo resonances enabled by level crossings [30]. However, this picture cannot readily account for the observed conductance drop ΔG since an odd hole state with total spin $S = S_0 + 1/2$ remains in the same spin state even when the up and down isospin bands first align at the Fermi level, as illustrated in Fig. 4.4(d). This picture therefore predicts $\Delta G = 0$, contradicting the observed dip.

However, according to the theoretical model discussed above, there are still strong correlations that can lead to different predicted spin ground states than a shell-filling picture. In particular, the transition between region II and III occurs via a succession of isospin flips, as indicated by the zig-zag pattern in region III. We attribute this to the previously mentioned non-uniform potential along the nanotube that produces a spatially inhomogeneous exchange interaction. When B is lowered from region II, the first localized isospin flip occurs in the region of maximum J. This will also be accompanied by a physical spin flip, which minimized the magnetic energy without an exchange energy cost. The total spin

state becomes $S = S_0 + 3/2$, as shown schematically in Fig. 4.4(e). Since T_K generally becomes lower as S increases [73], we expect G to drop between A and B, as observed. Thus the observation of $\Delta G > 0$ in the odd-hole valley provides a clear experimental signature of the strongly correlated nature of carriers in our experiment, that cannot be readily accounted for in a non-interacting electron picture. Note that while a classical description of the solitons can be used to explain our observations, further experimental and theoretical work is necessary to fully elucidate the behavior of the Kondo effect in our system. Nevertheless, taken together with the quantitative agreement of the transition boundaries to the theory of Levitov and Tsvelik, our data provides convincing evidence that carriers in carbon nanotubes at low densities form a 1D Wigner crystal.

The realization of this long predicted state can be used to test theories of interacting electrons in 1D in the clean limit [20, 61–63, 66]. For instance, at $B = 0$ the equilibrium state is determined by a competition between the thermal energy k_BT and J. If $k_BT >> J$, the spins and isospins can flip freely because of thermal fluctuations. This spin-incoherent regime is predicted to exhibit different behavior from an ordinary quantum wire, for example reduced conductance [20]. This may be observable in our system in future experiments provided we can achieve ballistic contacts to the nanotubes, for example by using Pd electrodes [74]. Moreover, we note that at low density, the experiment achieves a carrier separation of ∼100 nm which gives experimental access to control of individual exchange couplings, say using local gates. One could then utilize the many-body Wigner crystal as a chain of quantum bits towards realizing spin-based quantum computing in carbon, where intrinsic spin lifetimes are expected to be longer than in conventional semiconducting materials.

Supplementary Discussion

Calculation of exchange energy

The Levitov and Tsvelik theory [47] treats the carriers in a nanotube as a gapped Luttinger liquid (LL). The interactions in the gapped LL are characterized by a charge stiffness parameter K which is related to the inter-carrier interaction potential and can be usefully approximated by a constant $\sim 20 - 40$ [47, 66]. The interactions renormalize the non-interacting electron bandgap, making it $\sim K^{1/2}$ times larger.

In a nanotube LL, the two spin and two isospin states are described by one charged and three neutral flavor bosonic fields. When a spectral gap is introduced into the LL, the minimum energy field conguration becomes a lattice of sine-Gordon solitons, concentrating charge, spin, and isospin into localized packets to form the 1D Wigner crystal. The characteristic width w_c of the charge solitons is related to the measured gap Δ by $w_c \sim \hbar v_c/\Delta$ [75], where $v_c = K^{1/2} v_F$ is the charge mode velocity [47]. The flavor soliton width is $w \sim K^{-1/2} w_c$ [47, 66].

We compute the exchange energy in the Wigner crystal starting from the bosonized Lagrangian for the gapped Luttinger liquid with the four bosonic fields, which is the sum of two terms $V_0 + V_1$. The competition between V_0 and V_1 leads to soliton solutions for these fields. The solutions [47], together with the potential, enable us to compute the energy treating the fields classically.

The first term V_0 arises from the kinetic energy of localization [2, 47]

$$V_0 = \frac{\hbar v_F}{2\pi} \int dx \sum_{a=1}^{3} (\partial_x \phi_a)^2 \tag{4.1}$$

where $\phi_0 = \phi_{c+}$ is the charged field $\phi_{1,2,3} = \phi_{s+}, \phi_{s-}, \phi_{c-}$ are the three flavor fields, q is a wavevector, x is a position coordinate, v_F is the Fermi velocity, and $\hbar$ is Planck's constant. The second term V_1 is an effective potential that arises from the gap, given by [47]

$$\begin{aligned} V_1 = -4\lambda \int dx [&\cos(\phi_{c+}) \cos(\phi_{c-}) \cos(\phi_{s+}) \cos(\phi_{s+}) \\ &+ \sin(\phi_{c+}) \sin(\phi_{c-}) \sin(\phi_{s+}) \sin(\phi_{s+})], \end{aligned} \tag{4.2}$$

where $\lambda \simeq \hbar v_F/(4\pi w^2)$ is a (renormalized) coupling constant that is related to the physical flavor soliton width w.

A single soliton centered at the origin for the charge field is approximated by [47]

$$f_0(x) = \frac{\pi}{4} \left[e^{\frac{x}{\sqrt{K} w}} \theta(-x) + \left(2 - e^{-\frac{x}{\sqrt{K} w}} \right) \theta(x) \right], \tag{4.3}$$

where $\theta(x)$ is the unit step function. As a composite soliton of charge and flavor modes is the lowest energy state [47], the flavor fields then vary as

$$f_i(x) = \beta_i \frac{\pi}{4} \left[e^{\frac{x}{w}} \theta(-x) + \left(2 - e^{-\frac{x}{w}} \right) \theta(x) \right], \tag{4.4}$$

where $\bar{\beta}$=(1,1,1) for a spin up, isospin up carrier, $\bar{\beta}$=(1,-1,-1) for a spin up, isospin down carrier, $\bar{\beta}$=(-1,-1,1) for a spin down, isospin up carrier, and $\bar{\beta}$=(-1,1,-1) for a spin down, isospin down carrier. A soliton lattice corresponding to a chain of N carriers with density n is given by

$$\phi_0(x) = \sum_{j=1}^{N} f_0(x - j/n) \tag{4.5}$$

$$\phi_i(x) = \sum_{j=1}^{N} \beta_{ij} f_i(x - j/n), \tag{4.6}$$

where β_{ij} are the numbers β_i for the jth carrier. The energy is computed by substituting the expressions for $\phi_0(x)$ and $\phi_i(x)$ into the the potential $V_0 + V_1$ and computing the energy numerically. The magnetic energy is computed by multiplying the net spin by $g\mu_B B/2$ and the net isospin by $\mu_{orb} B$. The sum of the exchange and magnetic energy for a spin and isospin polarized electron or hole lattice, a spin-alternating, isospin polarized lattice, and a four-fold period lattice is used to determine which of these three states is the ground state. The result for the boundary between the four-fold and spin-alternating region is then converted into a mathematical interpolation function to fit to the data.

We note that this model is expected to be valid as long as the soliton width significantly exceeds the tube diameter [47], as it is expected to theoretically, and as it does in our fitted results.

Magnetic field and gate-voltage dependence from different devices

Figure 4.5(a) shows the differential conductance versus V_g and B for sample D1 taken to larger negative gate voltages than shown in the main text. Figure 4.5(b) shows similar data from another sample D2, also taken at 1.4 K. Note that the soliton spacing becomes smaller than the characteristic soliton size which occurs at $\sim L/w \sim 50$ holes for devices D1 and D2. In this regime, the solitons should merge together. This corresponds to a nearly constant charge and flavor density. In this limit, we expect that the device will therefore cross over to a metallic hole-liquid like regime, where the behavior can be described by a conventional shell-filling picture [24, 25], consistent with the well-defined four-fold periodicity of the Coulomb peaks we observe in this regime.

Addition energies; analysis of hardwall and parabolic potential models

Figure 4.6(a) shows the addition energies for sample D1 for different magnetic fields (offset for clarity). The data was obtained at each magnetic field value from the measured peak spacings and the value for α given in the text. Arrows mark the approximate beginning and end of region II for each magnetic field value. We note that the addition energies arise from the total energy to add each hole, including the Coulomb energy. In contrast the slope of the Coulomb peaks' evolution depends only the coupling of each hole's energy to the magnetic field. Therefore, determining the quantum number of the added carriers from the Coulomb peak evolution as we have done in the main text is more straightforward than using the addition energies.

Figure 4.6(b) shows a plot of the calculated level spectrum from a hard-wall model (HWM), for the length and measured μ_{orb} for D1. In addition to the coupling to the magnetic field from the electrons orbital motion [7], we also include the Zeeman energy from the electron spin. The levels are then derived from the equation

$$E_{n,\sigma,\delta} = \hbar v_F \sqrt{(\frac{\Delta}{\hbar v_F} + \delta\frac{reB}{2\hbar})^2 + (\pi n/L)^2} + \sigma\frac{g\mu_B B}{2}, \tag{4.7}$$

where the signs are determined by the spin ($\sigma = -1, 1$) and isospin ($\delta = -1, 1$) corresponding to each level, n is an integer $\geq$1, and other variables are as given in the text.

In the simplest picture, these single-particle levels with lowest level spacings $\sim$150, 250, 350... μeV would be filled with electrons up to the Fermi level. Up to $B = 9$ T, 4 holes are in region I, significantly less than the $\sim$12 spin-polarized carriers we observe. In addition, if we assume a constant charging energy U, The HWM predicts kinks in the Coulomb peaks evolution because of the numerous level crossings, which also we do not observe. In our calculation, we have assumed subband degeneracy, yielding a four-electron period for $B = 0$, although relaxing this assumption produces no qualitative differences in the results.

We also consider a parabolic potential model, as done in the electron hole symmetry work by Jarillo-Herrero et al. [28] However, this yields a mean level spacing $\sim$1.5 meV, and thus this model predicts the absence of region I over the entire range of magnetic fields studied, and predicts only $\sim$5 holes would be added before reaching region III, far fewer than we observe. This makes a shell-filling model even more difficult to accept as an explanation for our data, since an approximately parabolic potential is most likely appropriate at the

low densities we obtain in region I and II [28].

Finally, note that the results from region I differ from those of Tans et al. [76], in which repeated addition of the same spin electron to a metallic nanotube was observed over a limited range of gate voltage for $B <\sim 1$ T, followed by a complex spin-filling pattern at larger B. Here, the spin polarization is observed reproducibly in gapped nanotubes in the low density regime, and persists over the entire measured range of B up to 10 T.

The importance of non-nearest neighbor exchange coupling in producing a four-fold addition energy period

In a nearest neighbor exchange picture, an exchange energy cost only exists when pairs of adjacent carriers in the chain have the same exact quantum numbers, considering both spin and isospin. This symmetry between spin and isospin follows from both the molecular orbital picture of exchange discussed in the text, as well as the Lagrangian discussed by Levitov and Tsvelik. In a magnetic field, since an isospin down has a larger magnetic energy cost than physical spin down, a state where each carrier is isospin up minimizes the magnetic energy. However, a spin antiferromagnetic state minimizes exchange energy since each nearest-neighbor pair has different quantum numbers. The ground state, which minimizes both nearest neighbor exchange and magnetic energy is therefore spin antiferromagnetically ordered, with each carrier isospin up. This would preclude four-fold filling, unless the exchange interaction between non-nearest neighbor pairs is considered.

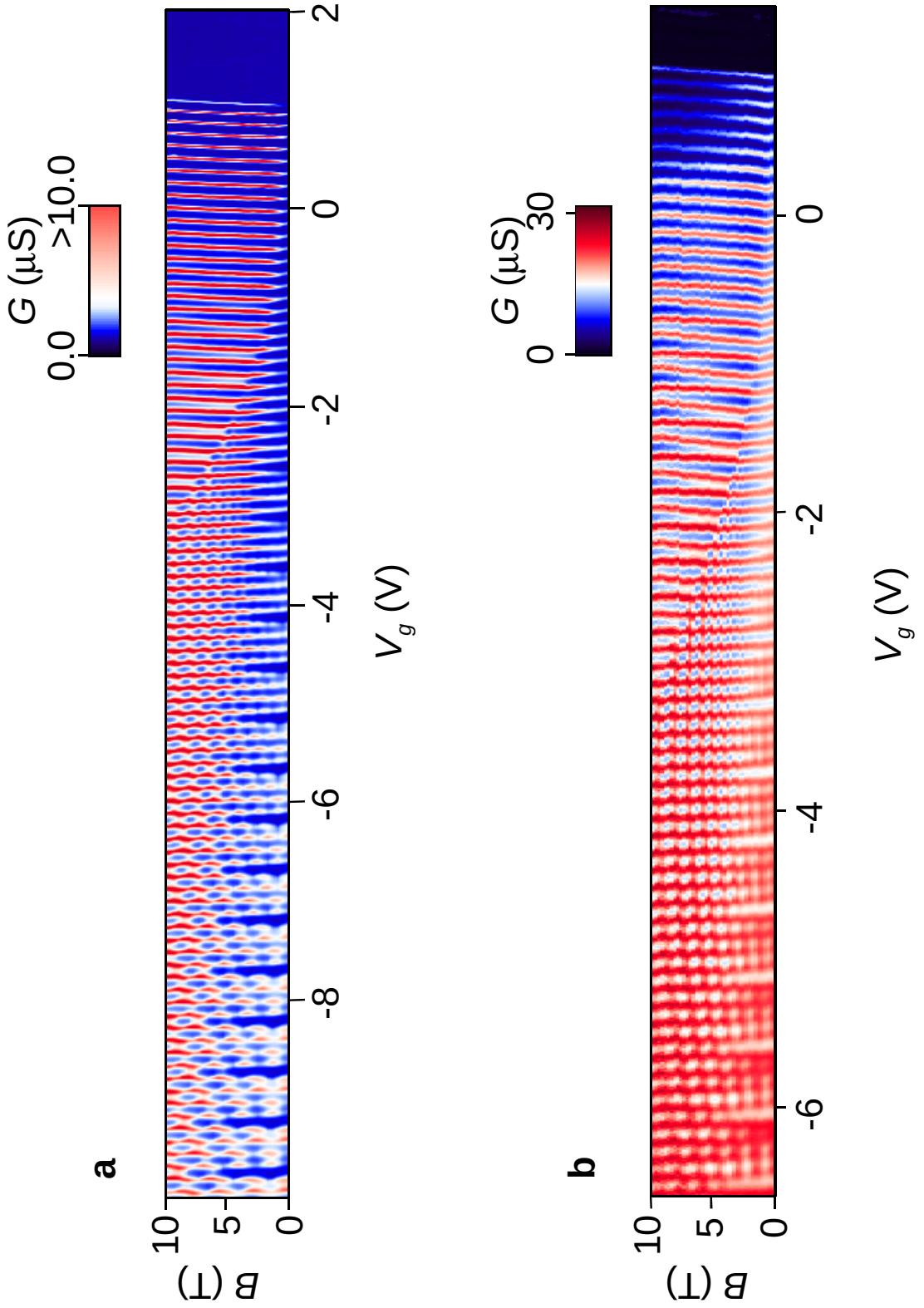

Figure 4.5. Color scale plot of dI/dV versus magnetic field for sample D1 **(a)** and D2 **(b)**

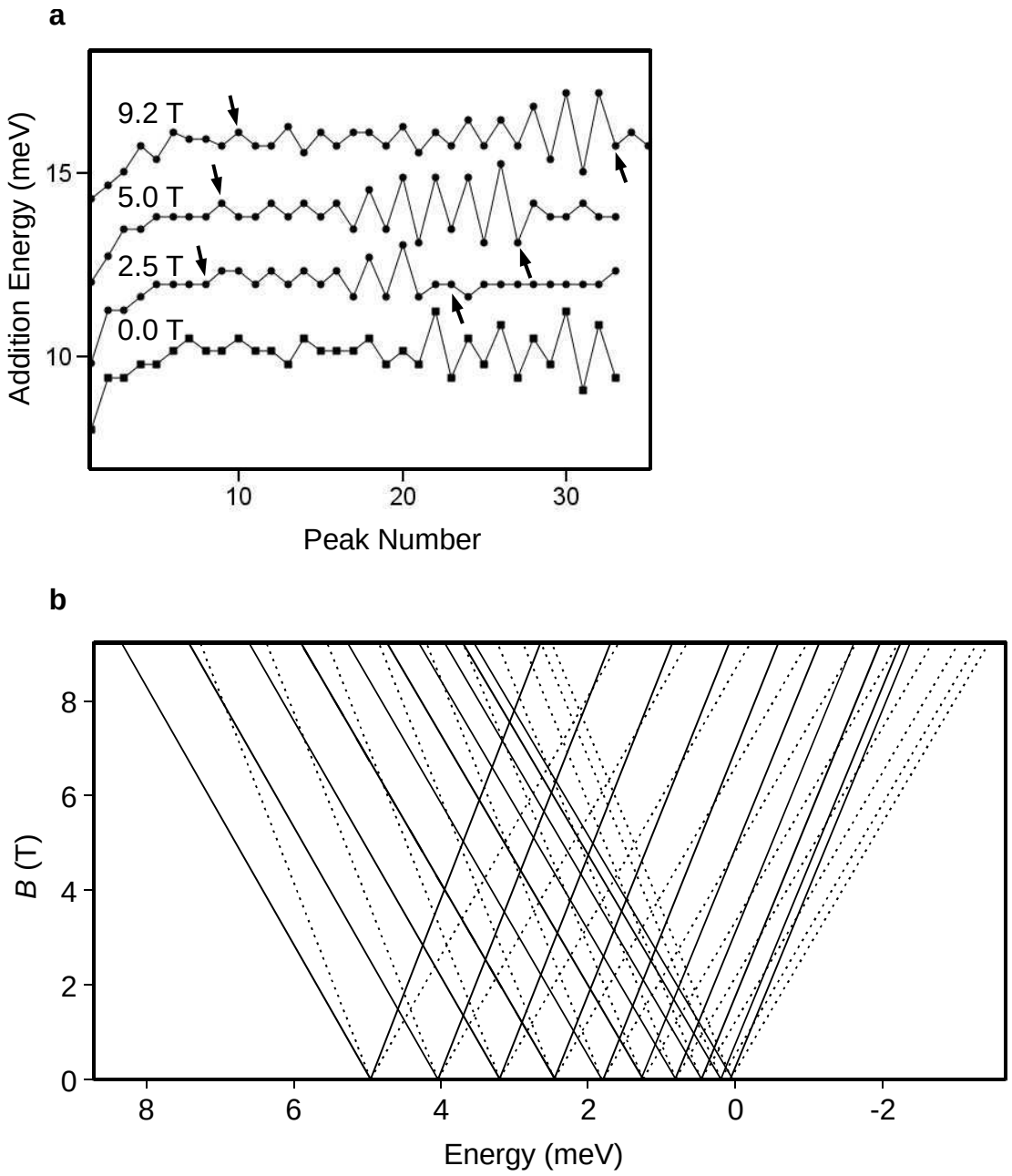

Figure 4.6. **(a)** Addition energies for sample D1 at various magnetic fields. Curves are offset for clarity. **(b)** Hardwall model quantum level energies versus magnetic field as explained in supplemental discussion. Solid lines correspond to spin down states and dotted lines to spin up states.

Chapter 5

Observation of a Mott Insulating State in Carbon Nanotubes

Abstract

The Mott insulating state is a dramatic manifestation of strong electron interactions in nominally metallic systems. Using transport spectroscopy, we show that an energy gap exists in nominally metallic carbon nanotubes, and occurs in addition to the band-gap in small-band-gap nanotubes, implying that carbon nanotubes are never metallic. This gap shows universal behavior, with magnitude 10–100 meV and nanotube radius dependence $\sim 1/r$, in good agreement with predictions for a nanotube Mott insulating state. We also observe neutral excitations within the gap, as predicted for this state. Our observation enables a gate-tunable one-dimensional Mott system, and comprises a realization of a nanoscale Mott transistor.

According to the quantum theory of solids, materials can be either metals or band insulators. However, this theory breaks down in metals at half filling of energy bands when strong Coulomb repulsion makes it energetically favorable for electrons to localize, one electron per atomic site, to form a Mott insulator [77]. This state is known to be anti-ferromagnetically ordered in higher dimensions and has been observed in a variety of bulk materials, including thin-films [78] and nanobeams [79]. The one-dimensional (1D) analog of this state is, however, remarkably different. Known as a spin-liquid Mott insulator, it has only short-ranged magnetic order and may have gapped spin excitations [54]. The presence of a spin gap in some classes of spin-liquids is believed to be related to the emergence of high-temperature superconductivity in cuprate oxides [80], motivating a search for such systems. Theoretical work [50, 51, 53, 55, 56] predicts that carbon nanotubes are a realization of a gapped

spin-liquid Mott insulator.

Experiments on bulk quasi-1D Mott insulating systems [54] typically use chemical doping which introduces additional disorder. Carbon nanotubes offer the unique opportunity of studying electronic phenomena without interference from disorder by using electric-field doping. Recently, the fabrication of ultra-clean nanotube devices [7] has facilitated the observation of long-predicted phenomena such as Wigner crystallization [81] and spin-orbit coupling [82], and may produce favorable conditions for observing a tunable 1D Mott insulator in an individual nanostructure.

Here we show that carbon nanotube transistor devices exhibit energy gaps that cannot be accounted for using non-interacting electron pictures, but agree well with predictions for a spin-liquid Mott insulating state in carbon nanotubes. These finite-size samples act as quantum dots, and Coulomb peaks corresponding to a single electron/hole at the band edge are observable. We tune the magnitude of the energy gap by applying an axial magnetic field [29]. By tracking the first electron and hole addition energies using transport spectroscopy, we accurately estimate the magnitude of the gap as it is tuned. Our data show that, in contrast to the expectation of non-interacting electron models, in which gaps are produced by the displacement of the Dirac points in the Brillouin zone of graphene by symmetry-breaking mechanisms such as strains, twists, or curvature [13, 83], this gap cannot be tuned to zero with an applied magnetic field. The gap instead reaches a minimum value at a critical magnetic field. Moreover, we measure the dependence of the minimum gap on the nanotube radius r and find a characteristic approximate $1/r$ dependence. Both the magnitude and behavior of the minimum gap with radius are consistent with theoretical predictions for the behavior of a Mott gap in a nanotube [50, 51, 53, 55, 56]. By measuring the critical magnetic field to minimize the gap, we determine the single-particle band-gap for each nanotube as well, finding values within the theoretically expected range from a curvature-induced mechanism. Finally, we also observe neutral low-energy excitations in the gap by inelastic cotunneling, which have a strong dependence on magnetic field. We interpret these as the neutral excitations of the spin-liquid Mott insulating state. Crucially, we note that such low-energy excitations do not exist in a non-interacting electron picture, where the single-particle gap sets the minimum excitation energy.

Previous work has shown the presence of energy gaps in carbon nanotubes. Indeed, depending on their radius and chirality, 2/3 of nanotubes are expected to be semiconducting

due to the boundary conditions causing the allowed wave-vectors in the Brillouin zone to miss the gapless Dirac points. For the remaining 1/3 of tubes which are expected to be metallic in a zone-folding picture, the non-interacting-electron symmetry-breaking mechanisms mentioned above can open a band gap [83]. Scanning tunneling microscopy studies of nanotubes have attributed energy gaps to curvature [84]; however these studies were performed on metal substrates, which screen electron-electron interactions. Previous transport experiments on nanotubes, where interactions are not screened, have shown gaps in the range ∼10–100 meV [85], but their origin was not investigated. To assess the role of curvature in producing the observed gaps in transport studies, we first studied armchair nanotubes, which are predicted to be metallic by band structure calculations and protected by symmetry from having curvature-induced gaps [83].

Figure 5.1(a)(right) shows the conductance G versus gate voltage V_g for two 500 nm segments each on two armchair nanotubes, fabricated and characterized by Rayleigh scattering measurements (Fig. 5.1(a)(left)) according to ref. [86]. All segments show a dip characteristic of an energy gap [85]. Similar behavior has been observed in ∼90 devices fabricated on 5 separate armchair nanotubes. Thus curvature can not fully account for the observed gaps in transport experiments. Nevertheless, gaps of similar magnitude or larger in tubes could also occur *e.g.* because of twists or strains produced during the device fabrication [29], making the origin of the observed gaps in transport studies still unclear.

To address the origin of energy gaps in "metallic" nanotubes, we fabricate extremely clean, as-grown, suspended devices free from disorder due to chemical processing or the substrate. These samples, discussed exclusively in the remainder of this chapter, are fabricated by chemical vapor deposition (CVD) growth over Pt electrodes as reported in detail previously [7, 81], and are presumed to have random chirality. The growth substrate is a Si_3N_4 layer on Si that has a trench between the two electrodes that enables the nanotubes to be freely suspended. Additionally in this work, varying ratios of Fe/Mo catalyst salts are used to vary the average nanotube radii [42]. Figure 5.1(b) shows a scanning electron microscope image of a representative device, with a measurement geometry similar to that employed earlier [81]. After growth, individual single-walled nanotube devices are selected based on their room-temperature transport characteristics [81].

Figure 5.1(c) shows the conductance G versus back gate voltage V_g for a representative device D1 (length ∼100 nm) at several different temperatures. The device shows a dip

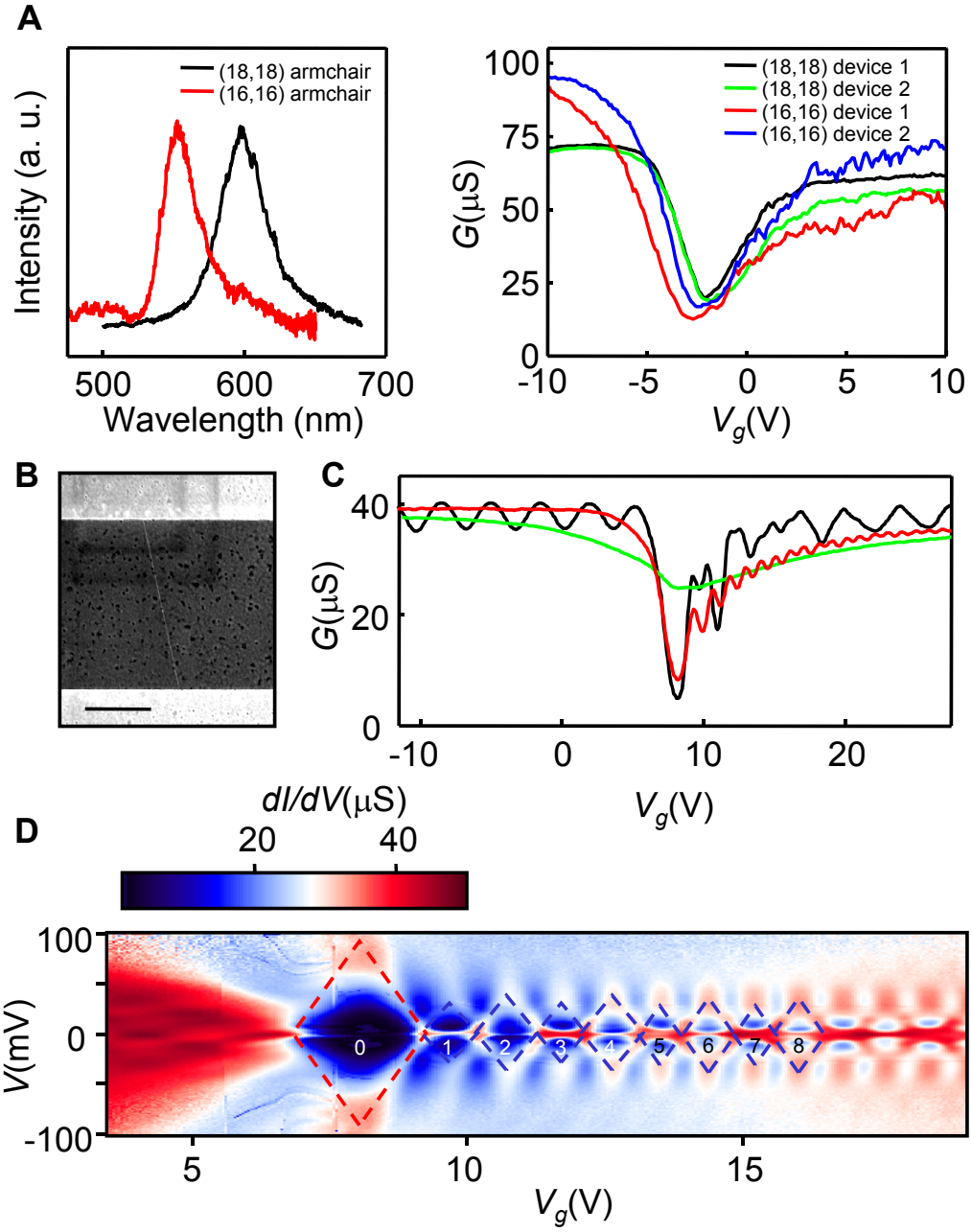

Figure 5.1. **(a)** Rayleigh scattering spectra (left) and room-temperature transport characteristics (right) of two armchair nanotubes. **(b)** Scanning electron microscope image of a representative suspended nanotube device. The scale bar indicates 2 μm. **(c)** Conductance versus gate voltage for D1 at temperatures T=1.5 K (black), 150 K (red) and 300 K (green). **(d)** Color plot of dI/dV versus gate voltage V_g and source-drain bias V for D1. The numbers indicate the number of charge carriers in the blockaded state.

similar to that in Figure 5.1(a). As the temperature is lowered the minimum conductance tends towards zero. Figure 5.1(d) shows a plot of G in color scale versus V_g and bias voltage V for D1 at 1.5 K. The gap corresponds to the large diamond marked with the red dotted lines. For the electrons, smaller diamonds marked by the blue dotted lines indicate Coulomb blockade with a charging energy $U \sim 40$ meV. On the hole side the conductance is somewhat larger and the features are reminiscent of the Fabry-Perot interference behavior observed previously in strongly coupled nanotube quantum dots [27]. These regular features are indicative of extremely clean quantum dots. Energy gaps were observed in all clean samples studied.

The magnitude of the gaps in single-walled nanotubes can be modulated with an axial magnetic field [29]. Figure 5.2(a) shows a plot of conductance G versus V_g and axial magnetic field B for device D2 with length 200 nm at 1.5 K. As with D1, the hole side is more conductive than the electron side and the two are separated by an energy gap. On application of the field, the lowest quantum energy levels (namely, the first electron and hole state) do not undergo crossings and can be used to accurately determine the gap. At low fields, the Coulomb peaks for the electrons evolve with a slope $dE/dB = \alpha dV_g/dB = 0.79$ meV/T, and with a similar magnitude, but opposite sign for the holes. The gap therefore decreases as the magnetic field is increased from $B = 0$. However, at a critical magnetic field $B_c \sim 4$ T, the gap stops closing and begins to open again. At this field we also often see an approximately horizontal conductance ridge extending across the gap in the G versus B and V_g plot.

This gap includes contributions from the charging energy U arising from electrostatic energy as well as a term ΔE from contributions due to the discrete energy levels of the electron system. Both these contributions arise from the finite size of the nanotube and would vanish in an infinite tube. To find the magnitude of the intrinsic gap that would occur for a very long nanotube, the contributions from U and ΔE must be subtracted. We therefore subtract the measured energy (≈ 12 meV for D2) obtained from Coulomb blockade diamonds from the measured energy of the gap. The inset to Fig. 5.3(b) shows the corrected gap versus B. Remarkably, this gap does not reach zero when $B = B_c$, but instead reaches a minimum value of $\Delta_{min} \approx 37$ meV. One can directly reduce finite-size effects by studying longer devices. Indeed, as shown in Figures 5.2(b) and 5.2(c) for devices D3 and D4 of lengths 500 nm and 2 μm respectively, the minimum gap dominates the

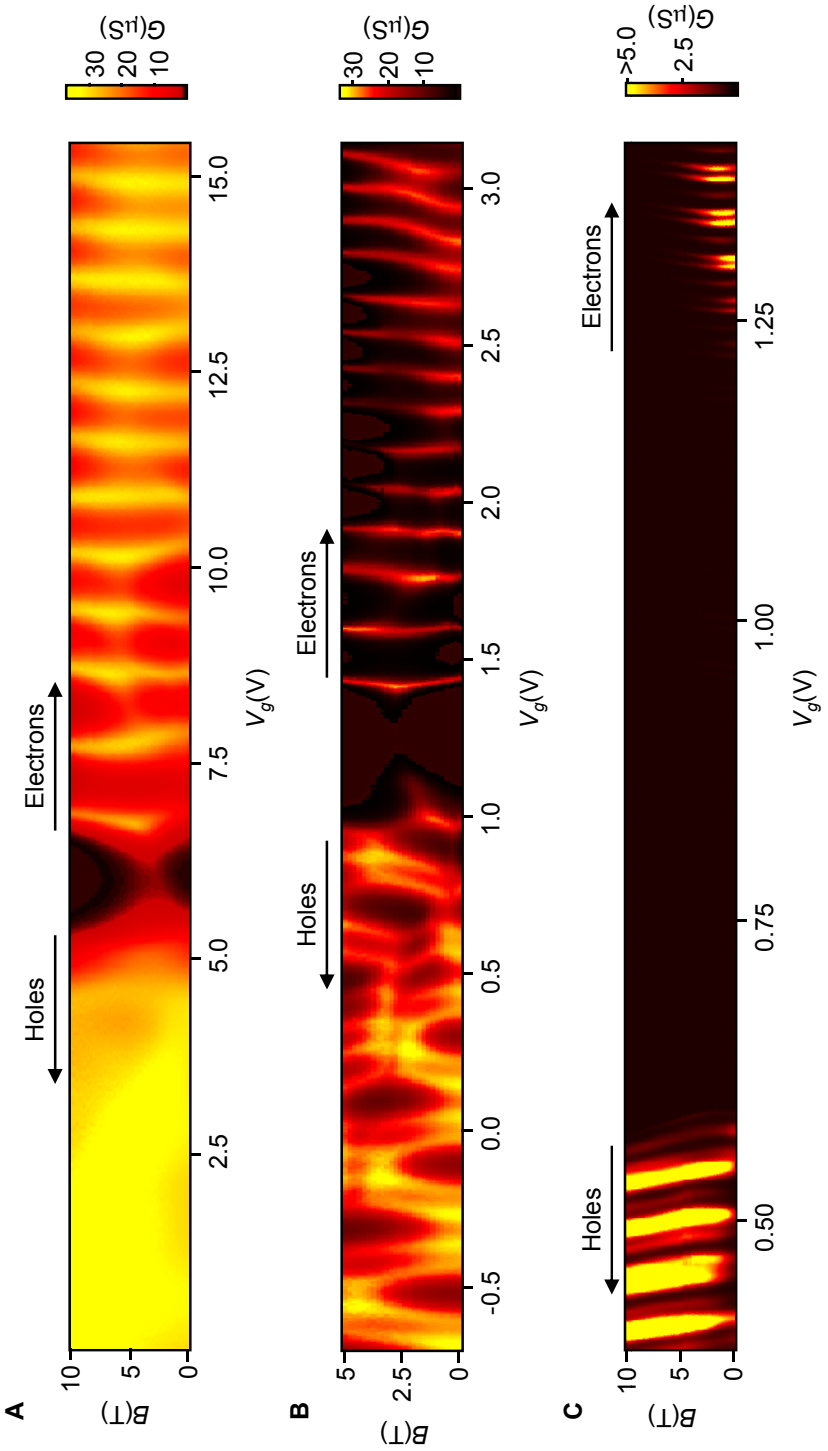

Figure 5.2. Color plot of conductance G versus V_g and magnetic field B for three devices: **(a)** D2, $L \sim 200$ nm **(b)** D3, $L \sim 500$ nm **(c)** D4, $L \sim 2$ μm. The electron and hole states are indicated for each device. Note that the first electron/hole energy level does not undergo crossings and can be used to study the gap. The evolution of higher charge states has been studied using quantum dot spectroscopy [82, 87]. Note also that, in part **c**, the first few electrons are not visible in the linear conductance plot. However their position is known from non-linear transport experiments.

charging energy and confirms the generality of the observed behavior.

Such a gap could possibly result from curvature in non-armchair tubes, or perturbations such as built-in strain or twists from the nanotube growth process. In a non-interacting electron picture [83], these perturbations cause the quantized transverse electron wave-vector to miss the zero-gap Dirac point of graphene's band-structure. This opens a gap in the nanotube band-structure [83]. The axial magnetic field shifts the transverse wave-vector [29], sweeping the quantization through the Dirac point for large enough field. However, the gap would be zero at the minimum rather than the finite value we observe. This contradiction with experiment, along with the observed energy gap in armchair nanotubes, rules out curvature, strain or twist as a possible mechanism for Δ_{min}.

To gain further insight into the origin of this gap, we have investigated how Δ_{min} depends on the nanotube radius r. The radius was obtained by measuring the slope of the Coulomb peak evolution in the magnetic field, and using the gate-efficiency factor α obtained from non-linear transport measurements on each device to determine $dE/dB = \alpha dV_g/dB$. This can be related to the radius via the orbital magnetic moment μ_{orb} using the relation $dE/dB = \mu_{orb} \pm \mu_Z = \pm rev_F/2 \pm \mu_Z$, where μ_Z is the electron spin magnetic moment. This procedure has been used by a number of groups to estimate nanotube radii [7, 29, 81, 82, 87]. A plot of Δ_{min} versus r for fifteen devices is shown in Fig. 5.3(a). The data follow an approximate $1/r$ relation. The inset to Fig. 5.3(a) shows the value of the additional gap that occurs at $B = 0$ as compared to when $B = B_c$, taken to be the single-particle band gap Δ_{sp}. Unlike the minimum gap plotted in the main panel, Δ_{sp} shows no trend with radius. However, it falls within the theoretical prediction for a curvature induced gap (shaded region) [83], which is given by $\approx 20\cos(3\theta)/(r[\mathsf{nm}])^2$ meV, with $0 < \theta < 30^\circ$ the range of nanotube chiral angles [84].

Another possibility for Δ_{min} is the Peierls instability, which opens an energy gap in 1D systems. However, due to stiff carbon-carbon bonds, such a gap for nanotubes is expected to be $\sim$1 meV for a 1 nm diameter nanotube [83], and recent calculations give $\Delta_{peierls} = 0.26/r^3$ meV where r is in nm [88]. Theoretical calculations thus are two orders of magnitude smaller that the observed gap and and have a different r dependence for Δ_{min} than we observe.

Having ruled out these non-interacting electron pictures, we now consider the influence of electron-electron interactions. In the simplest picture, electron-electron interactions are

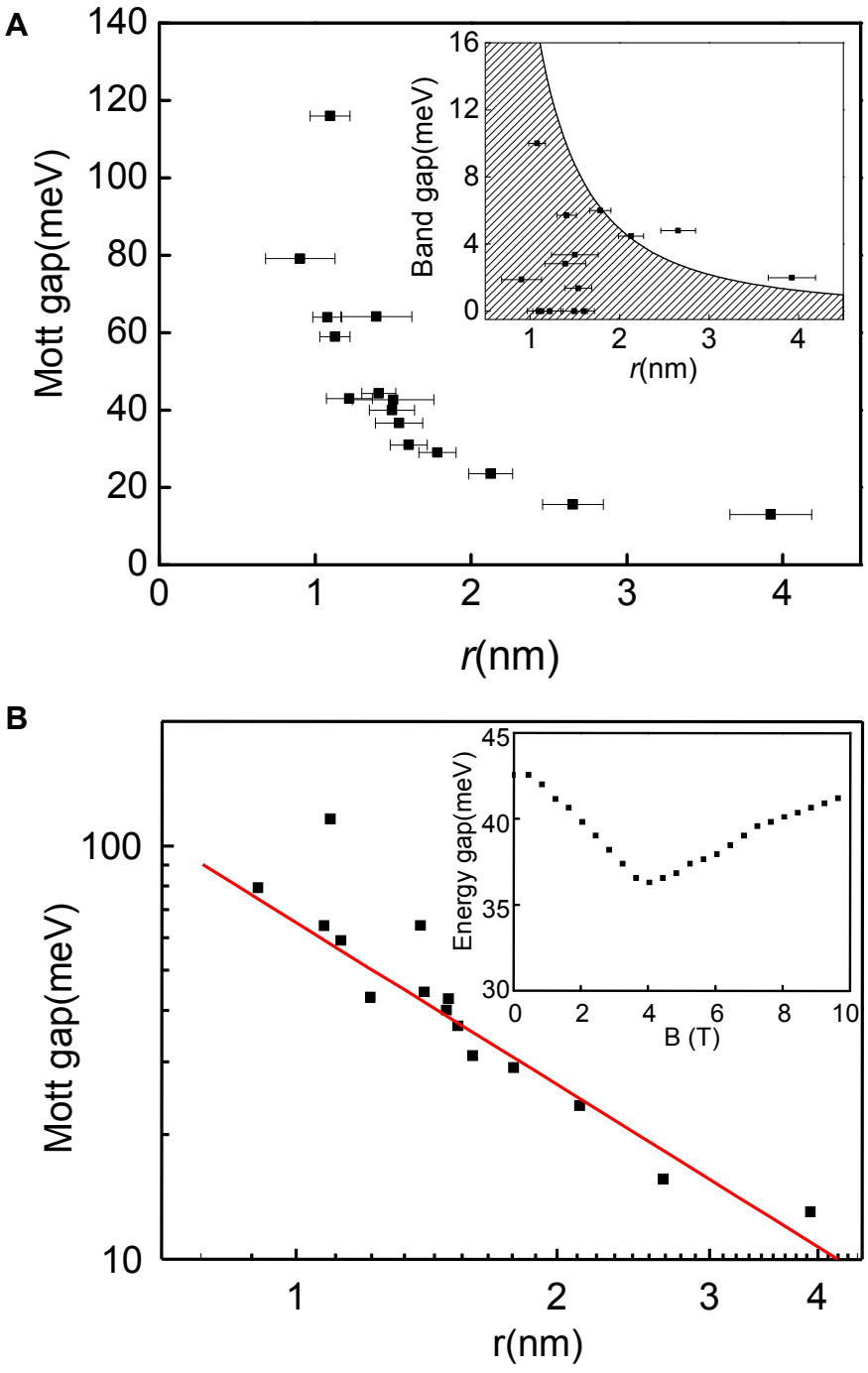

Figure 5.3. **(a)** Variation of the gap Δ_{min} with nanotube radius for 15 devices. The largest contribution to error bars comes from pixel size in Figure 5.2 and uncertainty of nanotube alignment with magnetic field (±20 degrees). (Inset) Plot of the single-particle band-gap Δ_{sp} versus nanotube radius. The shaded region corresponds to the prediction for curvature-induced gaps [83] depending on chirality. **(b)** Log-log plot of Δ_{min} with nanotube radius. (Inset) Variation of energy gap with magnetic field for D2.

considered in the forward-scattering approximation, producing a Tomonaga-Luttinger liquid state governed by the long-range part of the Coulomb interaction, which retains the metallic behavior [83]. However, at half-filling of energy bands, umklapp scattering via short-ranged Coulomb interactions is a viable backward-scattering mechanism. These interactions arise from the confinement of the electron wavefunctions due to the nanotubes' wrapped geometry.

Upon considering umklapp scattering, theory [50, 51, 53, 55, 56] predicts the formation of a Mott energy gap in metallic nanotubes at half-filling, rendering the metallic state into a Mott insulator. As discussed in refs. [50] and [51], one can establish equivalence between a nanotube and a two-chain version of the 1D Hubbard model (a two-leg ladder). The equivalent on-site interaction in this model is the average over atoms along the circumference of the nanotube, which gives a universal $1/r$ scaling to the energy gap in all nominally metallic tubes [53]. The renormalization-group calculation [53] suggests that the long-range part of the Coulomb interaction modifies the Mott gap scaling with radius to $r^{-1/(1-g)}$, where g is the Luttinger parameter, taken to be $\sim$ 0.2-0.3 for nanotubes [83].

In Fig. 5.3(b), the measured Δ_{min} is plotted against r on a log-log scale. The data falls on a straight line with a slope $\sim$-1.3$\pm$0.15, which yields an estimate for $g \sim 0.13 - 0.3$, in agreement with the expected range of values. The slope reveals that the data follow the curve $\Delta = \beta r^{-1.3}$, with $\beta = 60$ meV$\cdot$nm$^{-1.3}$ This value for β is in agreement to the theoretically estimated range of 10–100 meV$\cdot$nm$^{-1.3}$ [53].

We now turn to neutral excitations which are observed within the Mott gap. Figure 5.4(a) shows a plot of dI/dV versus V_g and V for a device D5 of length 200 nm. The gap region is indicated by the dashed lines. A number of features approximately independent of gate voltage appear in the gap. These features arise from inelastic cotunneling [89], in which a tunneling electron leaves behind a neutral excitation on the nanotube. The bias at which they occur directly yields the energies eV of these excitations. Figure 5.4(b) shows a plot of dI/dV versus V and B for V_g in the middle of the gap. B_c for this device is indicated by the vertical dashed green line. Near B_c the features corresponding to the lowest energy excitations acquire a slope with an energy shift of $\mu_{ex} \sim 2$ meV/T, indicating that they are of electronic origin rather than from, for example, phonons. Similar features were observed for all strongly-coupled devices where data was taken.

Neutral massive (gapped) excitations of the Mott insulator in a metallic nanotube are

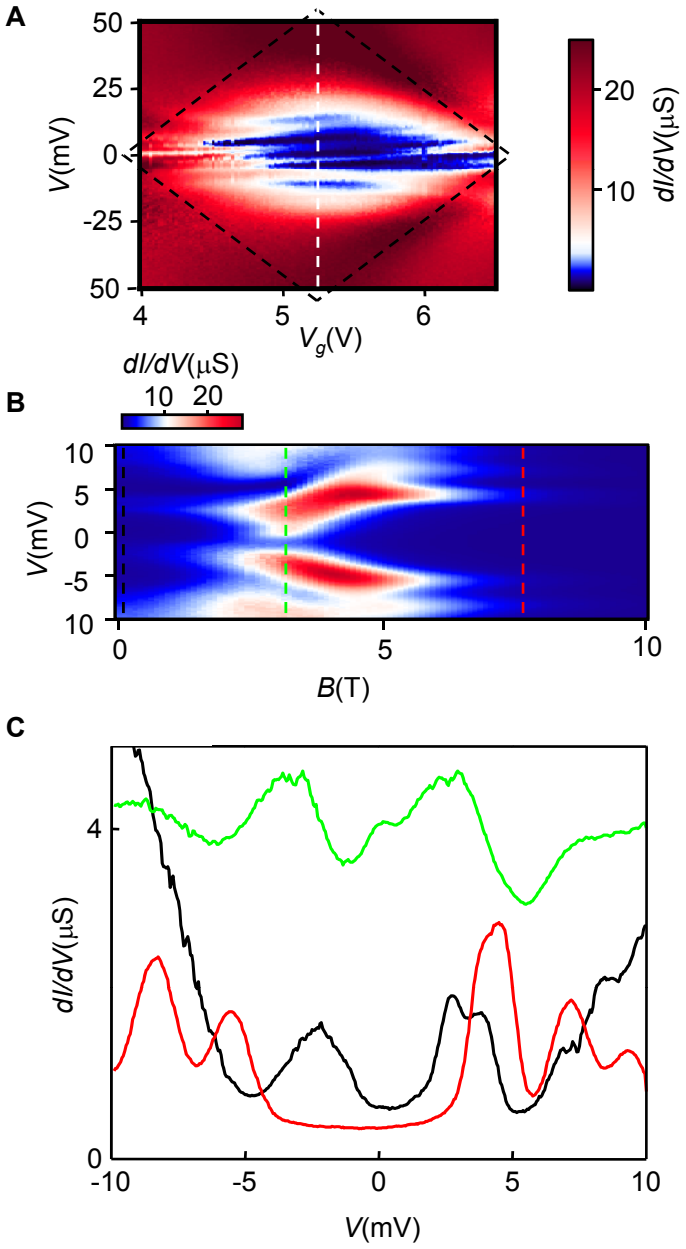

Figure 5.4. **(a)** Color plot of dI/dV versus gate voltage V_g and source-drain bias V for D5. The diamond indicated by black dashed lines corresponds to the energy gap. **(b)** Color plot of dI/dV versus magnetic field B and source-drain bias V in the middle of the gap (V_g corresponding to the white dashed line in part **a**). The yellow dashed line corresponds to B_c, where the energy gap is minimum. **(c)** dI/dV versus V at three different magnetic fields in part **b** corresponding to the black, green, and red dashed lines. Note the green curve has been scaled down by a factor of 10 and offset for clarity. Note also that the green curve shows a Kondo-like peak at zero bias that could account for the ridges observed for example in Fig. 5.2**a** and **b** at $B = B_c$.

characterized by several quantum numbers such as spin and vorticity [53, 56]. Symmetry-breaking mechanisms can also give rise to charge and neutral gaps as shown in ref. [47]. Neutral gaps in both pictures are separated in energy from the charge gap by the Luttinger parameter g. While the interplay between these two mechanisms for a realistic metallic tube has not been considered theoretically, it is likely that the gapped neutral excitations will generally persist even in the presence of a single-particle gap. This is consistent with our observations (Figure 5.4), as the neutral excitations remain gapped for any magnetic field. The lowest energy neutral gap, is predicted to be a fraction 0.26 of the Mott gap, for D5 [53]. We observe the ratio to be $\sim$0.2 in good agreement with theory. This measured separation of scales between the neutral and Mott gaps is also consistent with the value g of the Luttinger parameter for nanotubes.

At the critical field B_c, the symmetry-breaking single-particle gap $\Delta_{\rm sp}$ is likely to be compensated by the field. This regime may still be more complex than that considered in ref. [56], since the gap vanishes for only one of the two Dirac points. Furthermore, away from $B = B_c$, it is likely that the gap in the neutral sector will increase mostly due to single-particle terms of the kind considered in ref. [47] which scale as $erv_F(B - B_c)$, consistent in magnitude with the observed μ_{ex}. Our observation of a universal gap along with two independent measures of the Luttinger parameter thus provides convincing evidence for the 1D Mott state in nanotubes. Future theoretical work will address the behavior of excitations in systems when both a single-particle gap and a Mott gap are present, in nanotubes with known chirality.

The realization of an electric-field tunable 1D Mott insulator in an individual nanostructure facilitates a model system for studying theories of strong electron interactions (*e.g.* [90]). Moreover, the field-induced Mott transition has been shown to be a basis for the operation of transistors [91]. Our observation of a chirality-independent gap, which can be much greater than k_BT at room temperature for sub-nm diameter nanotubes, could be combined with techniques for growth of small-diameter devices. This would render all nanotubes semiconducting at room temperature, towards application as Mott transistors in nanoelectronics.

Chapter 6

Simultaneous Electrical and Raman Spectroscopy Measurements

6.1 Direct observation of mode selective electron-phonon coupling in suspended carbon nanotubes

Abstract

Raman spectra of individual pristine suspended single-walled carbon nanotubes are observed under high electrical bias. The LO and TO modes of the G band behave differently with respect to voltage bias, indicating preferential electron-phonon coupling and non-equilibrium phonon populations, which cause negative differential conductance in suspended devices. By correlating the electron resistivity to the optically measured phonon population, the data are fit using a Landauer model to determine the key scattering parameters.

Electron phonon coupling in carbon nanotubes has been studied by many research groups [92–98]. In metallic carbon nanotubes (m-CNTs), conduction electrons have been predicted to couple strongly to the Γ-point longitudinal optical (LO) phonons and to the $2k_F$-point transverse optical (TO) phonons. The G band Raman spectra of m-CNTs and semiconducting CNTs (s-CNT) are qualitatively different because of this strong electron-phonon coupling [99]. In metallic nanotubes, the lower-frequency component of the G band (G_-) exhibits a broad Breit-Wigner-Fano (BWF) lineshape, and is significantly downshifted in frequency with respect to its counterpart in semiconducting nanotubes [15]. Recent experiments have shown that this phonon softening can be removed by shifting the Fermi energy of m-CNTs with an applied gate voltage or chemical doping, which modulates this coupling and results in an upshift of the G_- band frequency [100–102]. Density functional theory

calculations have shown that the assignment of the upper and lower frequency components of the G band Raman modes, G_+ and G_-, to the LO and TO Γ-point phonon modes may be reversed in m-SWNTs and sc-SWNTs [16]. This is thought to be caused by the strong downshifting of the LO mode due to the Kohn anomaly, also referred to as a Peierls-like distortion phenomenon [103]. Other experiments have shown that this downshift may be caused by inter-nanotube bundling effects [104].

Negative differential conductance (NDC) has been observed by several research groups at high voltage bias in suspended nanotubes and is understood on the basis of electrons coupling strongly to Γ-point and $2k_F$-point optical phonons (OPs) [36, 105, 106]. At high voltage bias, the electrons emit OPs, causing increased scattering from absorption of those OPs, and an increase in resistance. In the experiment reported here, we simultaneously observe the OP populations and nanotube resistance, and are able to correlate the electron scattering length to phonon population.

When CNTs are heated, the G band downshifts in frequency [107–114], broadens [115], and decreases in intensity [107, 109] due to thermal expansion, which weakens the bonds. In thermal equilibrium, both the LO and TO optical phonons downshift together. We observe preferential downshifting of only one of the OPs at high currents, indicating strong coupling of electrons to only one band and a non-equilibrium phonon population.

Preferential e-ph coupling and coherent phonon generation was first reported in Ruby in 1961 [116], and was followed by other reports describing the phenomenon in GaAs and other semiconductor crystals [117–119]. More recent work analyzed selective amplification and emission of OPs in electron transport experiments [120], and a full quantum treatment of THz phonon laser design [121]. This observation of selective e-ph coupling in carbon nanotubes supports the possibility of using carbon nanotubes as a source of coherent phonons as suggested elsewhere [106]. Suspended SWNTs were grown using CVD on Pt electrodes prepared with islands of lithographically patterned catalyst. Out of 40 devices per chip, typically only a few have just one SWNT bridging the contacts of the device. The trench width for the devices range from 0.5 μm to 2 μm. Figure 6.1 shows one such device fabricated in this study. Raman spectra were measured in a Renishaw InVia spectrometer with a 785 nm Ti-Sapphire laser. An Ithaco current preamplifier was used to measure the current passed through the nanotube.

Sample fabrication proceeds as follows. A trench is first made between two Pt electrodes

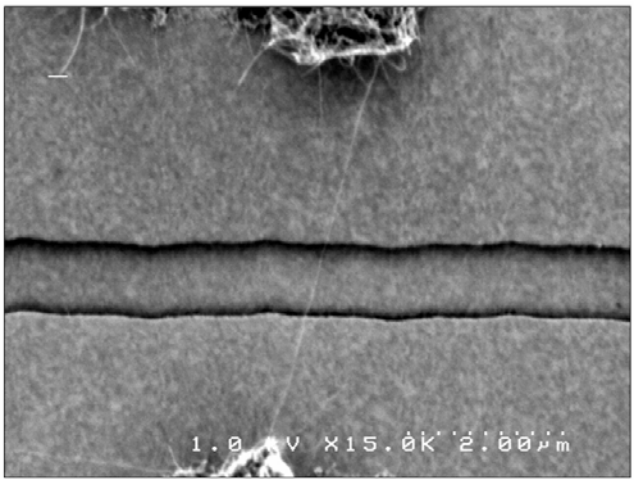

Figure 6.1. SEM image of a suspended carbon nanotube grown on top of Pt electrodes

on a degenerately doped Si substrate by one of two methods [6]. In the first method, Pt electrodes are patterned by lithography on a Si substrate capped with 300 nm of SiO_2, which is then wet-etched in HF using the Pt electrodes as an etch mask. In the second method, the Si substrate is capped with 500 nm of SiO_2 and 50 nm of Si_3N_4. The nitride is then dry-etched in a CF_4 plasma to form the trench, the underlying oxide is wet-etched and the Pt contacts are then patterned. Islands of Fe-Mo catalyst salts in an alumina matrix are then defined on top of the contacts in lithographically defined areas [10]. Nanotube growth is carried out by flowing a mixture of methane (0.5SLM) and hydrogen (0.7SLM) over the wafer for 5 minutes at 800 °C. Devices that show negative differential conductance at high bias (1–2V) with a maximum current of $\sim 10/L$ μA (where L is in μm) correspond to individual suspended single-walled nanotubes, and are selected for further study [36].

Figure 6.2 shows the G band Raman modes of a nanotube device under large voltage biases. The bandgap of this nanotube was determined to be ∼60 meV from the current-gate voltage dependence. The G_+ band is observed to downshift by more than 26 cm^{-1}, while the G_- on average doesn't change by more than 1 cm^{-1}. There is a clear crossing that occurs at ∼1.0V, above which the G_- band becomes higher in frequency than the G_+ band. The linewidths of the G_+ and G_- bands in the nanotube of Figure 6.2 also vary with the applied bias voltage. Here the G_+ band broadens while the G_- band remains largely unchanged. Finally, the intensity of the G_+ band decreases monotonically with bias voltage, while the G_- band remains constant. This behavior suggests preferential heating of the G_+ phonon mode, since the G band Raman spectra are known to downshift, broaden, and diminish in

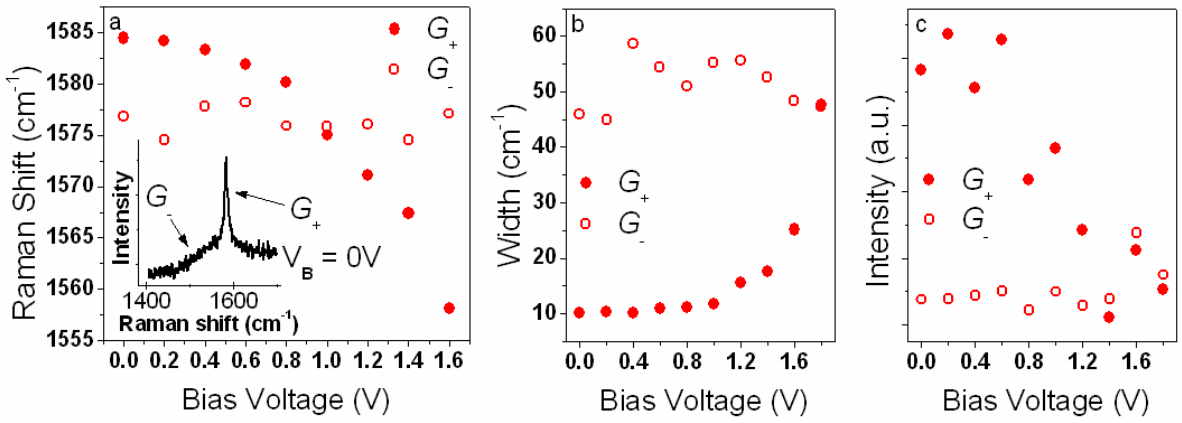

Figure 6.2. G band Raman spectral data versus bias voltage. G band Raman **(a)** shift, **(b)** width, and **(c)** intensity. The inset shows the Raman spectra at zero bias voltage.

intensity with increasing temperature [107–114]. The integrated areas of both the G_+ and the G_- Raman peaks remain constant, indicating that there is no change in the resonance condition of this nanotube with applied bias. Preferential heating of the G_+ phonon was observed in 4 out of 15 devices measured in this study, including one semiconducting device. Because the unbiased G_- band exhibits a broad, downshifted BWF lineshape, we assign it to the LO phonon mode, and we assign the G_+ to the TO phonon mode.

Figure 6.3 shows the G band Raman modes of another nanotube under large voltage biases. NDC can be clearly seen above 1.2V in the current-voltage (I-V_{bias}) characteristics of this device, as shown in the inset of Figure 6.3. Here, the voltage dependence of the G_+ and G_- bands are reversed from those shown in Figure 6.2. Over the range of applied bias voltage, the G_- band is observed to downshift by 15 cm^{-1}, while the G_+ band doesn't change by more than 1 cm^{-1}. Furthermore, the linewidth of the G_- band increases significantly with bias voltage and drops in intensity, while the G_+ band remains of constant width and intensity. Contrary to Figure 6.2, this data exhibits preferential heating of the G_- band, which we again assign to the LO Γ-point phonon mode. This case is rare and was only observed in one out of fifteen nanotubes measured in this study. Again, the integrated areas of both the G_+ and G_- peaks remain constant, indicating that there is no change in the resonance condition. The broadening of the G_+ feature is consistent with thermal broadening in SWNTs as reported by Jorio et al. [115]. Both nanotubes shown in Figures 6.2 and 6.3 are metallic, and all changes in the Raman spectra are reversible.

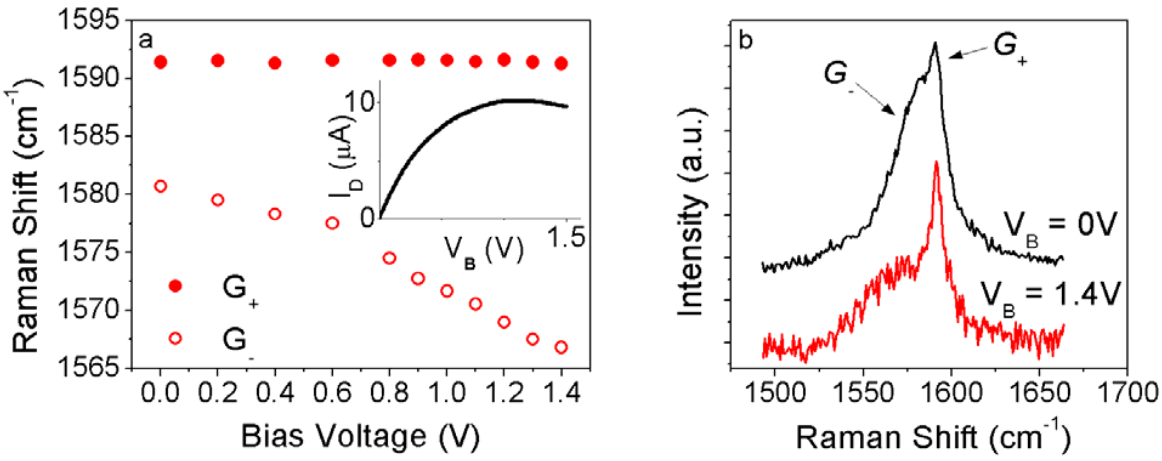

Figure 6.3. **(a)** The G band Raman shift versus bias voltage, with the $I - V_{bias}$ inset exhibiting NDC. **(b)** Raman spectra taken at V_{bias}=0V and 1.4V.

A weak radial breathing mode (RBM) was observed in the Raman spectra of this nanotube at 146.5 cm^{-1}, which corresponds to a nanotube diameter of 1.70 nm by the relation $\omega_{RBM} = 204/d_t + 27$ [122]. The strongly enhanced Raman intensities from suspending the carbon nanotubes off the substrate [123] make it possible to observe RBMs with the incident laser off resonance. The weak RBM observed for this nanotube implies an off-resonance condition, which creates significant uncertainty in the transition energy E_{ii}, and hence the chirality assignment of this nanotube. The maximum current density of this nanotube can be obtained by dividing the peak current (10 μA) by the cross-sectional area of the nanotube (3.81×10^{-18} m^2), obtained by multiplying the circumference of the nanotube with the thickness of graphene (0.355 nm). This results in a peak current density of 5.3×10^8A/cm^2. The behaviors shown in Figures 6.2 and 6.3 can be explained by the previous theoretical work of Piscanec et al. [16], which describes the strong electron-phonon coupling of the Kohn anomalies (KA) in metallic carbon nanotubes. One KA occurs at zero momentum (Γ-point) in the LO phonon band and gives the G$_-$ band in metallic nanotubes its downshifted and broadened BWF lineshape [124]. Another KA occurs at a finite phonon momentum $q = 4p/3T$ (2k$_F$-point) in the TO phonon branch, where T is the length of the unit cell in the nanotube. These two KAs provide the primary source of electron-phonon scattering in pristine m-CNTs at high bias voltages.

It is surprising that the narrow G$_+$ band (TO band) in Figure 6.2 is so strongly coupled

to the electrons, while the broad G_- band (LO band) remains unchanged with applied bias voltage. We can explain this by considering that the energy of the $2k_F$-point phonons associated with the TO KA ($\sim$0.16 eV) is significantly lower than the energy of the G_-point phonons of the LO KA ($\sim$0.195 eV). This results in a lower threshold energy for TO phonon emission in electron transport. Thus the electrons are scattered by emitting TO phonons before ever attaining enough energy to emit LO phonons, which results in heating of only the TO phonon band. This, together with the fact that the electron-phonon coupling for the $2k_F$-point KA is two times stronger than that of the G_-point KA [16], explains why the G_+ band (TO) is observed to be strongly heated for nanotubes of the type shown in Figure 6.2. While the finite momentum phonons cannot be observed directly in first order Raman spectra, the modes in each phonon branch are expected to equilibrate thermally. The orthogonality of the LO and TO phonon bands enables them to remain in a state of extreme non-equilibrium and exhibit preferential heating.

The seemingly contradictory results of Figure 6.3, in which only the G_- band (LO) downshifts with applied bias voltage, can be understood on the basis of a rare chirality, where $R = GCD(n,m)/GCD(2n+m, 2m+n) = 1$, which only occurs for slightly less than 1/3 of all metallic nanotubes. In fact, this behavior was only observed 1 out of 15 nanotubes measured in this study, which is consistent with the rarity of this chirality. In this case, the Raman active TO phonon branch does not exhibit a KA [16], and heating by hot electrons is only observed in the LO phonon band.

The high temperatures reached under large voltage biases were corroborated by anti-Stokes (AS) Raman spectroscopy. A G band anti-Stokes peak was observed at biases above 0.4V on the device shown in Figure 6.3. The ratio of the AS (absorbed phonons) to the Stokes (emitted phonons) Raman intensity is given by the Maxwell-Boltzmann factor $exp(-E_{ph}/k_BT)$, where E_{ph} is the phonon energy (195 meV), k_B is Boltzmann's constant and T is the temperature in Kelvin. Figure 6.4 shows the temperature as determined from the AS/S ratio plotted as a function of electrical power. The temperature shows a linear dependence on electrical power that reaches $\sim$700 °C at high bias. At higher voltages, the nanotube was destroyed. This temperature is consistent with the work of Cataldo, who measured the burnout threshold of carbon nanotubes in air to be $\sim$800 °C [125]. The optical phonon temperature was also determined independently from the downshift of the G_- band by the relation $\omega_{G,LO}(T) = -3.5 \times 10^{-5}T^2 - 6.5 \times 10^{-3}T + 1581.5$, which was

measured on one of our devices in a temperature controlled stage. This data is also plotted in Figure 6.4 and is in good agreement with the anti-Stokes/Stokes ratio data. We would like to point out that, while the anti-Stokes spectra of the LO mode yields a temperature of ~700 °C, the TO mode was not observed in the anti-Stokes spectra. This, together with the lack of change in the TO Stokes Raman frequency, indicates that the population of the TO phonon remains close to room temperature. These data show that the coupling between the two OP polarizations (LO and TO) is very weak, and that they can exist in a state of extreme non-equilibrium.

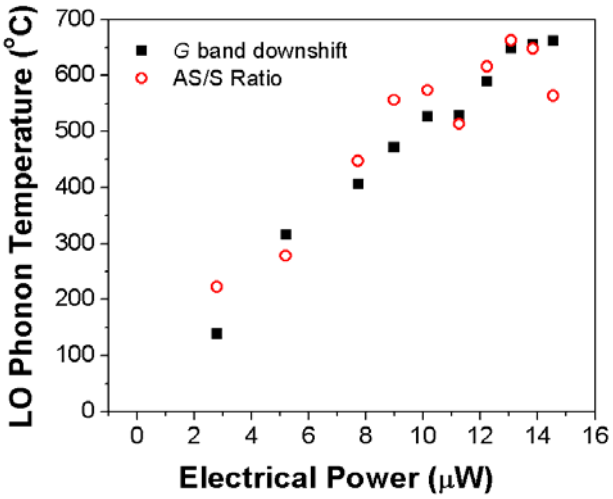

Figure 6.4. Optical phonon temperature versus electrical power. Temperature is measured for the device in Figure 6.3 by anti-Stokes/Stokes Raman spectroscopy and by G band downshift.

By measuring electrical resistivity and optical phonon population simultaneously, we gain new information about the phonon scattering mechanism responsible for the observed NDC as suggested by Lazzeri [106]. Figure 6.5 shows the electrical resistance plotted as a function of LO phonon population $N_{op}(T_{op})$, which is fitted from the experimental data in Figure 6.4. We can understand this data using the Landauer model developed by Pop [36], Mann [105], Park [34], Yao [33], and others [106, 126], in which the nanotube resistance is expressed as

$$R(V,T) = R_c + \frac{h}{4q^2}\frac{L + \lambda_{eff}(V,T)}{\lambda_{eff}(V,T)} \tag{6.1}$$

where R_c is the contact resistance, L is the nanotube length, and $\lambda_{eff} = (\lambda_{ac}^{-1} + \lambda_{op,ems}^{-1} +$

$\lambda_{op,abs}^{-1})^{-1}$ is the bias and temperature dependent electron mean free path [36]. The acoustic scattering length is given by $\lambda_{ac} = \lambda_{ac}^{RT}(300[K]/T_{ac})^{-1}$. The acoustic phonon temperature is $T_{ac} = (T_{op}+\alpha T_{sample})/(1+\alpha)$, where the non-equilibrium phonon coefficient α is taken as 2.3 from Mann et al. [105] and the optical phonon temperature T_{op} is measured by Raman spectroscopy. The optical phonon scattering length for emitted phonons is given by

$$\lambda_{op,ems} = \frac{E_{ph}L}{qV} + \lambda_{op}^{min}\frac{1+N_{op}(300[K])}{1+N_{op}(T_{op}} \tag{6.2}$$

and for absorbed phonons by

$$\lambda_{op,abs} = \lambda_{op}^{min}\frac{1+N_{op}(300[K])}{1+N_{op}(T_{op}}. \tag{6.3}$$

In these equations, E_{ph} is the OP energy, and λ_{op}^{min} is the scattering length for electron scattering from OP emission in the nanotube after the electron has accelerated to high energy $\geq E_{ph}$. Low energy electrons may scatter with this length scale from absorption of thermally populated OPs as well, as described by equation 6.3. In addition to the constant contact resistance R_c, this model has one fitting parameter, λ_{op}^{min}. An approximate value of λ_{ac}^{RT}=2400 nm was used in the fit in accordance with previous work [34], and the fitted value for λ_{op}^{min} was generally found to be insensitive to the value of λ_{ac}^{RT}.

The solid and dashed lines in Figure 6.5 correspond to fits of our data using this model with OP emission and absorption and with OP emission alone, respectively, with λ_{op}^{min}=26 nm. This value is consistent with those reported previously in the literature [34, 35]. The model including OP emission and absorption is in good agreement with the experimental results for phonon populations below 0.09. The failure of the model without OP absorption indicates the important role that the non-equilibrium optical phonon population plays in the electron transport of suspended SWNTs. At larger phonon populations, corrections to the model are needed to account for the non-uniformity of the temperature along the length of the nanotube, as shown previously in finite element thermal analysis calculations [105].

We have performed a systematic study measuring the optical and high bias electronic properties of 5 suspended nanotubes that exhibited preferential downshifting of the G_+ or G_- band. This data has been fit to the model described above and their results are listed in the Figure 6.6. The figure lists the metallic/semiconducting nature and bandgap of the nanotubes, as determined from the electron transport data. The Raman feature

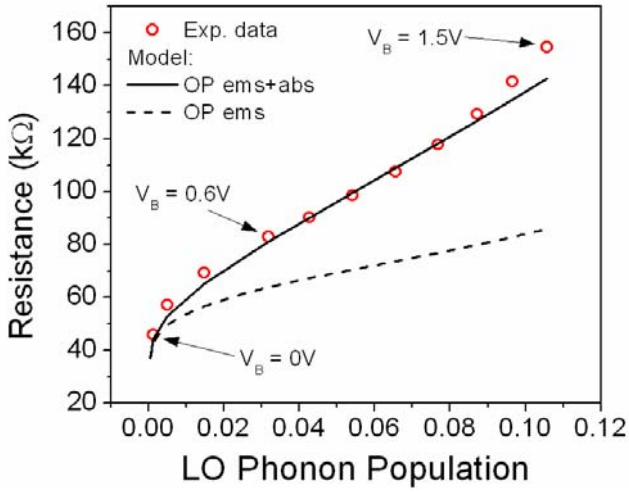

Figure 6.5. Electrical resistance plotted as function of phonon population. The phonon population is fit from the measured data in Figure 6.4, for the device in Figure 6.3. The two models shown are for LO scattering through emission plus non-equilibrium OP absorption and through OP emission alone.

that is preferentially downshifted with bias voltage is also indicated in the figure. The diameter is indicated for nanotubes that exhibited a RBM in their spectra. Despite the very different results observed in their optical spectra, we find little variation in the optical phonon scattering parameter λ_{op}^{min} amongst m-SWNTs.

Sample	Length (μm)	M/SC	Down-shift	d_t (nm)	λ_{op}^{min} (nm)
1	0.5	M	G_+	-	18
2	2	M	G_-	1.7	26
3	1	M	G_+	-	35
4	2	SC	G_+	2.0	9
5	0.5	M	G_+	-	28

Figure 6.6. Summary of electron and phonon parameters of 5 suspended nanotubes

10 out of the 15 nanotubes measured in this study did not exhibit preferential downshifting of the G_+ or G_- bands and were not included in Figure 6.6. In 5 of these 10 nanotubes, the relative intensity of the G_+/G_- bands was so great that a clear resolution of both peak positions was not possible, and hence it was not possible to observe whether preferential

heating occurred. The G_+/G_- intensity ratio has been theoretically predicted and experimentally shown to be a function of chiral angle [127, 128]. We attribute the behavior of these 5 nanotubes to the extreme cases of large and small chiral angles. In the remaining 5 nanotubes not shown in Figure 6.6, both the G_+ and the G_- bands downshifted when heated with electrical current. This is attributed to anomalous phonon-phonon anharmonic coupling, and further indicates the high purity of the pristine nanotube samples that did exhibit strong selective coupling and extreme non-equilibrium phonon populations.

In conclusion, we observe preferential electron-phonon coupling of the G Raman bands in carbon nanotubes under high voltage bias. This preferential coupling is caused by the differences between the two Kohn anomalies in the TO and LO Raman bands. Surprisingly, in most metallic nanotubes, the narrow G_+ band (TO band) is strongly heated by electron-phonon scattering at high biases. Because of the preferential electron-phonon coupling, high voltage biases produce a non-equilibrium phonon population, as observed by anti-Stokes Raman spectroscopy. By correlating the electron resistivity to the phonon population, measured by Raman spectroscopy, we determine the high energy electron-OP scattering length λ_{op}^{min} in m-SWNTs to be $\sim$30 nm.

6.2 Spatially-resolved temperature measurements of electrically-heated carbon nanotubes

Abstract

Spatially-resolved Raman spectra of individual pristine suspended carbon nanotubes are observed under electrical heating. Spatial temperature profiles of the Raman G_+ and G_- bands are obtained for the first time. In these devices, the bands show unequal spatial heating profiles. The non-equilibrium phonon populations are more pronounced in short nanotubes (2 μm) than in long nanotubes (5 μm). These results are understood in terms of the decay and thermalization of non-equilibrium phonons. The measurements reveal the mechanism of thermal transport in nanotubes, which occurs through non-equilibrium phonons in short nanotubes and through thermalized phonons in long nanotubes.

The temperature of a macroscopic solid is manifest in the energy of its lattice vibrations, or

phonons. In nanostructures with dimensions approaching the mean-free-path of phonons, this definition of temperature could break down. This is particularly true if the phonon population is driven out of equilibrium with an electrical current. In this case, some phonon modes can have effective temperatures higher than the rest of the lattice depending on their coupling with the electrical current. In the past, several interesting observations have been made in electrically-heated carbon nanotubes such as current saturation [33], Γ-point and K-point optical phonon scattering [34, 35], ballistic phonons [129] and electrical breakdown [130]. In freely suspended carbon nanotubes, the ability of phonons to relax is hindered on account of not being thermally sunk to a substrate and, as was first observed by Pop *et al* [36], suspended nanotubes showed remarkable negative differential conductance (NDC) at high electric fields. This observation was explained using non-equilibrium or "hot" phonons [36, 93].

These high-field properties are particularly relevant to carbon nanotubes' applications in field-effect transistors and interconnects towards the miniaturization of electronics. It is more insightful to probe these phenomena optically, rather than by transport measurements alone. In particular, since nanotubes are one-dimensional structures with a huge aspect-ratio, these phenomena could vary spatially and a local probe of temperature is necessary to fully understand thermal transport in nanotubes. Previously, scanned force microscopy [39] and local melting of nano-particles [40] have been used to extract local temperatures of multi-walled nanotubes under high bias. However, these techniques suffer from temperature differentials at the measurement contact interface.

Raman spectroscopy is a powerful, non-contact method of probing phonons in nanotubes. This technique enables one to probe the Γ-point longitudinal optical (LO), transverse optical (TO) and the radial breathing mode (RBM) phonons, among others. Recently, hot phonons in nanotubes have been directly observed using Raman spectroscopy in conjunction with electrical transport [131, 132]. Thus, spatial investigation of electrical heating using Raman spectroscopy forms the motivation for our experiment.

Individual single-walled carbon nanotube devices were grown on top of Pt leads, as reported in detail previously [131]. Devices used in this work were grown using ethanol as the carbon feedstock, which has been shown to yield long and low-disorder nanotubes [43]. Figure 6.7 (right inset) shows a scanning electron microscope image of a 5 μm long nanotube device. Raman spectra were measured in a Renishaw InVia spectrometer with

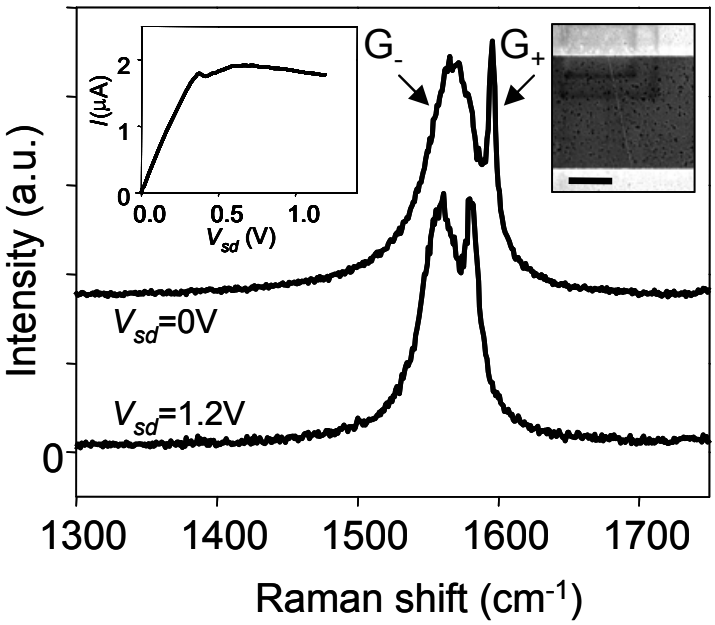

Figure 6.7. Raman spectra of the center of device D1 at two bias voltages. Left inset: I-V characteristics of D1. Right inset: SEM viewgraph of a typical device. Scale bar corresponds to 2 μm.

Spectra-Physics 532 nm solid state and 785 nm Ti sapphire lasers. Typical integration times were 60-120 seconds. An Ithaco current preamplifier was used to measure the current through the nanotube. All measurements were performed in an argon environment to prevent burn-out of devices at high bias voltages. Figure 6.7 (left inset) shows the current-voltage (I-V) characteristics of a typical quasi-metallic device D1 (5 μm long). Note the NDC, characteristic of suspended devices, above $V_{sd} \sim 0.6$ V in D1. In addition, D1 shows a "kink" in the I-V curve at $V_{sd} \simeq 0.4$ V. (This kink has been shown to be absent in vacuum and attributed to heating-induced gas desorption [42].)

Figure 6.7 shows Raman spectra taken at the center of D1 using a 532 nm laser at two bias voltages, V_{sd}=0 V and 1.2 V. Note the narrow G_+ and broad G_- peaks that are characteristic of the TO and LO phonon modes, respectively, of metallic nanotubes. The two peaks downshift unequally in energy on application of a 1.2 V bias voltage. A low enough laser power was used such that the laser itself did not cause any downshift or heating. Note that the defect-induced D band peak in the Raman spectrum, occurring in typical nanotubes around 1350 cm^{-1}, is absent in most of our devices, as it is in D1. This attests to the low-defect nature of our devices.

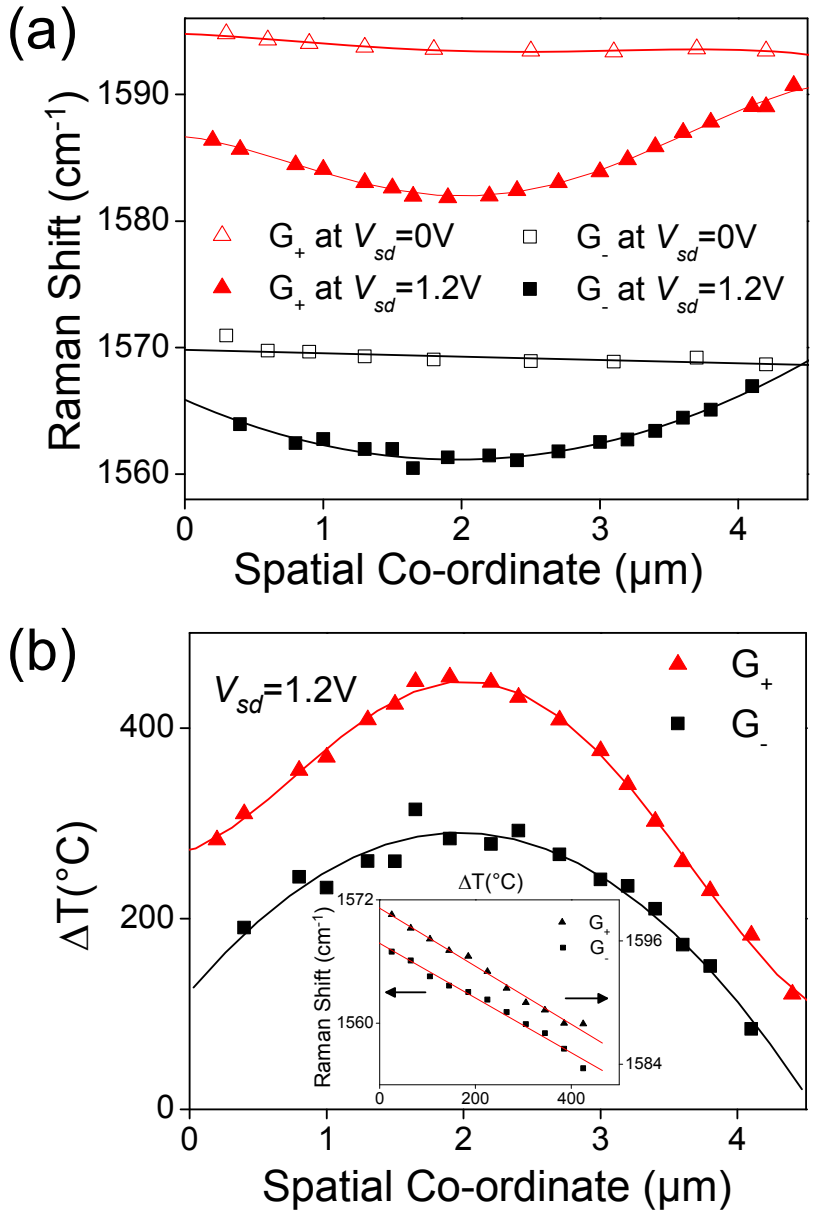

Figure 6.8. Spatial profile of Raman shifts of **(a)** G_+ and **(b)** G_- bands for device D1 at 0 V and 1.2 V bias. **(c)** Temperature profiles of G_+ and G_- bands. Inset: G_+ and G_- shifts for D1 in a temperature-controlled stage

We take spatially resolved Raman spectra of our devices at different bias voltages. The 532 nm laser with a diffraction-limited spot-size of 360 nm, affords 10–20 data points along the length of D1. Figure 6.8(a) shows the Raman shifts of the G_+ and G_- bands, along the length of the nanotube, for V_{sd}=0 V and 1.2 V. At V_{sd}=1.2 V, the bands downshift significantly and develop a spatial profile. The G_+ profile fits to a fourth order polynomial, while a parabola suffices for the G_- profile. The Raman shifts observed at high bias are subtracted from the reference (V_{sd}=0 V) at every spatial point. This corrects for extraneous local variations in the Raman spectra of the nanotube.

Previously, we showed that the downshift of the G_+ and G_- bands could be interpreted in terms of increased phonon populations [131] and hence effective temperatures. This interpretation was in agreement with the Stokes/anti-Stokes intensity ratio observed in that work. In this work, we calibrated the G band downshifts with temperature in a temperature-controlled stage. This calibration data is shown in the inset of Fig. 6.8(b) for device D1. The downshift is linear in temperature, with almost equal slopes for the two bands. The G band temperature is obtained at each point along the nanotube by dividing the voltage-induced change in the Raman shift by the slope of the calibration line. The resulting temperature profiles for the two bands are shown in Fig. 6.8(b).

This result constitutes the first observation of a spatial temperature profile of a single-walled nanotube under Joule heating. Figure 6.8(b) also shows that the temperatures at the ends of the nanotube are higher than room temperature and highly asymmetric, indicative of asymmetric thermal contact resistances. However, the most surprising aspect of Fig. 6.8(b) is that the temperatures of the two bands are quite different. Of ten 5 μm devices studied, 3 devices exhibited G_+ and G_- bands that could be resolved separately with bias voltage. All three devices showed the same qualitative behavior described above. Note that the G band Stokes/anti-Stokes intensity ratio was not resolvable with bias for any of these three devices.

In an earlier work [131], we reported that only one of G_+ or G_- bands downshifted with bias. This observation was most prominent in shorter devices ($\leq 2\mu$m). Figure 6.9(a) shows the G_+, G_- and a third mode (at 1545 cm^{-1}) as a function of bias voltage for such a 2 μm device, D2. In this device, the broad G_- band (LO) downshifts by 35 cm^{-1}, while the other bands remain unchanged within 1 cm^{-1}. The insets of Fig. 6.9(a) and (b) show the I-V and Raman spectrum for D2. Figure 6.9(b) shows the (converted) effective temperature of

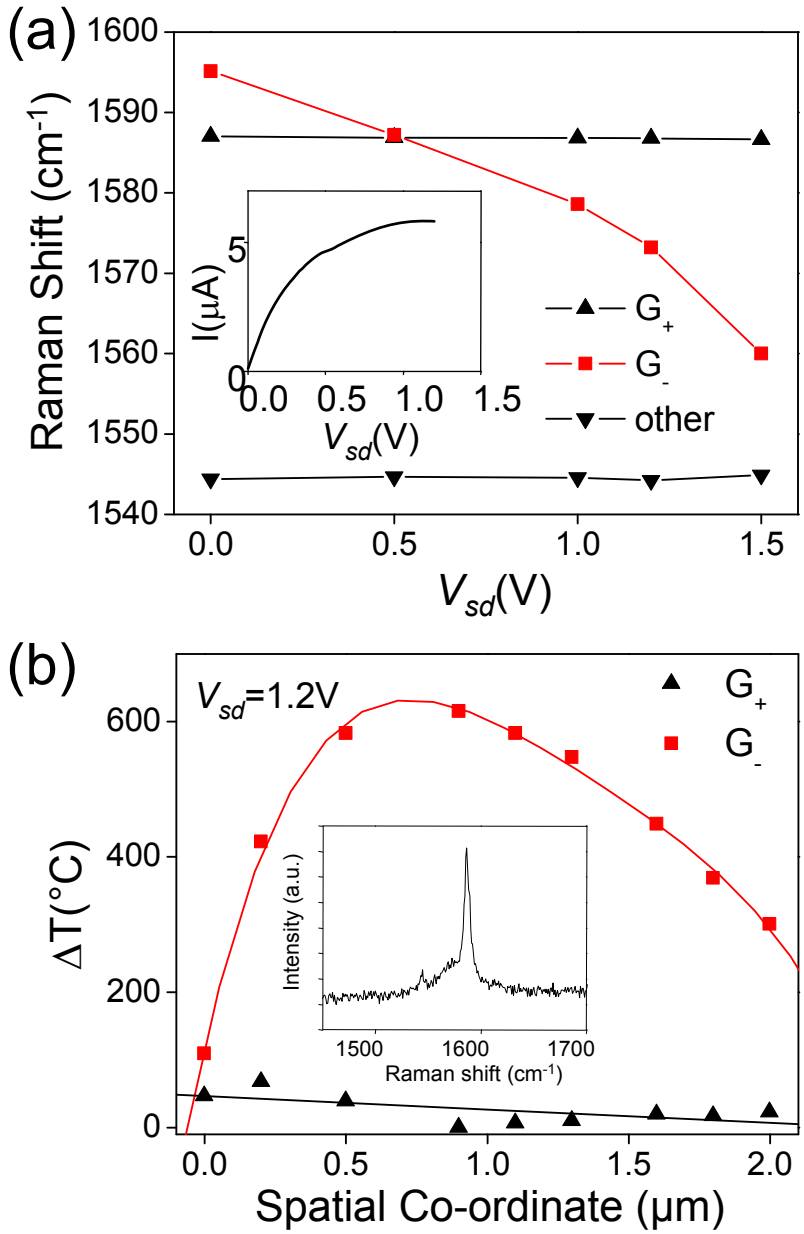

Figure 6.9. **(a)** Raman shifts for device D2 at different bias voltages. Inset: I-V characteristics of D2. **(b)** Spatial temperature profiles of G_+ and G_- bands. Inset: Raman spectrum at the center of D2 at 0 V

the G_+ and G_- bands at V_{sd}=1.2 V, along the length of D2. Surprisingly, while the G_- band shows a non-uniform temperature profile, the G_+ band shows no modulation in space (within the error of the measurement). This seems to be a limiting case of unequal heating, where one band is not heated at all.

We now interpret these results. In thermal equilibrium, both G_+ and G_- downshift equally, as observed in the temperature-controlled stage data of Fig. 6.8(b)-inset. Even in the case of thermal non-equilibrium, each phonon mode is likely to be at least at hot as the lattice. The lower temperature profiles shown in Fig. 6.8(b) and 6.9(b) are, thus, upper bounds on the lattice temperature profile. However, in Fig. 6.9(b) this lower profile coincides with room temperature. Hence, the observation that one of the modes in short nanotube devices does not modulate with bias or space indicates that the lattice remains at room temperature. The other Raman-active mode exists at an elevated non-equilibrium effective temperature, as a direct result of generation by high-energy electrons. In long nanotube devices, these hot phonon modes transfer energy to the pool of thermalized phonons through inter-phonon scattering processes, thus heating up the rest of the lattice.

For a quantitative approach, we first model the hot phonon profile of the simpler case of no lattice heating (Fig. 6.9). In this case, thermal transport is not governed by Fourier's law (diffusive heat transport), since the thermalized phonons are not heated. Instead, one needs to understand the decay process of the hot phonons. Consider a nanotube of length L under uniform heating by an electric current I (this assumption is substantiated by finite element calculations showing that the resistivity of the nanotube does not change by more than 10% along the length of the nanotube). Let $g(I)$ be the hot phonon generation rate per unit length, d be the phonon decay length and τ be the decay time. Hence, a phonon generated at point x has a probability of reaching point x_0 given by $exp(-|x-x_0|/d)$, which is a general characteristic of decay processes. Considering phonons arriving from both directions and a decay rate of n/τ, where n is the phonon population at any point, the continuity equation gives:

$$\frac{dn}{dt} = \int_0^{x_0} g(I) e^{-\frac{x_0 - x}{d}} dx + \int_{x_0}^{L} g(I) e^{-\frac{x - x_0}{d}} dx - \frac{n}{\tau} = 0. \tag{6.4}$$

Plotting the solution for L=2 μm, one obtains a good match to the temperature profile of G_- in Fig. 6.9(b) using a decay length $d \sim 1\mu$m.

We also need to understand the mechanism of power dissipation. In device D2, at a bias V_{sd}=1.2 V, the power input to the nanotube is 6 μW. This power should be carried away mainly by thermal conduction along the nanotube. Other mechanisms of energy transfer, such as radiation or heat sinking to the gaseous atmosphere, have been shown to be negligible (see *e.g.* [105]). The electronic contribution to thermal conduction is also known to be a small fraction (1/5th or less) of the equilibrium lattice contribution [133]. An upper bound to the lattice thermal conductance, G_{th}, of nanotubes in quasi-equilibrium is the ballistic phonon case (theory [134] predicts that the phonon mean-free-path at room temperature in nanotubes is $\sim 1\mu$m. Hence it is not unreasonable to consider ballistic phonon transport). At room temperature, $G_{th} \sim 8r_t$ W/K [134], where r_t is the nanotube radius in meters. A weak RBM was observed in the Raman spectra of this nanotube at 240 cm^{-1}, which corresponds to a nanotube diameter of 0.96 nm by the relation $\omega_{RBM} = 204/d_t + 27$. This yields a thermal conductance of 4 nW/K for the nanotube assuming near equilibrium conditions. From the relation $\dot{Q}= G_{th}/\Delta T$, the lattice cannot conduct away the 6 μW of power without heating to extremely high temperatures. However, such lattice heating is not supported by our observation, as discussed earlier.

An explanation for this apparent mismatch between heat generation and conduction lies with the hot phonons. The estimate for G_{th} assumes that all phonon modes are in thermal equilibrium. Using the Landauer model for phonon transport to calculate the thermal power conducted [133],

$$\dot{Q}_{ph}= \sum_m \int_0^\infty \frac{dk}{2\pi} \hbar\omega_m(k) v_m(k) \eta(\omega_m, T_{hot}) \zeta(\omega_m), \tag{6.5}$$

we can estimate an upper bound for the heat transport by hot modes in the ballistic phonon limit. In equation 6.5, η is the Bose-Einstein distribution function, ζ is the transmission, set to 1 [133], v_m is the group velocity of the mth phonon mode and $\hbar\omega_m$ is the phonon energy. Since the effective temperatures under consideration (T_{hot} ~900 K) are much smaller than $\hbar\omega_m$ (~2000 K), the distribution can be taken to be constant. Integrating over the range of energies of these phonons (1300–1600 cm^{-1}), equation 6.5 reduces to $\dot{Q}_{ph}= 0.185N\eta$ μW, where N is the total number of hot phonon modes. Since $\eta \simeq 0.1$ in our case, it is possible to dissipate the generated heat if $\simeq$150 phonon modes participate in heat transport. This is smaller than the total number of phonon branches of D2 and hence reasonable. Figure

6.10(a) shows a schematic of this heat removal mechanism (see top for short devices).

With this understanding of hot-phonon decay and thermal transport for the strongly non-equilibrium case, we now consider the longer devices, which show conditions closer to equlibrium. As Fig. 6.10(a) (bottom) shows, the bulk of the lattice becomes heated because the devices are long enough for the hot phonons to thermalize. In this case, the lattice could carry away a significant proportion of the heat generated. Since the lattice is almost as hot as the non-equilibrium phonons, we can estimate the thermal conductivity in the limit that all the heat were to be carried away by the lattice. The value of thermal conductivity thus obtained can indicate the validity of this assumption. We use an iterative Fourier's law approach along with the Landauer model for electron transport, as developed in [36]. Following their formulation:

$$A\frac{d}{dx}(\kappa(x)\frac{dT_{ac}}{dx}) + I^2\frac{dR(\lambda_{eff})}{dx} = 0 \tag{6.6}$$

with

$$\lambda_{eff}(T_{ac}(x), T_{op}(x)) = (\lambda_{ac}^{-1}(x) + \lambda_{op,ems}^{-1}(x) + \lambda_{op,abs}^{-1}(x))^{-1}. \tag{6.7}$$

Here, $\kappa(x)$ is the thermal conductivity and $R(x)$ is the resistance, corrected for contact resistance $\sim$25 kΩ and dependent on the effective electron mean-free-path $\lambda_{eff}(x)$. $\lambda_{eff}(x)$ is a function of the lattice temperature T_{ac}, hot phonon temperature T_{op} (which are known from our measurement) and scattering parameters $\lambda_{ac,RT}$, $\lambda_{op,min}$ [36]. The spatial variation of the parameters necessitates the use of a finite element iterative calculation. Using suitable values for the scattering lengths (as obtained from experiment [34, 35]), $\lambda_{ac,RT}$=1.6 μm and $\lambda_{op,min}$ $\sim$180 nm, we can obtain a spatial variation of the thermal conductivity. Note that the thermal conductivity as obtained from Fourier's law (eqn. 3) is extremely sensitive to the diameter of the nanotube. While device D1 did not show an RBM in its Raman spectrum, similar data was obtained from device D3 (L=4.6 μm, ω_{RBM}=124 cm^{-1}, d_t=2.1 nm). The above analysis yields a spatial variation of thermal conductivity for D3 as shown in Fig. 6.10(b).

We note that the magnitudes of κ are similar to other measurements on single-walled nanotubes [135], thus validating the assumption in longer devices that the lattice is the dominant heat carrier. The hot-phonon thermalization length is thus larger than 1 μm and at most 2.3 μm, considering $L/2$. Note that κ shown in Fig. 6.10(b) approaches 6000

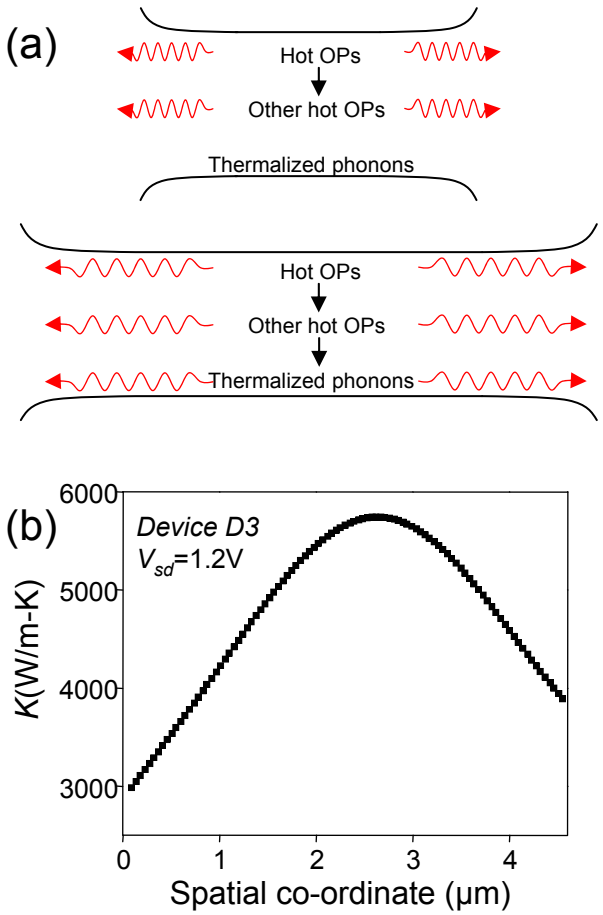

Figure 6.10. **(a)** Proposed mechanism for thermal transport in short and long devices. **(b)** Calculated spatial variation of thermal conductivity for device D3

W/m-K at 900 K and is among the highest reported for any material. Our analysis also shows an almost-linear T dependence much above room temperature, as theoretically predicted [134]. Our observation deviates from estimates on multi-walled nanotubes [38, 129], which show a downturn and $1/T$ dependence beyond room temperature due to Umklapp scattering. Theory predicts that the onset of Umklapp scattering occurs above 1000 K [134]. However, the presence of multiple shells or defects in multi-walled nanotubes could cause this downturn at the lower temperatures observed by these groups.

Our data also allows a direct estimate of thermal contact resistance, R_{th}. Previously, laser heating of nanotubes was used to determine the ratio of thermal contact resistances of the left (L) and right (R) lead, $R_{th,L}/R_{th,R}$ [136]. In our case, since both temperature and heat flow are known, we can directly compute both $R_{th,L}$ and $R_{th,R}$. For D1, we obtain

$R_{th,L} \simeq 8 \times 10^7$ K/W and $R_{th,R} \simeq 10^7$ K/W respectively. Similar values are obtained for other devices. The asymmetry is device specific and likely dependent on the nanotube-metal contact interface. Thermal contact resistance, thus, accounts for a significant temperature drop at the ends of the nanotube.

In summary, the spatial temperature profile of a single-walled nanotube is obtained for the first time. This measurement provides insights into the mechanism of thermal transport and gives a measure of the thermal conductivity and thermal contact resistances of carbon nanotubes.

Chapter 7

Ballistic Phonon Thermal Transport in Multi-Walled Carbon Nanotubes

Abstract

We report electrical transport experiments using the phenomenon of electrical breakdown to perform thermometry that probe the thermal properties of individual multi-walled carbon nanotubes. Our results show that nanotubes can readily conduct heat by ballistic phonon propagation. We determine the thermal conductance quantum, the ultimate limit to thermal conductance for a single phonon channel, and find good agreement with theoretical calculations. Moreover, our results suggest a breakdown mechanism of thermally activated C-C bond breaking coupled with the electrical stress of carrying $\sim 10^{12}$ A/m^2. We also demonstrate a current-driven self-heating technique to improve the conductance of nanotube devices dramatically.

The ultimate thermal conductance attainable by any conductor below its Debye temperature is determined by the thermal conductance quantum [137, 138]. In practice, phonon scattering reduces the thermal conductivity, making it difficult to observe quantum thermal phenomena except at ultra-low temperatures [139]. Carbon nanotubes have remarkable thermal properties [140–143], including conductivity as high as ∼3000 W/m K [38]. Here we report the observation of ballistic phonon motion and quantum thermal transport in micron-scale individual carbon nanotube devices, demonstrating the universal limit to thermal transport. In this qualitatively different regime, quantum mechanics limits the entropy flow, giving a maximum thermal conductance and an absolute physical limit to the information bandwidth that a nanotube can transport per unit power [137, 138]. From our data, we obtain a measurement of the thermal conductance quantum that is in good agreement

with theory.

Very recently the thermal conductance of a carbon nanotube attached to an AFM tip has been observed to be independent of the AFM retraction length, and the result was interpreted in terms of ballistic phonon propagation [144]. However, the phonon scattering length and thermal conductance quantum were not determined. In our experiments, we heat multi-walled nanotubes (MWNTs) with an electrical current and monitor temperature by the electrical breakdown phenomenon [130, 145]. Our data yields an experimental measurement of the thermal conductance quantum, which agrees with theoretical predictions [133, 137, 138] as well as thermal transport results on cryogenically-cooled Si_3N_4 nanobridges [139]. This demonstrates that fundamental knowledge about thermal transport in nanotubes can be obtained from an electrical transport experiment. This knowledge, which is challenging to obtain by other means, also contributes toward understanding thermal management issues relevant to the rational design of nanotube interconnects and logic devices.

Fabrication of free-standing and substrate-supported MWNT devices was described elsewhere(e.g. [21, 146]). A device diagram is shown in Fig. 7.1(a) and a scanning electron microscope (SEM) device image in Fig. 7.1(b). We mainly studied devices in which electrical leads were placed over the tubes. In the work of Collins et al. [130], it was shown that sufficiently high electrical power dissipation in MWNTs causes the current I to drop in abrupt events separated by $\sim$1 s, due to the ablation of individual nanotube shells, behavior recently imaged by transmission electron microscopy (TEM) [147]. It was carefully argued that the breakdown temperature T_B was $\sim$900 K [130]. Nevertheless, Joule heating alone is not likely to account entirely for the shell breakdown [148].

To address the role of T_B in the breakdown process, we compared the behavior of both freestanding devices and supported nanotube devices. In the latter, the substrate provides an additional cooling pathway for the nanotubes. Figure 7.1(c) shows current-voltage (IV) data from three freestanding nanotube devices with radius R=10 nm, determined by SEM imaging. The samples' lengths L were 0.50 μm, 0.64 μm, and 1.58 μm, respectively (top to bottom). At breakdown, the resistance is directly proportional to the nanotube length, indicating that it originates primarily from the nanotube. The IV curves end at an abrupt $\sim$10 A current drop, marked by the black circles, indicating shell breakdown. The voltage V was then quickly reduced, to prevent further shell breakdown [145]. The dotted line is a

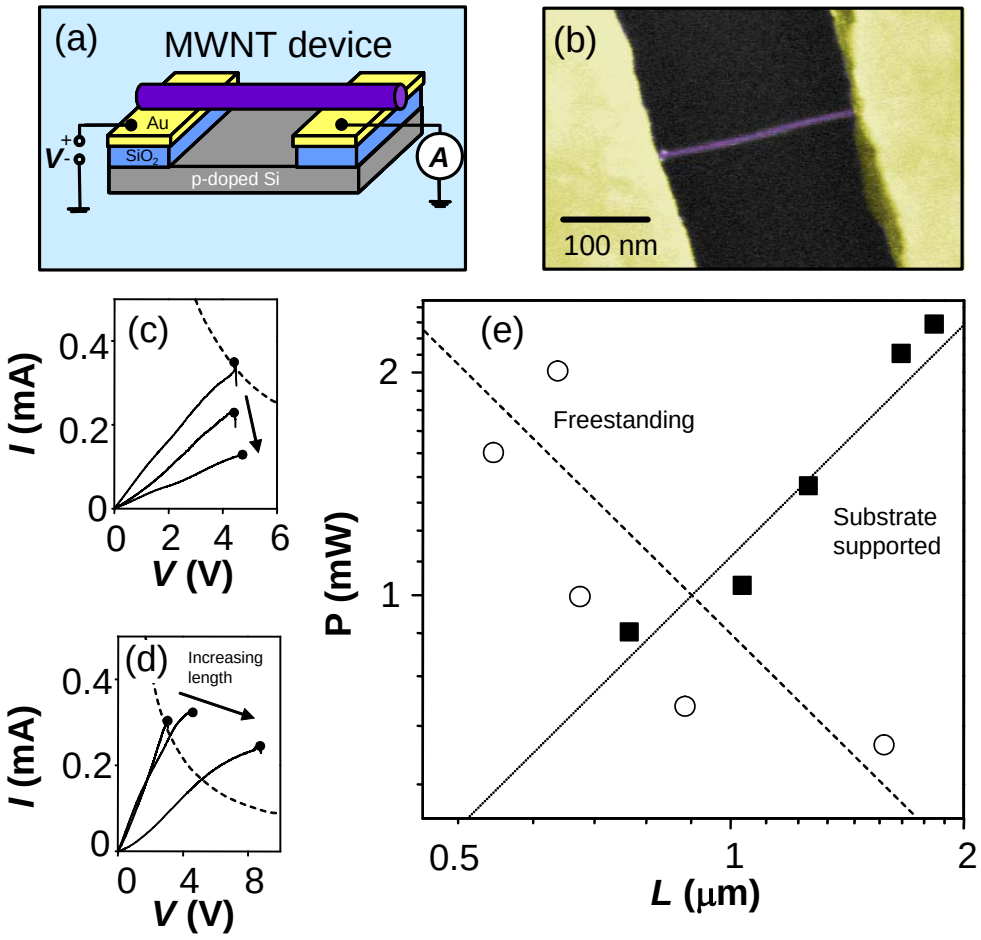

Figure 7.1. **(a)** Diagram of a freestanding multiwalled nanotube device. **(b)** SEM image completed device. **(c)** IV characteristics from freestanding nanotube devices with R=10 nm. The arrow indicates increasing lengths. Dotted line: iso-power curve. **(d)** IV characteristic of substrate-supported devices with R= 8 nm, 9 nm, and 14 nm, increasing in length following the arrow. Dotted line: iso-power curve. **(e)** P vs. L on a log-log scale for freestanding tubes (open circles) and substrate supported nanotubes (filled squares). Dotted line: $P \propto L$, dashed line: $P \propto L^{-1}$

constant power curve corresponding to the breakdown power P for the shortest tube. From this, we deduce that increasing L leads to decreasing P.

Figure 7.1(d) shows IVs from supported nanotube data with L= 0.74 μm, 1.26 μm, and 1.66 μm, for curves with ends going from left to right, respectively. P increases with L, showing the opposite behavior from free-standing nanotubes, and is relatively insensitive to R.

Figure 7.1(e) shows a log-log plot of P vs. L. Free-standing tubes approximately follow $P \propto L^{-1}$ behavior, while the supported tubes exhibit $P \propto L$ behavior. This behavior can be understood using a diffusive thermal transport model. For freestanding tubes, the necessary power P to increase the temperature at the tube center by ΔT is then $P = 8\pi R^2 \kappa \Delta T/L$, where κ is the characteristic nanotube thermal conductivity. Taking the previous estimate $T_B \sim$900 K [130], a linear fit to our data with ΔT=600 K [dashed line in Fig. 7.1(e)] yields a thermal conductivity of $\kappa \approx 600$ W/m K, consistent with previous thermal conductivity measurements on individual MWNTs in the diffusive regime [38]. For supported nanotubes, the relation $P \propto L$ indicates that the cooling occurs mainly by heat conduction into the substrate. We estimate heat transport in this geometry as between concentric cylinders. This yields $P = 2\pi L \kappa \Delta T/ln(R_0/R)$, with R_0 the outer cylinder radius at which T drops to the ambient value, and κ the substrate thermal conductivity. Taking R_0=50 nm, and R=10 nm the fit shown by the dotted line in Fig. 7.1(e) yields $\kappa \sim$0.5 W/m K, in agreement with the bulk thermal conductivity of SiO_2, $\kappa \approx$1.5 W/m K. Considering the two cases together, our data and analysis indicate that the shell ablation occurs at a well-defined temperature T_B.

We now focus exclusively on freestanding nanotube devices, representing a broad range of L and R values. Figure 7.2 shows $P/8\pi R^2$ vs. L^{-1} for $\sim$30 samples. Based on diffusive heat transport, we expect plotting the normalized power $P_N = P/8\pi R^2$ vs. L^{-1} should yield a straight line with a slope of T_B. Remarkably, although the initial trend for the longer tubes appears linear, for nanotubes with $L^{-1} \gtrsim (0.5\text{ m})^{-1}$ (filled squares) P_N saturates and becomes L independent. This shows that heat flow from the nanotube occurs at an L-independent rate, depending only on R. The rest of the shells are then broken, producing a gap in the nanotube. The Fig. 7.2 inset shows the gap position, normalized to the suspended tube length. This breakpoint is near the center for tubes longer than $\sim$0.5 μm, but for L in the saturation regime the scatter in the breakpoint values increases. As the statistical

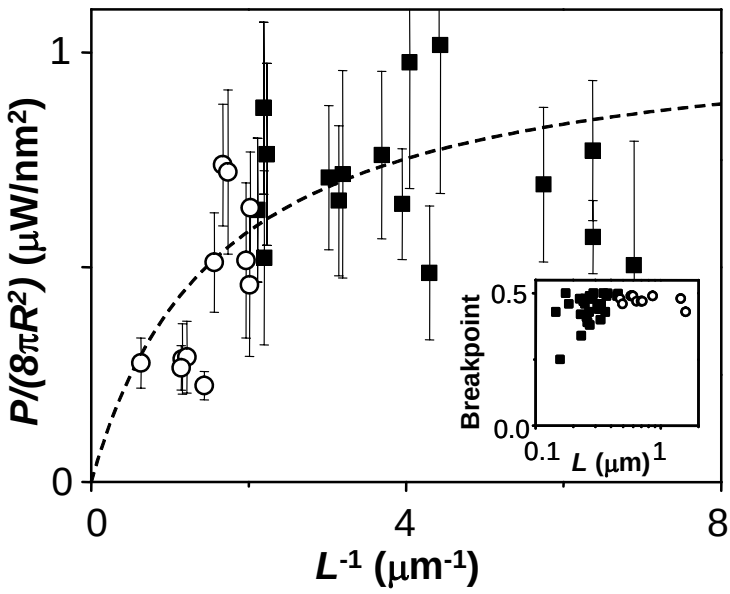

Figure 7.2. $P/(8\pi R^2)$ vs. L^{-1}. Open circles: longer tubes L^{-1}. Shorter tubes: filled squares. Dashed line: fit to data to an interpolation formula described in text. Inset: breakpoint position normalized to L vs. L on log scale

distribution of breakpoints reflects the temperature distribution along the nanotube, this suggests the nanotube temperature becomes more spatially uniform as they become shorter than $\sim$0.5 μm.

Figure 7.3(a) shows P vs. R on a log-log scale. Data from short tube samples and linear fit, showing that$P \propto R^{\alpha}$, with α=2.1. Some data from longer samples, fall near the line, but for the longest nanotubes, the data points fall below the line. The curve followed by the short nanotube data represents an upper limit to P; modulo experimental scatter, data for each nanotube falls on or below the curve and achieves the maximum only for nanotubes with $L \leq$0.5 μm. The Fig. 7.3(a) inset shows the same data and fit on a linear scale.

We now consider potential interpretations for this behavior. One possibility is that a dominant metal-nanotube thermal contact resistance κ_C produces the saturation seen in Fig. 7.2. This is unlikely, however, as κ_C was determined to be negligible in ref. [38], which also used metal contacts as thermal reservoirs, as well as in ref. [144] which used graphite contacts as a thermal reservoir. Finally, based on the supported tubes' behavior, we would expect κ_C, and hence P, to be approximately independent of R. The observed systematic relationship $P \propto R^2$ differs sharply from this expectation.

Another possibility is that because of ballistic electron transport [149], the electrical

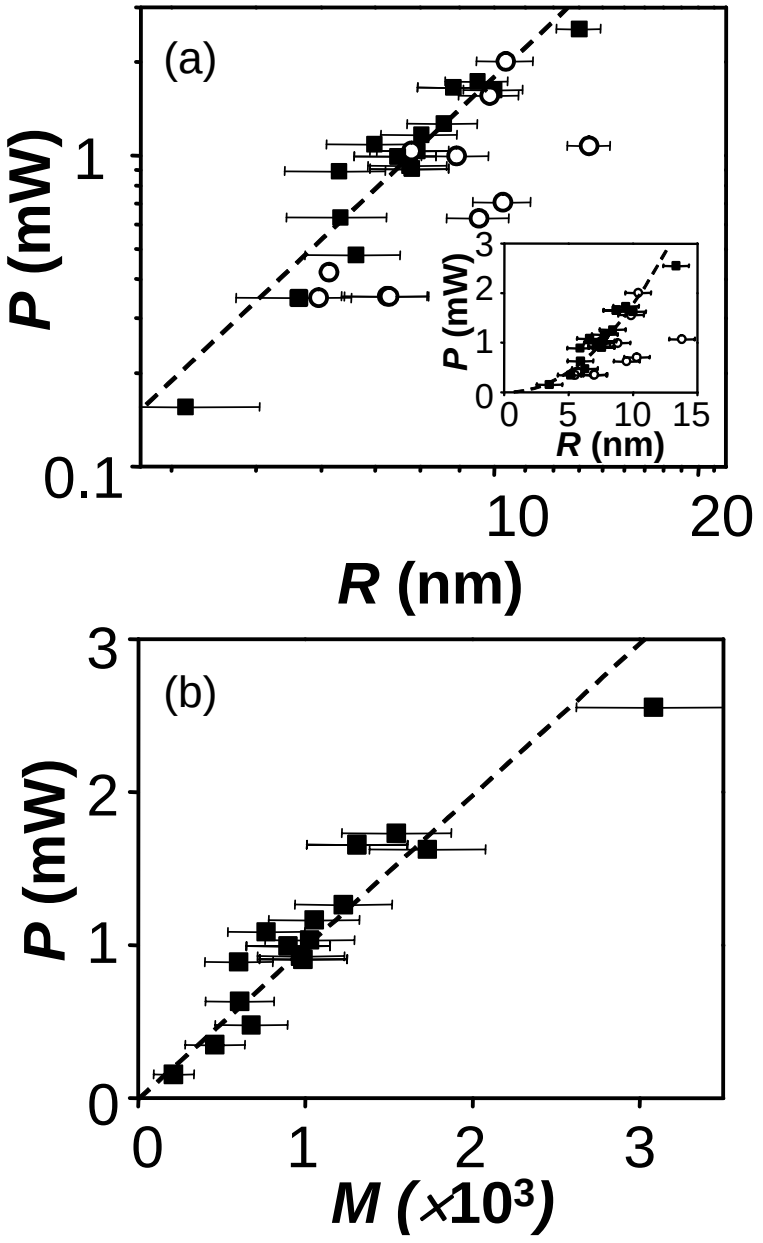

Figure 7.3. **(a)** Log-log plot of P vs. R. Open circles: longer tubes. Shorter tubes: filled squares. Dashed line: linear fit to short nanotube data. Inset: same data and fit on a linear scale. **(b)** P vs. M. Dashed line: linear fit through origin to data taken from nanotubes with $L < 0.6$ μm

current primarily heats the electrodes. In this case, the required power to reach T_B may be relatively L-insensitive. However, both experiments and theory [33, 34] indicate the electronic mean free path due to phonon emission at the high biases applied to our samples is ∼10 nm. Since each optical or zone boundary phonon emission is associated with an energy ∼180 meV [34], we expect even for our shortest nanotube studied (∼150 nm) most of the energy eV provided by the electric field to each electron is converted into phonons within the nanotube.

We now discuss the possibility of ballistic phonon transport within the nanotube. In this picture, a diffusive heat transport regime with Umklapp inter-phonon scattering as the dominant scattering mechanism [38] makes a transition to a ballistic center-of-mass motion regime for sample lengths L ∼0.5 μm. This suggests the temperature distribution along the tube should broaden as L decreases, consistent with the data in the Fig. 7.2 inset. Furthermore, because the characteristic distance the phonons travel before escaping the tube is $\sim L/2$, we would infer a characteristic Umklapp scattering mean-free path l_U ∼0.2 μm. We note that this situation, where the electron mean free path is shorter than l_U, is reminiscent of the conditions prevailing in silicon-based transistors [150]. This must be accounted for to understand thermal management in Si transistors. Similar issues may therefore occur in nanotube transistor devices.

In the ballistic regime, the heat flux carried by the phonons P is given by [133, 139]

$$P = \sum_n \int \frac{d\omega_n}{2\pi} \hbar\omega_n [\eta_{ne}(\omega_n) - \eta(\omega_n, T_0)] \xi(\omega_n) \tag{7.1}$$

where the integration is over each of the nth photon modes bandwidths, $\eta_{ne}(\omega_n)$ is the non-equilibrium phonon distribution for the nth phonon branch, $\eta(\omega_n, T_0)$ is the Bose-Einstein distribution corresponding to the phonons injected into the nanotube at the electrode temperature T_0, and $\xi(\omega_n)$ is the transmission coefficient for phonons escaping into the electrodes.

We now make several assumptions to simplify eq. 7.1. Although the geometry dependence of $\xi(\omega_n)$ for various situations was calculated by Rego and Kirczenow [151], our geometry of an extended lateral contact was not addressed. However, considering the negligibility of κ_C as discussed above, as well as the relatively large characteristic thermal phonon wavevector ∼10^{10} m^{-1} compared to that studied in ref. [151], we take $\xi(\omega_n)$ ≈1.

Moreover, since $T_B >> T_0$ we neglect $\eta(\omega_n, T_0)$ relative to $\eta_{ne}(\omega_n)$. Since breakdown depends on P, rather than V or I separately the hot phonons emitted by the electrons likely achieve thermodynamic equilibrium over a thermalization length $l_{th} \ll L$ after a few L independent characteristic number of collisions. Thus we set $\eta_{ne}(\omega_n) = \eta(\omega_n, T)$, where T is the tube temperature. We also set $\omega_{n,min} \approx nc/R$ [152], where c ~1.5×10^4 m/s is the in-plane speed of sound in graphite [153]. Since T_B is considerably less than Θ_D ~2500 K, the graphene Debye temperature, we replace $\omega_{n,max}$ by infinity. Finally, motivated by the observed $P \propto R^2$ relationship we assume that the thermal current is carried by the different nanotube shells in parallel.

Summing over the contribution from each shell in the MWNT spaced by a=0.34 nm independently (justified by weak coupling between graphite sheets), the power dissipated by phonons exiting the nanotube is then

$$P_{ph} \approx 2\zeta(3)(k_B T)^3 \frac{R^2}{\pi \hbar^2 ac} \tag{7.2}$$

taking into account the heat flow into both contacts and phonon mode degeneracy factor of two, with ζ the Riemann zeta function. Note that this expression contains no free parameters. We rewrite eq. 7.2 as $P_{ph} = 2M\kappa_Q T$, analogous to the well-known Landauer formula for the ballistic conduction of electrons. Here $M \approx 1.5\pi k_B T R^2/hac$, corresponding to the characteristic number of occupied phonon branches, and $\kappa_Q = \pi^2 {k_B}^2 T/3h$ is the thermal conductance quantum [137, 138].

Plotting P vs. M for samples shorter than ~0.5 μm should thus yield a straight line with a slope of $2T_B\kappa_Q$. Figure 7.3(b) shows such a plot with T=T_B=900 K for tubes with $L \lesssim$0.5 μm. The data closely follows a straight-line with a fitted slope of 1.0 μW/branch. From this, we infer a value for the thermal conductance quantum of 6 10^{-10} W/K. This is the key experimental finding of this work. Although the accuracy of this measured value of κ_Q is somewhat limited by the uncertainty in T_B and the assumptions of our model, our experimental determination of κ_Q is nevertheless in good quantitative agreement to the theoretical value κ_Q=9×10^{-10} W/K. This demonstrates that we readily reach quantum mechanical limits to thermal transport in our nanotube devices that act as ballistic phonon waveguides. This is the first such observation for a nanostructure under ambient conditions, enabled by the unique thermal properties of carbon nanotubes.

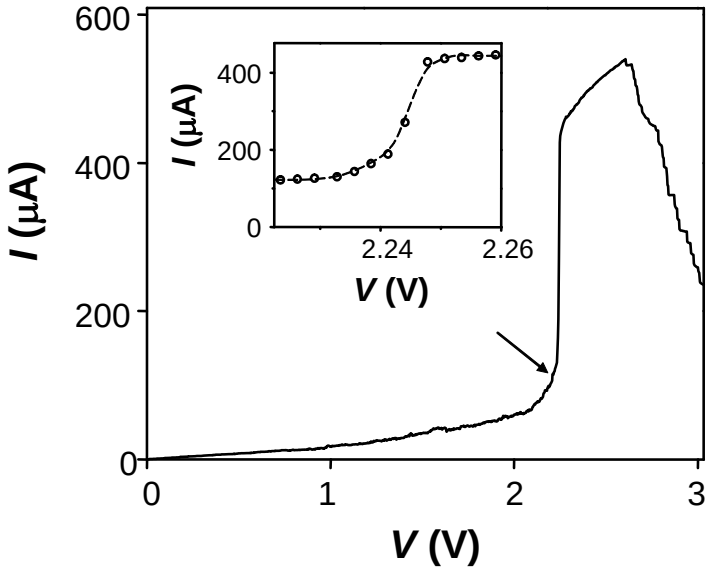

Figure 7.4. *IV* characteristic of a freestanding nanotube device with R=14 nm. The arrow indicates a dramatic current increase. Inset: expanded view of data in the rapid-increase region

From our model and the data of Fig. 7.2 we also obtain an estimate for the phonon mean free path, which was not determined in ref. [144]. Since the thermal conductance in the diffusive limit may be written as $K = \lambda M \kappa_Q / L$, where λ is the phonon mean free path we can obtain an interpolated expression for the power, appropriate to T=900 K, that agrees with the asymptotic limits discussed earlier, $P_{int} = 2M\kappa_Q L^{-1}/(L^{-1} + 3/8\lambda)$. The dashed line is a fit of $P_{int}/8\pi R^2$ to the data of Fig. 7.2 with λ=220 nm, yielding a satisfactory fit to the data over the entire length range with only a single free parameter.

Furthermore, our data yields insight into the breakdown process. The well-defined breakdown temperature suggests it requires an initial defect-forming step with activation energy Δ. We expect the defect formation rate is $\Gamma \sim N\omega_A exp(-\Delta/k_B T_B)$, where ω_A is a characteristic attempt frequency, and N is the number of atoms in the tube at temperature T_B ∼900 K. We find Δ ∼3–4 eV with Γ=1 s^{-1}, a range of ω_A ∼10^8–10^{18} s^{-1} and N ∼10^6, highly insensitive to the choice of N and Γ. One possible origin for Δ is the formation of a Stone-Wales defect. However, our estimated Δ is considerably smaller than the theoretically determined barrier ∼10 eV to form a Stone-Wales defect in graphite and MWNTs [154] ruling out this possible mechanism.

Our data suggests instead a shell breakdown mechanism based on thermal activation of

bond-weakening $\sigma - \pi^*$ electronic transitions, similar to the results of scanning tunneling microscope (STM) cutting experiments [155] which were interpreted as originating with the *electronic* excitation of such transitions [156]. Indeed, the characteristic energy cost $E_{\sigma-\pi^*}$ $\sim$3.6 eV(see e.g., ref. [153]) is close to our estimated Δ $\sim$3–4 eV. Finally, we are able to improve nanotube device conductance considerably using the electric current flow. Freestanding samples with initial low-bias resistance $\sim$50 kΩ up to 10 MΩ typically show a rapid increase in conductance as the voltage across the sample is ramped, such as shown in Fig. 7.4. At higher voltages, a cascade of shell ablation begins and the current decreases in a stepwise fashion. The inset shows that the rise in conductance occurs in a smooth fashion. This behavior may be related to the structural annealing recently imaged by TEM [147]. Further experiments, however, are necessary to fully clarify the origins of this behavior, which is of practical value in addressing the challenge of obtaining a high yield of conductive nanotube devices.

Chapter 8

Carbon Nanotube Linear Bearing Nanoswitches

Abstract

We exploit the remarkable low-friction bearing capabilities of multi-walled carbon nanotubes to realize nanoelectromechanical switches. Switching occurs through the sliding of the inner nanotube shells to close the gap, producing a conducting ON state. For double-walled nanotubes in particular, a gate voltage can restore the insulating OFF state. Acting as a non-volatile memory element capable of several switching cycles, our devices are straightforward to implement, self-aligned and do not require complex fabrication or geometries allowing for convenient scalability.

Microelectromechanical structures have produced a wealth of novel devices for sensing, actuation, and lab-on-a-chip applications. Making smaller nanomechanical systems promises faster and more compact versions of their larger counterparts, opening up the possibility of highly-integrated nanoscale machines and logic circuits [157, 158]. However, challenges such as friction and precise control of device geometry remain important obstacles to the miniaturization of mechanical systems. Carbon nanotubes promise to address many of these challenges because of their intrinsic nanoscale dimensions, mechanical stiffness, structural perfection, and low inter-shell friction. Here we exploit the remarkable low-friction bearing capabilities [159–161] of multi- and double-walled carbon nanotubes (MWNTs and DWNTs) to realize a nanoelectromechanical switch that operates on an entirely different principle than previous efforts exploiting nanotube bending [162–166]. Our devices are straightforward to implement, self-aligned and do not require complex fabrication or geometries allowing for convenient scalability. We find double-walled nanotube devices in particular act as non-volatile memory elements capable of several gate-voltage driven switching cycles.

Our nanotube bearing devices are fabricated in high yield by using electric breakdown [130] to create gaps in a freestanding multi-wall nanotube device producing an insulating OFF state. The devices are actuated with electrostatic forces and undergo linear bearing motion that telescope the inner shells in the two MWNT or DWNT segments [167] so that they bridge the gap. This restores electrical contact and produces an ON state. Adhesion forces between the nanotube ends maintain the conductive state. For double-walled nanotube devices in particular, the insulating state is controllably restored using a gate voltage, enabling several repeated ON/OFF cycles. We thereby create three-terminal non-volatile memory devices. We model the device behavior by considering the balance of electrostatic forces tending to close the device and restore the conductance and the retraction force from the inter-tube van der Waals forces. A fit of our model to data yields an estimate for the inner shell retraction force, which agree with theoretical calculations as well as the results from atomic force microscopy (AFM) measurements [168]. Our results suggest that the intra-tube electrostatic repulsion makes a significant contribution to actuating the bearing motion. Finally, we estimate the switching speed of our devices, and find sub-nanosecond switching times for the typical nanoscale device geometries employed in our experiment, with considerable scope for further optimization of switching speed by using shorter and thinner nanotubes.

Samples are fabricated by one of two methods on top of heavily doped Si wafers capped by 300 nm of SiO2. The first method is to evaporate Cr/Au contacts on arc-discharge synthesized MWNTs (dispersed in 1,2-dichloroethane) deposited on the substrate, and then using 10:1 buffered HF to etch the oxide and suspend the tubes. The second is by forming the electrical leads, etching the oxide with 10:1 buffered HF and then depositing MWNTs on top. A device schematic with the nanotubes on top of the leads is shown in the inset to Fig. 8.1.

Our ∼40 MWNT samples studied typically had an initial resistance ranging from ∼10 kΩ to a few MΩ. A sufficiently high voltage V across the higher-resistance samples usually resulted in a rapid drop in resistance [129, 147]. This phenomenon enabled us to obtain low-resistance nanotube devices with resistance ∼10–20 kΩ from nearly all contacted nanotubes. Figure 8.1 shows an IV curve taken in an Ar atmosphere from a device that was pre-annealed (device D1). The current rises approximately linearly until $V \approx 4.45$ V at which point I drops to zero and V is quickly ramped down. This observation is consistent with

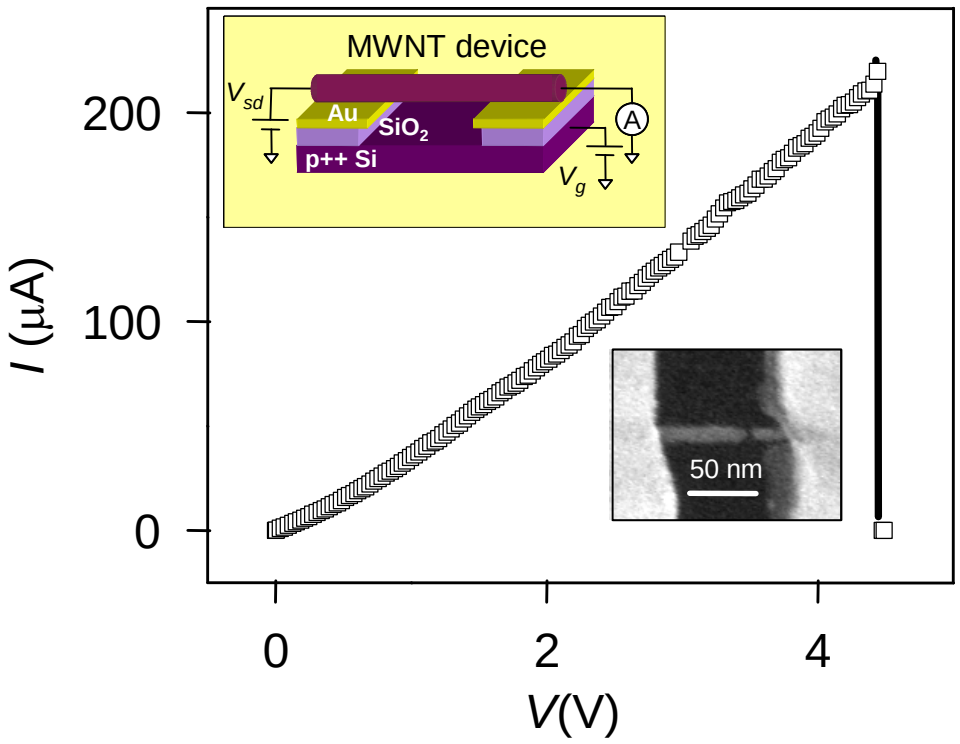

Figure 8.1. Relay device from freestanding MWNT. Main panel: IV characteristics of device D1 leading to electrical breakdown. Upper left inset: MWNT device geometry with attached electrodes and back gate. Lower-right inset: MWNT D2 with nm-size gap after electrical breakdown.

previous work in which heating and electrical stress result in the successive breakdown of the nanotube shells [130]. Indeed, SEM examination of devices after breakdown typically shows two segments with tapering ends, with each segment consisting of 10–30 shells, separated by a gap d ≈5-20 nm. Figure 8.1 shows an SEM image from a representative device D2 with such a gap. After the gaps are formed, the devices are in an insulating OFF state, consistent with expected negligible tunnel current for electrode separation exceeding ∼1–2 nm.

On application of a higher bias (typically in the range ∼5–10 V) to D1 in the OFF state, at a voltage V=4.53 V as shown in Fig. 8.2, the current increases abruptly, leading to a conductive ON state (open squares). Once the bias was reduced to 0 V, the device remains latched in this ON state, showing a finite zero-bias resistance (filled squares). In the latched ON state, subsequent SEM imaging of the devices shows that the gap vanishes, indicating nanomechanical motion of the nanotube shells to physically rejoin the two nanotube seg-

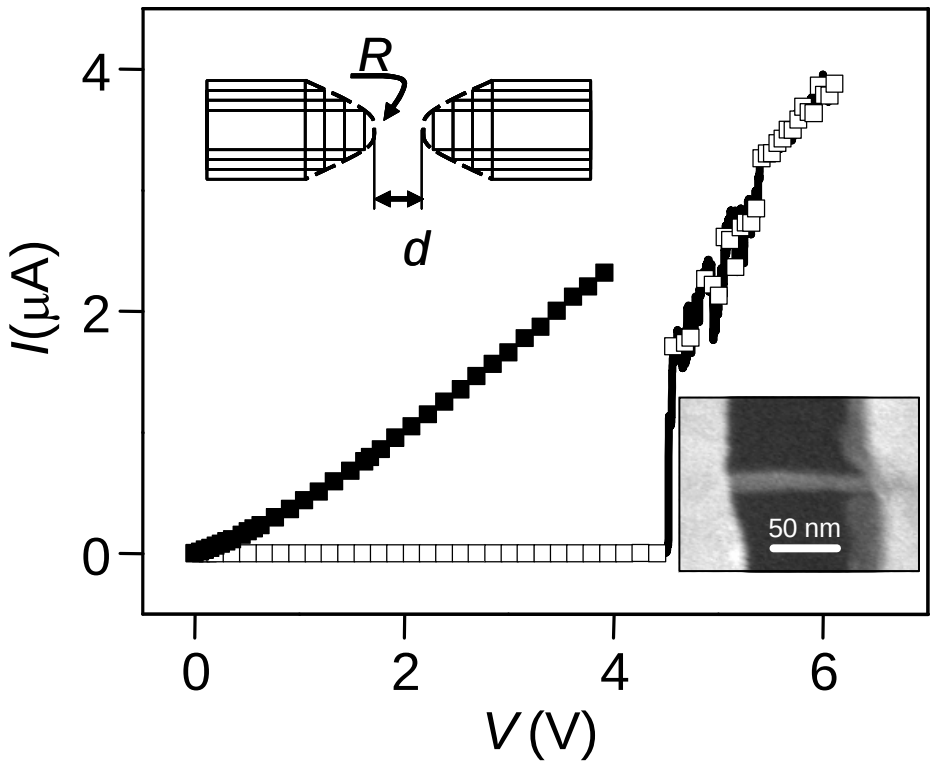

Figure 8.2. Relay device ON characteristics. Main panel: Abrupt rise in conductance of device D1 on sweeping of voltage V_{sd} (open squares) and subsequent latching in the ON state (filled squares). Lower right inset: SEM image of D2 after latching shows that gap has closed. Upper right inset: Schematic cup and cone model of the tube ends used for analysis.

ments and complete the electrical circuit. The Fig. 8.2 lower right inset shows this closure for device D2. Our devices thus act as an electrostatically actuated nanomechanical switch. Approximately 1/3 of MWNT devices switched to the ON state with $V \lesssim 10$ V.

Careful examination of the MWNT positions in a number of representative samples before and after joining showed that the outer shell remains pinned to the contact even when gaps as large as ∼20 nm have been closed. Furthermore, SEM examination of our devices rarely shows any observable slack, consistent with the high mechanical stiffness of the ∼10–20 nm diameter MWNTs. Thus, actuation is unlikely to occur in general by nanotube bending. Having ruled out these possibilities, we then consider telescoping of inner shells from their outer casing as the actuation mechanism [159]. We use the linear bearing model of Cumings and Zettl [159] to model the van der Waals force between shells

within the MWNT. The bearing is expected to act as a constant-force spring, i.e. the force is independent of the extended length, with the expected retraction force $F_R = \alpha R$, with R the extended core radius and $\alpha \sim 1$ N/m a constant. To close the circuit, F_R must be overcome by the electrostatic force due to the applied voltage. To model the electrostatic force, we approximate the MWNT segments with a cone for the tapered part, and a spherical cap at the tip (Fig. 8.2 upper left inset) [169]. The geometric parameters for this model (cap radius R, gap d, cone half-angle θ) are carefully extracted from the SEM images using a MATLAB image-processing program. We calibrated the SEM radius measurements carefully by comparing SEM images to AFM images on the same nanotube, for a selected subset of the nanotubes. The estimated radius measurement error is ± 1 nm as indicated in Figure 8.3.

The two main force contributions arise from electrostatic attraction between the segments and intra-shell electrostatic repulsion within a segment. Both of these forces tend to slide one or more shells out to close the gap. It is most straightforward to estimate these for the case where the two segments are far apart ($d \gg R$). In this case, the attractive force between segments (considered to be point charges for this evaluation) is $\pi\epsilon_0 V^2 R^2/(d+2R)^2$ while the repulsive force within a segment (modeled as force between two halves of a charged sphere) is $\pi\epsilon_0 V^2$. The force balance gives,

$$\alpha R = \pi\epsilon_0 V^2 \left[\frac{R^2}{(d+2R)^2} + 1\right]. \tag{8.1}$$

Plotting V^2 versus of R for data points with $d/R \gg 1$ should thus yield a straight line with a slope $\alpha/\pi\epsilon_0$ where $\alpha \approx 1$ N/m, obtained from previous AFM measurements [168]. Scaling data points as d/R in Fig. 8.3, indeed we find that data points with the largest d/R (corresponding to the bigger squares) lie closest to α=1 N/m.

This demonstrates that for d/R in this range the dominant actuation force comes from the intra-tube repulsive forces rather than the inter-tube attractive forces. For data with $d \approx R$ (corresponding to the smaller squares) the data falls below the line, signifying a smaller voltage to overcome the van der Waals forces for a given R. Although accurate modeling of the electrostatics for $d \approx R$ is challenging due to lack of charge distribution information on individual shells, we expect that in this regime both the electrostatic intra-

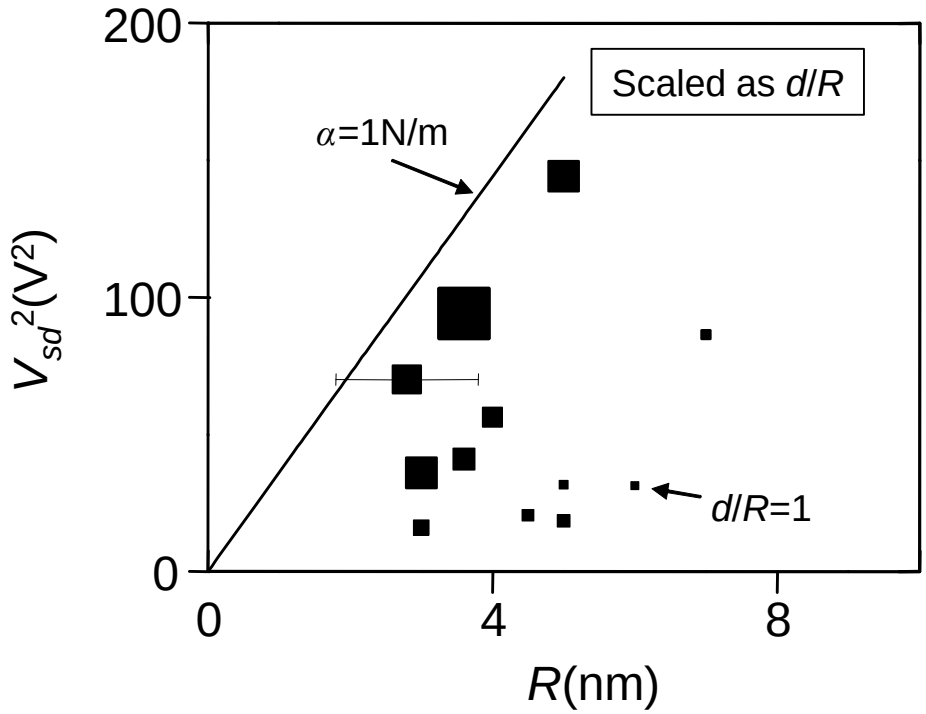

Figure 8.3. Plot of V^2 vs R. Data points' sizes are proportional to d/R. Plot shows that data matches the parameter-free model (as indicated by the force constant of 1 N/m) closely for large d/R, where it is expected to have the greatest validity. The plot also reveals that samples with nanotube segments close-in ($R \sim d$) are actuated at lower V than those well separated ($d \gg R$).

tube repulsion and inter-tube attraction are $\sim \pi\epsilon_0 V^2$, leading to a smaller closing voltage than in the $d \gg R$ regime, in qualitative agreement with our observations.

The above procedure of electrical breakdown and closing of gap with bias voltage has been applied to DWNTs as well. DWNTs were obtained commercially from NanoLab, Inc. and had a typical diameter d ≈3–6 nm. Using the p-doped Si wafer as a back gate in these samples, we find that for high enough gate voltage devices switch back to OFF state, thus enabling repeated ON-OFF cycles. Fig. 8.4 shows the time-trace plot of DWNT device D3 (with a pre-breakdown resistance of 100kΩ) for two cycles in Ar environment. In the OFF state, on applying a bias voltage the conductance increases abruptly at Vsd=9V leading to the ON state. With V_{sd}=10mV, at V_{gate}=110V the device snaps back to the zero conductance (OFF) state. On application of bias voltage, at V_{sd}=9V the device turns ON again. Nearly all of the ∼10 DWNT devices tested successfully switched back to the ON

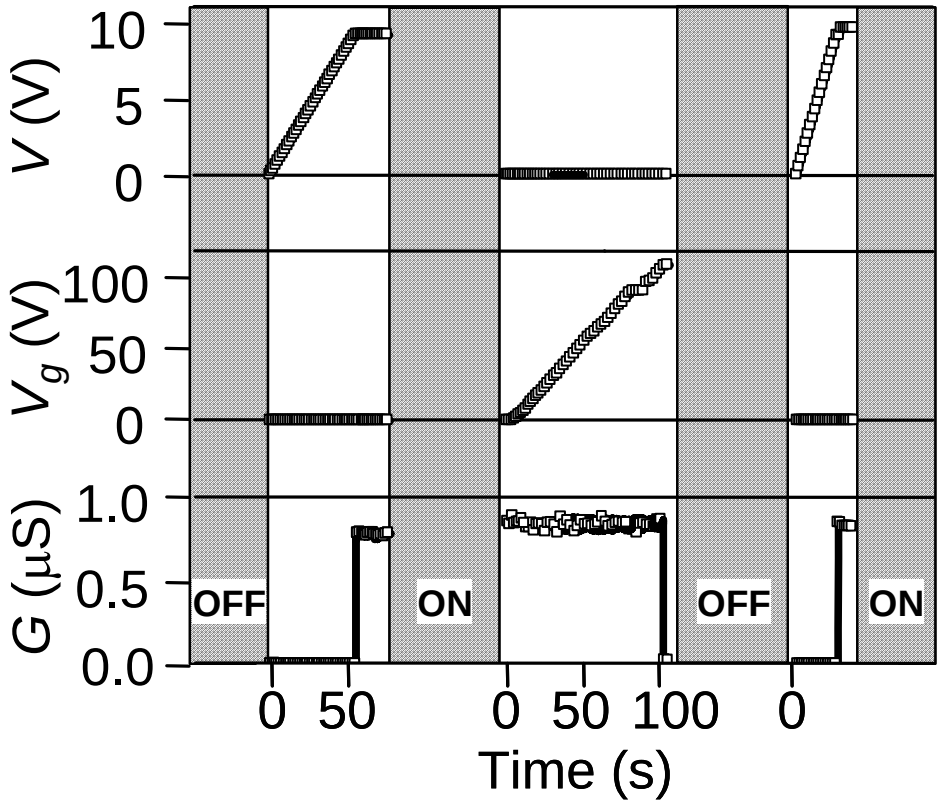

Figure 8.4. Three-terminal relay switching and operation. Plot shows the time trace of bias voltage (V), gate voltage (V_g) and conductance (G) for DWNT device D3 for two cycles. The device initially in OFF state turns ON, OFF and ON again as seen in the plot of G. Transport data was obtained from D3 in series with a 1 MΩ protection resistor.

state after electrical breakdown, and either became insulating or remained latched in the ON state within 3–4 switching cycles.

We consider the possible explanations for this reversible gate-switching. Previously, a gate voltage has been used to induce the same sign charge and create repulsive electrostatic forces between nanotubes in lateral contact [170], thereby breaking the contact between two nanotubes. However, in our devices this mechanism is unlikely because with the tapered geometry the electrostatic forces are unlikely to have any tensile component.

Another possibility is that the gate voltage places a bending stress on the nanotube that acts to break the connection. After setting the gate voltage back to zero, the nanotube segments elastically return to their original OFF state positions. The electrostatic force (per unit length) on the nanotube due to V_g is $F_{el} = \pi\epsilon V_g^2/h[log(2h/R)]^2$. Based on elementary beam mechanics, the maximum bending stress corresponding to F_{el}, (occuring

at the mid-point of the nanotube) is $\sigma = 4F_{el}L^2/(3\pi d^3)$. This is $\sim 10^{11}$ Pa for V=110V and typical values of d, L and h (d=5nm, L=500nm, h=350nm). We note that this force greatly exceeds the van der Waals forces between tube-ends, which correspond to a binding stress of $\sim 10^7$ Pa, using the value for the inter-layer adhesion in graphite. Further evidence for this mechanical switching action comes from that we do not see gate-voltage switching with MWNTs which have much larger diameters and greatly-reduced induced bending stress.

Also, the gap-closing OFF-ON transition is not as stable as seen in Fig. 8.4, if the device is imaged in the SEM in the intermediate stage or even just exposed to the ambient atmosphere, indicating that the cleanliness of the tube ends is important for stable adhesion. This and the large magnitude gate-induced bending stress suggests that the nanotube adhesion results from the formation of one or more covalent bonds between the atoms in the tube ends. However, further experiments are necessary to fully elucidate the adhesion mechanism, for example high-temperature vacuum annealing of the device post-breakdown, to close and cap the ends of the inner nanotube shells [171]. It is expected that the tube ends would then adhere with the smaller van der Waals bonds, and may permit, for example, the realization of microwave-frequency oscillators [172, 173] or charge shuttles.

We also note that the observed switching voltage can likely be reduced by optimization of the geometry such as using thinner nanotubes and decreasing the distance between the nanotube and the back gate. Using a core mass $m \approx 2\times 10^{-19}$ kg corresponding to a nanotube of length 500 nm and core radius 5 nm, an accelerating force $\sim$5 nN, and a gap distance $\sim$5 nm, we estimate using Newton's laws a switching speed $\sim$400 ps, comparable to silicon-based transistor technology. This could be reduced substantially in principle by using shorter core lengths and smaller diameter to decrease m. The time to turn the device off should be much faster, comparable to the femto- or picosecond characteristic timescale for chemical bond breaking. These intrinsic nanomechanical time scales represent a lower bound for the switching speed approachable in practice only by carefully reducing the stray device capacitances and hence the characteristic RC charging times.

In sum, we report nanoelectromechanical non-volatile memory devices that operate by using multi-walled nanotubes as a low-friction bearings. The devices are straightforward to fabricate in high yield and go through reversible ON-OFF conductance cycles with extremely high estimated switching speeds and high ON/OFF ratios. Aside from their use as nanoscale memory elements, their unique closing motion can exploited, for example, as adjustable-

gap probes to make electrical contact to other nanostructures that are attached using the flexible chemistry of the open nanotube ends.

Chapter 9

Conclusion

In this thesis, we investigated three important aspects of physics in carbon nanotubes, namely electron-electron interactions, electron-phonon interactions and phonon transport, all strongly influenced by the 1D nature of nanotubes. We also realized an application using the low-friction sliding degree-of-freedom of these low-defect structures. In addition to contributing to the physics of nanotubes, the work also highlights the use of nanotubes in studying many-body states like the Wigner crystal and Mott insulator. Future work will involve further investigating signatures of these states, perhaps using different geometries or high-frequency measurements, showing the crossover from the 1D Wigner crystal (WC) to a Luttinger liquid (LL), the interplay between the band-gap and Mott gap, or the effect of spin-orbit coupling on all of these ground states at mK temperatures and so on.

One can also use these states to realize even more theoretical predictions. One interesting state is the spin-incoherent Luttinger liquid [174]. While one could think of it as the high-temperature regime of the Wigner crystal in which the the spin degree of freedom is thermally excited, it shows qualitatively different behavior from a LL or WC and has been predicted to be responsible for one of the unsolved mysteries of mesoscopic physics, *i.e.*, the 0.7 anomaly. Carbon nanotubes could be used to shed some light on this problem. Futhermore, the Mott state as observed in nanotubes, or indeed an artificial Mott insulator using nanotubes, could be used to realize the complex many-body states predicted by the Hubbard model (though a superconducting ground-state is not a likely outcome). With thermal transport, it would be nice to observe a few quanta of thermal conductance at low temperatures. Using suspended structures such as ours, one might be able to study the interplay between quantum thermal transport and macroscopic (mechanical) modes of vibration.

In terms of technology, as was suggested in Chapter 4 one could think of the Wigner crystal as a self-assembled chain of electrons (with an inter-electron separation of $\sim$100

nm) to gate locally and use the interaction between adjacent spins to perform quantum operations. There has been some effort towards realizing a phonon laser, and our observation of electron scattering preferentially off one phonon mode makes nanotubes a promising candidate. And the linear-bearing nanoswitch is a classic example of a nano-sized system with moving parts which would not seem out of place in a (nanoscale) futuristic movie! There is indeed much physics and technology to be realized using carbon nanotubes.

Bibliography

[1] J. M. Ziman, *Electrons and Phonons* (Oxford University Press, 2001).

[2] M. P. A. Fisher, L. I. Glazman, *Mesoscopic Electron Transport* (Kluwer Academic, Boston, 1997).

[3] M. Bockrath, *et al.*, *Nature* **397**, 598 (1999).

[4] O. M. Auslaender, *et al.*, *Science* **295**, 825 (2002).

[5] A. M. Chang, *Rev. Mod. Phys.* **75**, 1449 (2003).

[6] J. Cao, Q. Wang, D. Wang, H. Dai, *Small* **1**, 138 (2005).

[7] J. Cao, Q. Wang, H. Dai, *Nat. Mater.* **4**, 745 (2005).

[8] S. Iijima, *Nature* **354**, 56 (1991).

[9] A. Thess, *et al.*, *Science* **273**, 483 (1996).

[10] J. Kong, H. T. Soh, A. M. Cassell, C. F. Quate, H. Dai, *Nature* **395**, 878 (1998).

[11] E. D. Minot, Tuning the band structure of carbon nanotubes, Ph.D. thesis, Cornell University (2004).

[12] R. Saito, G. Dresselhaus, *Physical properties of carbon nanotubes* (Imperial College Press, 1998).

[13] C. L. Kane, E. J. Mele, *Phys. Rev. Lett.* **78**, 1932 (1997).

[14] M. S. Dresselhaus, P. C. Eklund, *Advances in Physics* **49**, 705 (2000).

[15] M. Dresselhaus, G. Dresselhaus, R. Saito, A. Jorio, *Physics Reports* **409**, 47 (2005).

[16] S. Piscanec, M. Lazzeri, J. Robertson, A. C. Ferrari, F. Mauri, *Phys. Rev. B* **75**, 035427 (2007).

[17] R. Hanson, L. P. Kouwenhoven, J. R. Petta, S. Tarucha, L. M. K. Vandersypen, *Rep. Mod. Phys.* **79**, 1217 (2007).

[18] L. P. Kouwenhouven, *et al.*, *NATO ASI Series E Applied Sciences* **345**, 105 (1997).

[19] L. P. Kouwenhoven, D. G. Austing, S. Tarucha, *Rep. Prog. Phys.* **64**, 701 (2001).

[20] K. A. Matveev, *Phys. Rev. Lett* **92**, 106801 (2004).

[21] M. Bockrath, *et al.*, *Science* **275**, 1922 (1997).

[22] S. J. Tans, *et al.*, *Nature* **386**, 474 (1997).

[23] P. McEuen, M. Bockrath, D. Cobden, Y.-G. Yoon, S. Louie, *Phys. Rev. Lett.* **83**, 5098 (1999).

[24] W. Liang, M. Bockrath, H. Park, *Phys. Rev. Lett.* **88**, 126801 (2002).

[25] S. Sapmaz, *et al.*, *Phys. Rev. B* **71**, 153402 (2005).

[26] J. Nygard, D. H. Cobden, P. E. Lindelof, *Nature* **408**, 342 (2000).

[27] W. J. Liang, *et al.*, *Nature* **411**, 665 (2001).

[28] P. Jarillo-Herrero, S. Sapmaz, C. Dekker, L. P. Kouwenhoven, H. S. J. van der Zant, *Nature* **429**, 389 (2004).

[29] E. D. Minot, Y. Yaish, V. Sazonova, P. L. McEuen, *Nature* **428**, 536 (2004).

[30] P. Jarillo-Herrero, *et al.*, *Nature* **434**, 484 (2005).

[31] A. Bachtold, *et al.*, *Phys. Rev. Lett.* **87**, 166801 (2001).

[32] M. H. Devoret, *et al.*, *Phys. Rev. Lett.* **64**, 1824 (1990).

[33] Z. Yao, C. Kane, C. Dekker, *Phys. Rev. Lett.* **84**, 2941 (2000).

[34] J. Y. Park, *et al.*, *Nano Lett.* **4**, 517 (2004).

[35] A. Javey, *et al.*, *Phys. Rev. Lett.* **92**, 106804 (2004).

[36] E. Pop, *et al.*, *Phys. Rev. Lett* **95**, 155505 (2005).

[37] P. G. Collins, M. S. Arnold, P. Avouris, *Science* **292**, 706 (2001).

[38] P. Kim, L. Shi, A. Majumdar, P. L. McEuen, *Phys. Rev. Lett.* **87**, 215502 (2001).

[39] P. Kim, L. Shi, A. Majumdar, P. L. McEuen, *Physica B* **323**, 67 (2002).

[40] G. E. Begtrup, *et al.*, *Phys. Rev. Lett.* **99**, 155901 (2007).

[41] M. Bockrath, Carbon nanotubes: Electrons in one dimension, Ph.D. thesis, University of California at Berkeley (1999).

[42] D. Mann, Synthesis of single-walled carbon nanotubes and their electro-thermal and opto-electronic properties, Ph.D. thesis, Stanford University (2006).

[43] L. Huang, *et al.*, *J. Phys. Chem. B* **110**, 11103 (2006).

[44] O. M. Auslaender, *et al.*, *Science* **308**, 88 (2005).

[45] T. Giamarchi, *Quantum Physics in One Dimension* (Oxford University Press, 2004).

[46] A. O. Gogolin, A. A. Nersesyan, A. M. Tsvelik, *Bosonization and Strongly Correlated Systems* (Cambridge University Press, 2004).

[47] L. S. Levitov, A. M. Tsvelik, *Phys. Rev. Lett.* **90**, 016401 (2003).

[48] S. Coleman, *Phys. Rev. D* **11**, 2088 (1975).

[49] S. Mandelstam, *Phys. Rev. D* **11**, 3026 (1975).

[50] L. Balents, M. P. A. Fisher, *Phys. Rev. B* **55**, R11973 (1997).

[51] H.-H. Lin, *Phys. Rev. B* **58**, 4963 (1998).

[52] D. S. Novikov. Personal communication.

[53] A. A. Odintsov, H. Yoshioka, *Phys. Rev. B* **59**, R10457 (1999).

[54] E. Dagotto, T. M. Rice, *Science* **271**, 618 (1996).

[55] Y. A. Krotov, D.-H. Lee, S. G. Louie, *Phys. Rev. Lett.* **78**, 4245 (1997).

[56] A. A. Nersesyan, A. M. Tsvelik, *Phys. Rev. B* **68**, 235419 (2003).

[57] Z. Yao, H. W. C. Postma, L. Balents, C. Dekker, *Nature* **402**, 273 (1999).

[58] A. Schwartz, *et al.*, *Phys. Rev. B* **58**, 1261 (1998).

[59] E. Wigner, *Phys. Rev.* **46**, 1002 (1934).

[60] H. J. Schulz, *Phys. Rev. Lett.* **71**, 1864 (1993).

[61] G. A. Fiete, K. Le Hur, L. Balents, *Phys. Rev. B* **72**, 125416 (2005).

[62] M. M. Fogler, E. Pivovarov, *Phys. Rev. B* **72**, 195344 (2005).

[63] M. Kindermann, P. W. Brouwer, A. J. Millis, *Phys. Rev. Lett* **97**, 036809 (2006).

[64] H. Steinberg, *et al.*, *Phys. Rev. B* **73**, 113307 (2006).

[65] M. Yamamoto, M. Stopa, Y. Tokura, Y. Hirayama, S. Tarucha, *Science* **313**, 204 (2006).

[66] D. S. Novikov, *Phys. Rev. B* **72**, 235428 (2005).

[67] D. H. Cobden, M. Bockrath, P. L. McEuen, A. G. Rinzler, R. E. Smalley, *Phys. Rev. Lett.* **81**, 681 (1998).

[68] K. A. Matveev, *Phys. Rev. B* **70**, 245319 (2004).

[69] A. D. Klironomos, R. R. Ramazashvili, K. A. Matveev, *Phys. Rev. B* **72**, 195343 (2005).

[70] Y. Oreg, K. Byczuk, B. I. Halperin, *Phys. Rev. Lett.* **85**, 365 (2000).

[71] D. Goldhaber-Gordon, *et al.*, *Nature* **391**, 156 (1998).

[72] R. Zitko, J. Bonca, A. Ramsak, T. Rejec, *Phys. Rev. B* **73**, 153307 (2006).

[73] S. Sasaki, *et al.*, *Nature* **405**, 764 (2000).

[74] A. Javey, J. Guo, W. Q., L. M., H. J. Dai, *Nature* **424**, 654 (2003).

[75] I. V. Krive, A. A. Nersesyan, M. Jonson, R. I. Shekhter, *Phys. Rev. B* **52**, 10865 (1995).

[76] S. J. Tans, M. H. Devoret, R. J. A. Groeneveld, C. Dekker, *Nature* **394**, 761 (1998).

[77] N. F. Mott, *Rev. Mod. Phys.* **40**, 677 (1968).

[78] M. Imada, A. Fujimori, Y. Tokura, *Rev. Mod. Phys.* **70**, 1039 (1998).

[79] J. Wu, *et al.*, *Nano Lett.* **6**, 2313 (2006).

[80] P. A. Lee, N. Nagaosa, X.-G. Wen, *Rev. Mod. Phys.* **78**, 17 (2006).

[81] V. V. Deshpande, M. Bockrath, *Nat. Phys.* **4**, 314 (2008).

[82] F. Kuemmeth, S. Ilani, D. C. Ralph, P. L. McEuen, *Nature* **452**, 448 (2008).

[83] J.-C. Charlier, X. Blase, S. Roche, *Rev. Mod. Phys.* **79**, 677 (2007).

[84] M. Ouyang, J.-L. Huang, C. L. Cheung, C. M. Lieber, *Science* **292**, 702 (2001).

[85] C. Zhou, J. Kong, H. Dai, *Phys. Rev. Lett.* **84**, 5604 (2000).

[86] X. Huang, *et al.*, *Nano Lett.* **5**, 1515 (2005).

[87] P. Jarillo-Herrero, *et al.*, *Phys. Rev. Lett.* **94**, 156802 (2005).

[88] W. Chen, A. V. Andreev, A. M. Tsvelik, D. Orgad, *arXiv.org:0807.1936* (2008).

[89] S. De Franceschi, *et al.*, *Phys. Rev. Lett.* **86**, 878 (2001).

[90] M. Garst, D. S. Novikov, A. Stern, L. I. Glazman, *Phys. Rev. B* **77**, 035128 (2008).

[91] D. M. Newns, *et al.*, *Appl. Phys. Lett.* **73**, 780 (1998).

[92] G. G. Samsonidze, *et al.*, *Phys. Rev. B* **75**, 155420 (2007).

[93] M. Lazzeri, F. Mauri, *Phys. Rev. B* **73**, 165419 (2006).

[94] O. Dubay, G. Kresse, *Phys. Rev. B* **67**, 035401 (2003).

[95] N. Caudal, A. M. Saitta, M. Lazzeri, F. Mauri, *Phys. Rev. B* **75**, 115423 (2007).

[96] M. Lazzeri, S. Piscanec, F. Mauri, A. C. Ferrari, J. Robertson, *Phys. Rev. B* **73**, 155426 (2006).

[97] O. Dubay, G. Kresse, H. Kuzmany, *Phys. Rev. Lett.* **88**, 235506 (2002).

[98] R. B. Capaz, C. D. Spataru, P. Tangney, M. L. Cohen, S. G. Louie, *Phys. Rev. Lett.* **94**, 036801 (2005).

[99] M. S. Dresselhaus, G. Dresselhaus, A. Jorio, A. G. S. Filho, R. Saito, *Carbon* **40**, 2043 (2002).

[100] L. Kavan, *et al.*, *J. Phys. Chem. B* **105**, 10764 (2001).

[101] P. M. Rafailov, J. Maultzsch, C. Thomsen, H. Kataura, *Phys. Rev. B* **72**, 045411 (2005).

[102] S. B. Cronin, *et al.*, *Appl. Phys. Lett.* **84**, 2052 (2004).

[103] S. Reich, C. Thomsen, J. Maultzsch, *Carbon Nanotubes* (Wiley-VCH, 2004).

[104] R. Kumar, S. B. Cronin, *Phys. Rev. B* **75**, 155421 (2007).

[105] D. Mann, *et al.*, *J. Phys. Chem. B* **110**, 1502 (2006).

[106] M. Lazzeri, S. Piscanec, F. Mauri, A. C. Ferrari, J. Robertson, *Phys. Rev. Lett.* **95**, 236802 (2005).

[107] M. Z. Atashbar, S. Singamaneni, *Appl. Phys. Lett.* **86**, 123112 (2005).

[108] A. Bassil, P. Puech, L. Tubery, W. Bacsa, E. Flahaut, *Appl. Phys. Lett.* **88**, 173113 (2006).

[109] S. Chiashi, Y. Murakami, Y. Miyauchi, S. Maruyama, *Chem. Phys. Lett.* **386**, 89 (2004).

[110] L. Ci, *et al.*, *Appl. Phys. Lett.* **82**, 3098 (2003).

[111] F. Huang, *et al.*, *J. Appl. Phys.* **84**, 4022 (1998).

[112] P. V. Huong, R. Cavagnat, P. M. Ajayan, O. Stephan, *Phys. Rev. B* **51**, 10048 (1995).

[113] H. D. Li, *et al.*, *Appl. Phys. Lett.* **76**, 2053 (2000).

[114] N. R. Raravikar, *et al.*, *Phys. Rev. B* **66**, 235424 (2002).

[115] A. Jorio, *et al.*, *Phys. Rev. B* **66**, 115411 (2002).

[116] E. B. Tucker, *Phys. Rev. Lett.* **6**, 547 (1961).

[117] R. E. Nahory, *Phys. Rev.* **178**, 1293 (1969).

[118] R. W. Shaw, *Phys. Rev. B* **3**, 3283 (1971).

[119] R. Merlin, *Solid State Communications* **102**, 207 (1997).

[120] C. G. Rodrigues, urea R. Vasconcellos, R. Luzzi, *Solid State Communications* **140**, 135 (2006).

[121] I. Camps, S. S. Makler, H. M. Pastawski, L. E. F. F. Torres, *Phys. Rev. B* **64**, 125311 (2001).

[122] J. C. Meyer, *et al.*, *Phys. Rev. Lett.* **95**, 217401 (2005).

[123] Y. Zhang, J. Zhang, H. Son, J. Kong, Z. Liu, *J. Am. Chem. Soc.* **127**, 17156 (2005).

[124] S. D. M. Brown, *et al.*, *Phys. Rev. B* **63**, 155414 (2001).

[125] F. Cataldo, *Fullerenes, Nanotubes and Carbon Nanostructures* **10**, 293 (2002).

[126] C. L. Kane, *et al.*, *Europhys. Lett.* **41**, 683 (1998).

[127] R. Saito, *et al.*, *Phys. Rev. B* **64**, 085312 (2001).

[128] Y. Wu, *et al.*, *Phys. Rev. Lett.* **99**, 027402 (2007).

[129] H. Y. Chiu, *et al.*, *Phys. Rev. Lett* **95**, 226101 (2005).

[130] P. G. Collins, M. Hersam, M. Arnold, R. Martel, P. Avouris, *Phys. Rev. Lett.* **86**, 3128 (2001).

[131] A. Bushmaker, V. Deshpande, M. Bockrath, S. Cronin, *Nano Lett.* **7**, 3618 (2007).

[132] M. Oron-Carl, R. Krupke, *Phys. Rev. Lett.* **100**, 127401 (2008).

[133] T. Yamamoto, S. Watanabe, K. Watanabe, *Phys. Rev. Lett.* **92**, 075502 (2004).

[134] N. Mingo, D. A. Broido, *Phys. Rev. Lett* **95**, 096105 (2005).

[135] C. H. Yu, L. Shi, Z. Yao, D. Y. Li, A. Majumdar, *Nano Lett.* **5**, 1842 (2005).

[136] I.-K. Hsu, *et al.*, *Appl. Phys. Lett.* **92**, 063119 (2008).

[137] J. B. Pendry, *J. Phys. A* **16**, 2161 (1983).

[138] R. Maynard, E. Akkermans, *Phys. Rev. B* **32**, 5440 (1985).

[139] K. Schwab, E. A. Henriksen, J. M. Worlock, M. L. Roukes, *Nature* **404**, 974 (2000).

[140] J. Hone, M. Whitney, C. Piskoti, A. Zettl, *Phys. Rev. B* **59**, R2514 (1999).

[141] J. Hone, B. Batlogg, Z. Benes, A. T. Johnson, J. E. Fischer, *Science* **289**, 1730 (2000).

[142] M. C. Llaguno, J. E. Fischer, A. T. Johnson, J. Hone, *Nano Lett.* **4**, 45 (2004).

[143] M. R. Buitelaar, T. Nussbaumer, C. Schonenberger, *Phys. Rev. Lett.* **89**, 256801 (2002).

[144] E. Brown, L. Hao, J. C. Gallop, J. C. Macfarlane, *Appl. Phys. Lett.* **87**, 023107 (2005).

[145] B. Bourlon, *et al.*, *Phys. Rev. Lett.* **92**, 026804 (2004).

[146] J. Nygard, D. H. Cobden, *Appl. Phys. Lett.* **79**, 4216 (2001).

[147] J. Y. Huang, *et al.*, *Phys. Rev. Lett.* **94**, 236802 (2005).

[148] J. Cumings, P. G. Collins, A. Zettl, *Nature* **406**, 586 (2000).

[149] S. Frank, P. Poncharal, Z. L. Wang, W. A. De Heer, *Science* **280**, 1744 (1998).

[150] A. Bezryadin, C. Dekker, *J. Vac. Sci. Technol. B* **15**, 793 (1997).

[151] L. G. C. Rego, G. Kirczenow, *Phys. Rev. Lett.* **81**, 232 (1998).

[152] L. X. Benedict, S. G. Louie, M. L. Cohen, *Solid State Commun.* **100**, 177 (1996).

[153] M. S. Dresselhaus, G. Dresselhaus, P. C. Eklund, *Science of Fullerenes and Carbon Nanotubes: Their Properties and Applications* (Academic Press, 1996).

[154] E. Kaxiras, K. C. Pandey, *Phys. Rev. Lett.* **61**, 2693 (1988).

[155] L. C. Venema, *et al.*, *Appl. Phys. Lett.* **71**, 2629 (1997).

[156] P.-M. Allemand, *et al.*, *Science* **253**, 301 (1991).

[157] M. Roukes, *Phys. World* **14 (2)**, 25 (2001).

[158] T. Rueckes, *et al.*, *Science* **289**, 94 (2000).

[159] J. Cumings, A. Zettl, *Science* **289**, 602 (2000).

[160] A. M. Fennimore, *et al.*, *Nature* **424**, 408 (2003).

[161] B. Bourlon, D. C. Glattli, C. Miko, L. Forro, A. Bachtold, *Nano Lett.* **4**, 709 (2004).

[162] J. M. Kinaret, T. Nord, S. Viefers, *Appl. Phys. Lett.* **82**, 1287 (2003).

[163] S. N. Cha, *et al.*, *Appl. Phys. Lett.* **86**, 083105 (2005).

[164] J. E. Jang, *et al.*, *Appl. Phys. Lett.* **87**, 163114 (2005).

[165] E. Dujardin, V. Derycke, M. F. Goffman, R. Lefevre, J. P. Bourgoin, *Appl. Phys. Lett.* **87**, 193107 (2005).

[166] S. W. Lee, *et al.*, *Nano Lett.* **4**, 2027 (2004).

[167] L. Forro, *Science* **289**, 560 (2000).

[168] A. Seiji, Y. Nakayama, *Jpn. J. Appl. Phys.* **42**, 4830 (2003).

[169] S. Hudlet, M. Saint Jean, C. Guthmann, J. Berger, *Eur. Phys. J. B* **2**, 5 (1998).

[170] P. Kim, C. M. Lieber, *Science* **286**, 2148 (1999).

[171] H. Z. Geng, *et al.*, *Chem. Phys. Lett.* **399**, 109 (2004).

[172] Q. S. Zheng, Q. Jiang, *Phys. Rev. Lett.* **88**, 045503 (2002).

[173] S. B. Legoas, *et al.*, *Phys. Rev. Lett.* **90**, 055504 (2003).

[174] G. A. Fiete, *Rep. Mod. Phys.* **79**, 801 (2007).